

ANTIFERROMAGNETISM IN THE SUPER-DEGENERATE KAGOMÉ LATTICE AND CUPRATES

AMIT KEREN

Abstract

This thesis concentrates on two different areas of magnetism that have been of high profile in the past few years: the kagomé lattice, which belongs to a branch of magnetism known as frustrated magnets, and the cuprates, which are a derivative of the research of superconductivity. Though several investigative techniques are utilized in this work, the chief experimental method is the muon spin rotation/relaxation (μ SR). I therefore devote chapters 1 and 2 to μ SR, using the first to review the experimental setup and traditional means of interpreting the data, and the second to present my personal contribution to the understanding of muon spin relaxation, based on three of my publications [1, 2, 3]. Equipped with the knowledge of the μ SR technique, I move on to present the experiments. In chapter 3 I discuss the physics of localized moments on the highly degenerate kagomé lattice, a fascinating subject from both a theoretical and experimental point of view. As we shall see, this subject involves new physical concepts, and systems with kagomé lattice structure show very unusual behavior in a variety of measurements. Here I present data on $\text{SrCr}_{8-x}\text{Ga}_{4+x}\text{O}_{19}$ and $\text{KR}_3(\text{OH})_6(\text{SO}_4)_2$ ($\text{R}=\text{Cr}$ or Fe) and attempt to account for some of the observed behavior with new models. However, a complete picture of this system requires further research. This chapter too is based on three published papers [4, 5, 6] as well as a fourth one which is currently in preparation; my work on the kagomé lattice was also orally presented in the international μ SR conference in Maui. Next I go on to present the subject of antiferromagnetism in the two cuprates systems known as the “infinite layers” ($\text{Ca}_{0.86}\text{Sr}_{0.14}\text{CuO}_2$) and “infinite chains” (R_2CuO_3 $\text{R}=\text{Ca}$ or Sr). The initial motivation for the investigation of these systems was the simplicity of their crystal structure and their resemblance to the building blocks of high T_c superconductors. However, throughout the research it became evident that the infinite chains are interesting on their own merit. I therefore discuss these subjects in two different chapters, 4 and 5, and concentrate mainly on the influence of dimensionality on their magnetic properties. Again, these chapters are based on two published papers [7, 8] and the work on the “infinite chain” was also orally presented in the international conference on magnetism in Warsaw (ICM’94). As in the case of the kagomé lattice, the research on the infinite chains is still in progress in my group, and both topics remain exciting and active areas of research throughout the solid state community.

SUBMITTED IN PARTIAL FULFILLMENT OF THE
REQUIREMENTS FOR THE DEGREE
OF DOCTOR OF PHILOSOPHY
IN THE GRADUATE SCHOOL OF ARTS AND SCIENCES

COLUMBIA UNIVERSITY

1994

© 1994

Amit Keren
All Rights Reserved

Contents

| | | |
|----------|---|-----------|
| 1 | The μSR Technique | 1 |
| 1.1 | Experimental Setup | 1 |
| 1.1.1 | Production of Polarized Muons | 2 |
| 1.1.2 | The Longitudinal Field Configuration | 2 |
| 1.1.3 | The Transverse Field Configuration | 3 |
| 1.1.4 | Electronics | 3 |
| 1.1.5 | The Sample | 4 |
| 1.1.6 | Cryogenics | 4 |
| 1.1.7 | Data Analysis | 5 |
| 1.2 | Muon Spin Rotation | 5 |
| 1.3 | Traditional Theory of Muon Spin Relaxation | 6 |
| 2 | A New Look at Muon Spin Relaxation | 7 |
| 2.1 | The Paramagnetic State ($T \gg T_N$) | 8 |
| 2.2 | Critical Region ($T \rightarrow T_N$) | 10 |
| 2.3 | Relaxation Mechanism ($T \rightarrow 0$) | 12 |
| 2.4 | Hopping | 14 |
| 2.5 | Summary | 15 |
| 3 | The Kagomé Lattice | 16 |
| 3.1 | Introduction | 16 |
| 3.2 | $\text{SrCr}_{8-x}\text{Ga}_{4+x}\text{O}_{19}$ | 20 |
| 3.2.1 | Susceptibility Measurements | 21 |
| 3.2.2 | μ SR Measurements | 21 |
| 3.2.3 | Discussion | 25 |
| 3.3 | The Jarosite Systems | 25 |
| 3.3.1 | $\text{KFe}_3(\text{OH})_6(\text{SO}_4)_2$ | 25 |
| 3.3.2 | $\text{KCr}_3(\text{OH})_6(\text{SO}_4)_2$ | 26 |
| 3.3.3 | Discussion | 27 |
| 3.4 | Numerical Simulation | 27 |
| 3.5 | Conclusion and Discussion | 31 |
| 3.5.1 | Summary of Experimental results | 31 |
| 3.5.2 | Speculations on Dynamics in the Kagomé lattice | 32 |
| 4 | The “Infinite Layer” Cuprate Antiferromagnets | 34 |
| 4.1 | Introduction | 34 |
| 4.2 | μ SR Measurements | 35 |
| 4.3 | Muon Diffusion | 36 |
| 4.4 | Muon Sites | 37 |
| 4.5 | Discussion | 38 |
| 5 | The “Infinite-Chain” Cuprate Antiferromagnets | 39 |
| 5.1 | Introduction | 39 |
| 5.2 | The Ca_2CuO_3 system | 39 |
| 5.2.1 | μ SR measurements | 39 |
| 5.2.2 | Susceptibility Measurements | 40 |
| 5.2.3 | Magnon Raman Scattering | 41 |
| 5.3 | The Sr_2CuO_3 system | 41 |
| 5.3.1 | μ SR Measurements | 41 |

| | | |
|-------|---------------------------------------|----|
| 5.3.2 | Susceptibility Measurements | 42 |
| 5.4 | Discussion | 43 |

| | | |
|----------|---|-----------|
| A | The McMullen and Zaremba Formula | 43 |
|----------|---|-----------|

| | | |
|----------|------------------------------|-----------|
| B | The Fermi Golden Rule | 45 |
|----------|------------------------------|-----------|

| | | |
|----------|-------------------------|-----------|
| C | Spin-Wave Theory | 45 |
|----------|-------------------------|-----------|

| | | |
|----------|-------------------|-----------|
| D | Spin Glass | 46 |
|----------|-------------------|-----------|

Contents

1 The μ SR Technique

The positive muon spin rotation/relaxation technique, denoted here as μ SR, is based on the direct measurement of the time evolution of a positive muon (μ^+) spin polarization $\mathbf{P}(t)$ in a sample. This evolution depends on the magnetic field experienced by the μ^+ and thus provides information on the magnetic environment in the vicinity of the muon. This technique allows us to detect static magnetic fields as small as a fraction of a Gauss and as large as several Tesla. We can also detect fluctuating fields on a time scale between 10^{-3} and 10^{-6} sec. The biggest advantage of this technique is that there is no need for a fine tuning of the experimental apparatus (as in techniques which depend on resonance or scattering). The weakness of μ SR is in the lack of direct determination of the muon site in the sample which limits the amount of information we can obtain on the magnetic environment. This chapter deals with both the experimental method and the information we can obtain about the magnetic environment using the μ SR.

1.1 Experimental Setup

The measurement of the muon spin polarization is made possible due to three properties of the muon particle:

- (I) Muons produced from pion decay are polarized.
- (II) The muon decay into a positron and two neutrinos, according to

$$\mu^+ \longrightarrow e^+ + \nu_e + \bar{\nu}_\mu$$

with the positrons emerging, for the most part, with high enough energy to travel a substantial distance before annihilating.

(III) The distribution of decayed positrons is not spherically symmetric, but rather depends on the muon polarization. The angular distribution of the muon decay probability with respect to the initial muon polarization is displayed in Fig. 1. In this figure the radial distance represents the relative probability that a positron is emitted in a given direction at some energy. By measuring the change in the angular distribution of

positrons as a function of time, the muon polarization can be reconstructed.

The ways in which we produce the muons, handle the sample and external field, detect the positron, and reconstruct the polarization are described below. Naturally, we emphasize the aspects of μ SR relevant to the experiments presented in subsequent chapters.

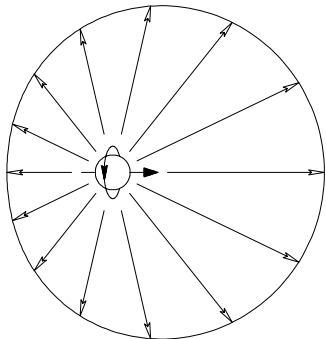
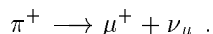


Figure 1: Angular distribution of positrons from muon decay, integrated over energy.

1.1.1 Production of Polarized Muons

Our experiments were conducted at the TRIUMF μ SR facility (Vancouver B.C.). At the heart of this facility is a cyclotron, where protons are accelerated to 500 MeV and then made hit a production target (usually Graphite or Beryllium). At the target, pions are produced through the reactions of the projectile proton with the target's nuclei. Positive muons are produced from the pions (with pion lifetime $\tau_\pi = 26$ nsec) according to



Since only left handed neutrinos exist, and because pions have zero spin, the muons are created with their spin polarized (\vec{s}_μ antiparallel to \vec{p}_μ , as shown in the inset of Fig. 2). However, the pion decay is isotropic, and, in principle, if the pions decay in flight, the beam can contain fast muons with down spin (emitted in the direction of pion velocity), or slow muons with up spin (emitted in the direction opposite to the pion velocity). If, on the other hand, the pions decay at rest, the muons produced in the direction of the beam pipe are fully polarized. Therefore, we select only those muons produced by pions which decay at rest near the target surface ($\vec{p}_\pi = 0$). These muons are known as “surface muons”.

Figure 2 shows a schematic diagram of a muon beamline. After the production of surface muons, dipole magnets serve to guide the beam and select the muon momentum. There are also tens of quadrupole magnets on the line employed to focus the beam. A set of slits controls the rate at which

muons arrive into the experimental area. We usually ensure that no more than 30000 muons per second arrive at the apparatus, thus keeping the average time between two muons $33 \mu\text{sec}$ ($15 \times \tau_c$). Near the experimental area, a DC separator (crossed electric and magnetic fields with $E/B = v_\mu$) serves to reject positrons which contaminate the beam. By applying a large magnetic field B , and scaling the electric field E appropriately, we can also rotate the muon spin while selecting the same muon velocity.

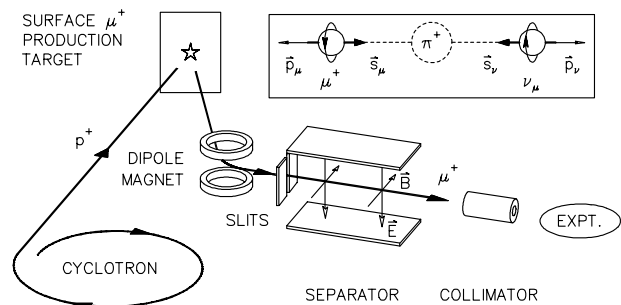


Figure 2: Production of polarized surface muon.

At the end of the beam pipe we place the refrigerator (cryostat) and surround it with positron counters and coils (see Fig. 3). The refrigerator (cryostat) is fitted with thin windows to allow the beam to access the sample. The positron counters and magnetic field are arranged in one of two possible configurations: longitudinal or transverse, depending on the information we are trying to obtain from our measurements.

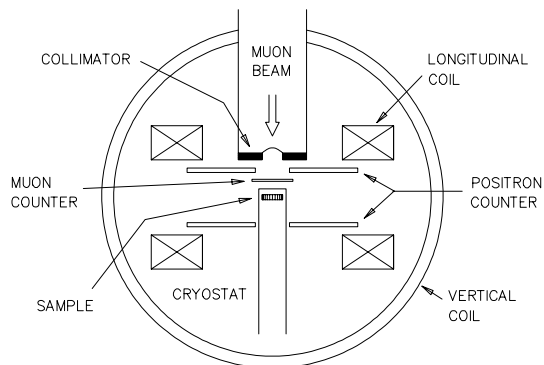


Figure 3: Top view of schematic layout of a μ SR apparatus.

1.1.2 The Longitudinal Field Configuration

The Longitudinal Field (LF) [including the Zero Field (ZF)] experimental configuration is used to measure the rate in which the muon loses its polarization in the

sample as a function of a magnetic field applied along the initial muon spin direction (H_L). This setup is based on the fact that at $t = 0$ positrons are preferentially emitted in the forward direction, while at $t \rightarrow \infty$, when the muons have lost their polarization, there is no difference between the forward and backward directions. We therefore place two positron counters as shown in Fig. 4a. The backward (B) counter has a small hole in it which allows the incoming muons to reach the sample (S). The forward (F) counter has a larger hole in it which allows access to the cryogenics. Between the B counter and the sample we place a muon counter (M) with a very thin (0.025 cm) scintillator (in order not to stop the beam). This counter starts the clock every time a muon enters the sample.

1.1.3 The Transverse Field Configuration

The transverse field (TF) experimental configuration is used to measure both the frequency of muon precession and the rate in which it loses phase coherence when the field is applied perpendicularly to the initial muon spin direction (H_T). There are two ways to create this configuration. I) The counters are set up in the same way as in the LF configuration, but the field is applied in a direction perpendicular to the beam. This configuration is shown in Fig. 4b. II) The muon spin is rotated by the separators and the field is applied parallel to the beam. In the latter configuration, the counters are placed above (U) and below (D) (or on the left and right sides) of the specimen as shown in Fig. 4c.

The signals from the counters are transferred to a counting room where we place our electronic gates.

1.1.4 Electronics

In our measurements we are interested in the time evolution of the muon polarization, rather than its equilibrium value. We therefore require our electronic system to record the time in which a positron was detected. In addition, we have to ensure that the positrons we detect come from a muon that entered the sample at $t = 0$. This is the most common case, although sometimes a different order of event can take place: a bunch of muons can arrive together giving rise to several positron counts at different times; a muon can decay in the area between the separator and the experimental apparatus producing a stray positron that can be mistakenly identified with a muon which arrived earlier. We can discriminate against these kind of events by opening a data gate ($D_g = \text{“truth”}$) for a time t_g ($t_g \gg \tau_\mu$) with the arrival of a muon, and then requiring that:

1. There is no other muon before a positron.
2. There are no two (or more) positrons within t_g .

In practice we replace condition 1 with the more restrictive demand:

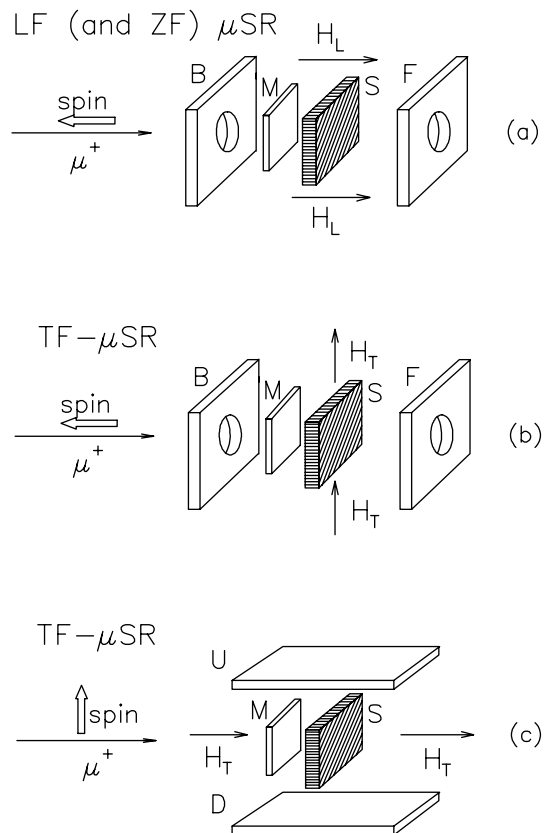
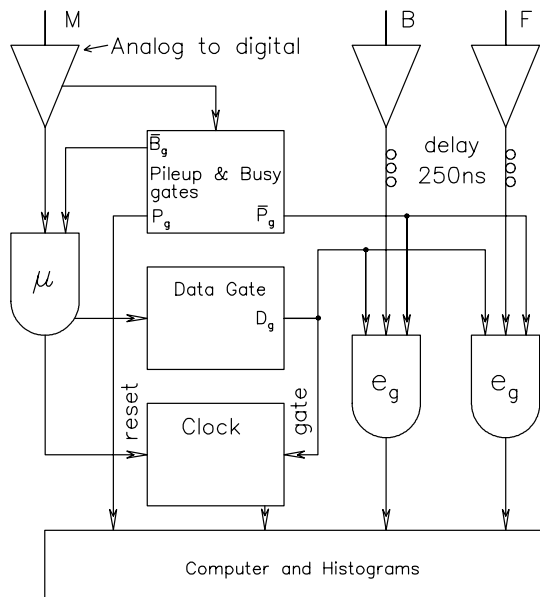


Figure 4: (a) Longitudinal (and Zero) field geometry, (b) and (c) are Transverse field geometries.

1. There are no two muons within t_g .

These conditions are achieved by the following steps:

1. When a muon enters the sample, a Pile-up gate (P_g) is set to “false”, a Busy gate (B_g) is set to “truth”, and a Data gate (D_g) is set to “truth”, all for the next t_g μ sec.
2. If a second muon enters the sample within these t_g μ sec, P_g is flipped and stays that way for the rest of the time t_g .
3. If $B_g = \text{“false”}$, (only before a fresh muon enters the sample), the clock is reset and the number of positrons detected (n) in the computer is set to zero.
4. A positron event ($e = \text{“truth”}$) is accepted, namely, its time recorded and $n = n + 1$, only if $e_g = \bar{P}_g D_g e = \text{“truth”}$.
5. The event is registered in a histogram provided that only one positron is detected ($n = 1$) and $P = \text{“false”}$ when the clock is reset.

Figure 5: *Electronic chart*

A diagram of the electronics is shown in Fig. 5.

In the histograms the information is kept in the form of the number of counts per bin, where the time each bin represents depends on the desired time resolution. The limitation on the time resolution comes from the electronics dead time of 0.25 nsec, and by the allowed computer memory per histogram (see also discussion in section 2.1).

The rejection procedure described above leaves out the possibility that a muon enters the sample, does not decay within t_g , and a stray positron (from a different source) is detected. This kind of event is considered a background event. We evaluate the rate of background events by imposing a delay time (t_d) on the positron pulse (usually $t_d = 250$ nsec). Therefore, the time it takes for a positron pulse to reach the electronics is longer than the time it takes for the muon pulse. Thus, a stray e^+ arriving at most t_d before a μ^+ , with no other e^+ detected after the μ^+ (within t_g) will be registered in the histograms at $t < 0$. These positrons allow us to estimate the rate of background events. It is easy to know where $t = 0$ is in the histogram, since the number of positrons registered at $t > 0$ is dramatically larger than at $t < 0$.

1.1.5 The Sample

The required sample size for a μ SR experiment is determined by the stopping range of the muon in the measured compound. Typical surface-muon stopping range in matter is ~ 170 mg/cm², so 0.2 mm thick samples are usually large enough. For comparison, this size is smaller than that needed for neutron scattering mea-

surements, which require samples the size of a human finger, but larger than that needed for optical measurements, which can be made on thin films. However, the μ SR technique is not inherently limited by sample size: a muon could give a signal off an object as minuscule as a single magnetic molecule. The problem lies in our ability to attach the muon to such a small object. This can only be achieved by slowing down the muons (while keeping their polarization) before they enter the sample. Currently no such slow muon beams are available, and an effort to produce them is taking place in all major μ SR facilities in the world.

The desired cross section of the sample is determined by our ability to focus the beam. Usually a cross section of 1 cm² is large enough to have more than 90% of the muons stop in the sample rather than in the sample holder or the walls of the refrigerator. Even so, some of the muons do not stop in the sample. Therefore, we place the sample on a backing material in which the muon behavior is in contrast to its expected behavior in the sample. For all the relaxation experiments presented here we used aluminum backing since muons do not depolarize in this compound, and for all the precession experiments we used rust since the muons depolarize very quickly in this compound and therefore have no precession signal.

1.1.6 Cryogenics

For measurements within the temperature range of 2 K to 300 K, the samples are mounted in a gas flow cryostat. In this cryostat liquid helium (at 4.2 K) is made to expand through small holes (diffuser) between an area where it is in liquid phase at high pressure to an area where it is in a gas phase at low pressure. The expansion of the liquid into gas provides the cooling power. The cooled gas blows on the sample thus providing a very uniform temperature.

The fine temperature control is made with two heaters: one wrapped around the diffuser and one around the sample holder. We try to generate as little heat as possible with the sample heater (by balancing the temperature first with the diffuser heater) in order to obtain better temperature homogeneity on the sample.

The experiments below 2 K are done using a ³He/⁴He Dilution Refrigerator (DR). In this refrigerator ³He is evaporated from a mixture of ³He and ⁴He. Since the concentration of ³He in the mixture is non-zero even at $T = 0^+$ the DR can, in principle, provide cooling power even at zero temperature. The practical limitation on the temperature comes from heat leaks and vibrations of the refrigerator. The lowest temperature we achieved with our DR is slightly above 20 mK. The fine temperature tuning in the dilution refrigerator is also done with a heater. The cooling power is transferred to the sample by mechanical contact. This fact could hinder us from achieving uniform temperature

when we use samples with low heat conductivity or powder samples. In the case of powder samples, the heat conductivity can be improved by mixing the sample with a non-magnetic sticky grease (see chapter 3.3).

The temperature in both cases is measured with calibrated carbon resistors, and its stability is maintained with an automatic temperature controller which increases or decreases the amount of power going into the heater according to the deviation of the real sample temperature from the desired one. Usually the temperature stability is better than 1%.

1.1.7 Data Analysis

From our electronic system we obtain, for each detector, a histogram of detected positrons as a function of the time difference between the muon arrival at the sample and its decay. The number of detected positrons in a histogram corresponding, for example, to the back (B) counter is given by:

$$N_B(t) = N_0^B [B_B + \exp(-t/\tau_\mu) (1 + A_0 P(t))] \quad (1)$$

where B_B is the time-independent background, $P(t)$ is the muon polarization function and A_0 is the asymmetry.

The constant backgrounds ($N_0^B B_B$, and $N_0^F B_F$), which are measured during times where no muons are in the sample (see 1.1.4), are first subtracted to form:

$$B(t) = N_B(t) - N_0^B B_B \quad (2)$$

$$F(t) = N_F(t) - N_0^F B_F. \quad (3)$$

The experimental (raw) asymmetry $A_r(t)$ is then defined as:

$$A_r(t) = \frac{B(t) - F(t)}{B(t) + F(t)} \quad (4)$$

$$= \frac{(1 - \alpha) + (1 + \alpha)A_0^B P(t)}{(1 + \alpha) + (1 - \alpha)A_0^B P(t)} \quad (5)$$

where α is the ratio of the raw count rates N_0^F/N_0^B . Equation (5) can be inverted to give the corrected asymmetry:

$$A(t) = A_0^B P(t) = \frac{(\alpha - 1) + (\alpha + 1)A_r(t)}{(\alpha + 1) + (\alpha - 1)A_r(t)} \quad (6)$$

which equals $A_r(t)$ when $\alpha = 1$. In Fig. 6(a) we show a raw spectrum from one counter and in Fig. 6(b) we present the corrected asymmetry corresponding to the raw asymmetry of that counter (and its corresponding counter 180° opposed to it).

The quantity α in Eq. 5 reflects the ratio of effective solid angles of the different counters and is independent of the magnetic interaction of the muon with the target. Although it could, in principle, be calculated from the experimental geometry, in practice, α is extracted

from the data empirically. In the TF configuration α is chosen such that the oscillations are centered around zero as in Fig. 6b. In the LF configuration, α is selected such that $\lim_{t \rightarrow \infty} P(t) = 0$ in the most strongly relaxing spectrum for a given sample. Since α is extremely sensitive and can be affected by the applied field, by slight changes in the sample position, and by the position of the proton beam on the production target, we leave α as a free parameter with less than 10% freedom, when fitting the asymmetry.

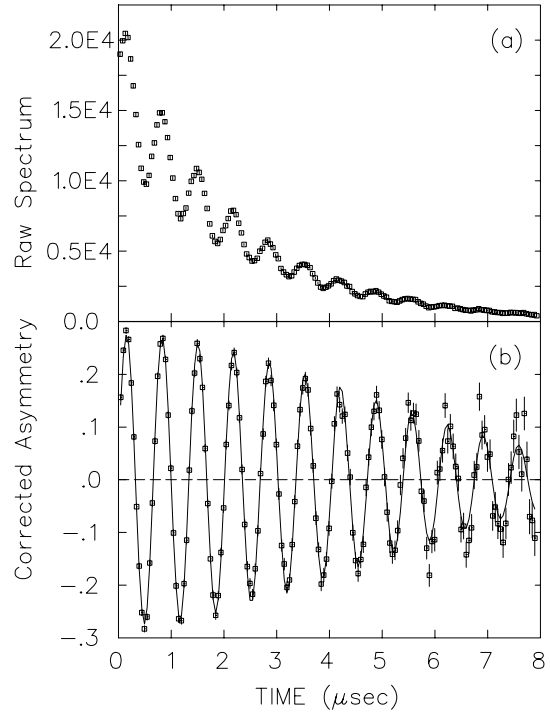


Figure 6: (a) *Raw spectrum*. (b) *Corrected asymmetry*.

We now turn to discuss the time dependence of muon spin polarization.

1.2 Muon Spin Rotation

The fully polarized muon, after entering the sample, comes to rest in a magnetic environment. Since the mechanism which stops the muon is much stronger than any magnetic interaction, the muon maintains its polarization while losing its kinetic energy. However, at the site, the muon spin starts to evolve in the local field \mathbf{B} . When all the muons experience a unique magnetic field in their site, the polarization along the \hat{z} direction [$G_z(t)$] is given by

$$G_z(t) = \text{Re} \left(\cos^2 \theta + \sin^2 \theta e^{i\omega(t-t_0)} \right) \quad (7)$$

where θ is the angle between the initial muon spin and the local field direction (see Fig. 7), $\omega = \gamma_m B$, and t_0

is the muon arrival time.[9] We chose to present this equation in a complex form for reasons which will become clear in section 2.4. When taking the powder average of Eq. 7 we get

$$G_z(t) = \frac{1}{3} + \frac{2}{3} \cos(\omega t) \quad (8)$$

where we define $t_0 = 0$.

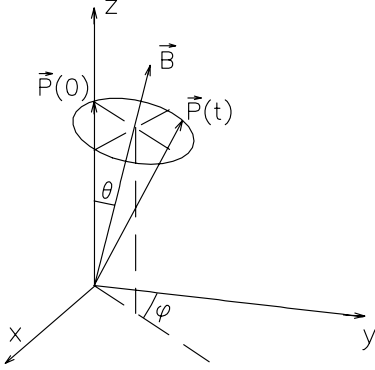


Figure 7: The \hat{z} component of the muon polarization in the presence of a constant field

In real systems, however, the local field experienced by different muons is rarely unique. It can vary from site to site as a result of nuclear moments, impurities, or non-homogeneous freezing of the ionic moments. It could also vary in time, at a given site, due to dynamical fluctuations. These two effects cause the relaxation of the oscillating amplitude (2/3) or the average polarization (1/3).

The relaxation of the 2/3 component results from both dynamical fluctuations and spatial inhomogeneities. If we ignore momentarily the dynamical fluctuations, and assume that the frequency of oscillations, instead of being unique, is distributed around a mean ω_0 with a distribution $\rho(\omega - \omega_0)$, then

$$G_z(t) = \frac{1}{3} + \frac{2}{3} \int d\omega \rho(\omega - \omega_0) \cos(\omega t). \quad (9)$$

It is easy to see that if ρ is a Gaussian/Lorentzian the 2/3 component relaxes with a Gaussian/exponential line shape. Dynamical fluctuation could only add additional sources of relaxation. However, without the help of echo techniques (as in NMR) it is hard to distinguish between the two sources of relaxation of the 2/3 component.

On the other hand the spatial inhomogeneity of the field can not cause relaxation of the 1/3 component since in the powder there are always muons (1/3 of the ensemble) with their polarization pointing along the local field. The polarization of these muons is constant unless the field changes with time. Therefore, the relaxation of the 1/3 component could result only from

dynamical fluctuations. We can isolate this effect when we have a single crystal, by orienting the crystal in such a way that $\theta = 0$ as described in 2.3. We discuss the dynamical relaxation of the muon spin in detail in the next section and in chapter 2.

For the time being we assume for data analysis the phenomenological form

$$G_z(t) = \frac{1}{3} \exp(-t/T_1) + \frac{2}{3} \exp(-[t/T_G]^2 - [t/T_1]) \cos(2\pi f t). \quad (10)$$

where

$$f = \omega/2\pi. \quad (11)$$

The combination of a linear and a quadratic terms in t in the relaxation of the 2/3 component (also known as T_2 relaxation) is supposed to account for both the static and dynamic relaxation sources. It should be pointed out that the particular choice of the relaxation function in data analysis will affect the values of T_1 and T_G but will only slightly affect the values of ω which is our primary parameter of interest.

1.3 Traditional Theory of Muon Spin Relaxation

The 100% polarization of the muons in the sample is not the equilibrium ratio of up spin to down spin and the muon gradually depolarizes in order to reach the equilibrium ratio. The time dependence of this depolarization is derived in this section using the strong collision model. In this model we assumed that the field experienced by the muon changes discontinuously (hops) at times $t_1 < \dots < t_n < t$ ($t = t_{n+1}$) with some average frequency ν . Between hops, the polarization evolves as if the field were static.[10] We demonstrate the application of this model to a field distribution given by

$$\rho(\mathbf{B}) = \frac{\gamma_m^3}{\sqrt{2\pi}\Delta^2} \exp\left(-\frac{\gamma_\mu^2 [\mathbf{B} - \mathbf{B}^s]^2}{2\Delta^2}\right) \quad (12)$$

where \mathbf{B}^s is some average field which is either applied externally or caused by magnetic order, and Δ/γ_m is the root mean square (RMS) of the field distribution.

The static relaxation function $g_0(t)$ is obtained by convoluting $G_z(t)$ from Eq. 7 with the field distribution $\rho(\mathbf{B})$. For example, if $\mathbf{B}^s = 0$ we obtain

$$g_0(t) = \int d^3B \rho(\mathbf{B}) G_z(t) \quad (13) \\ = \frac{1}{3} + \frac{2}{3} (1 - \Delta^2 t^2) \exp(-\frac{1}{2} \Delta^2 t^2).$$

This relaxation function is known as the static Kubo-Toyabe.

If we now take the field hops into account, then the polarization at the measured time t contains contributions from muons that experience no hops at all, those that experience one hop, two hops and so on. The probability that the field stays unchanged during the time $t_{i+1} - t_i$ is given by $\kappa(t_{i+1} - t_i)$. For Markovian processes we have

$$\kappa(t) = e^{-\nu t}. \quad (14)$$

It should be pointed out that this type of dynamical process (Markovian) leads to an exponential decay of the time-dependent field-field correlation function $\langle \mathbf{B}(t) \cdot \mathbf{B}(0) \rangle$.

The averaged polarization is obtained by taking the sum over all possible number of hops, weighted by their probability.[10] Since the probability density for n hops between $[t_1, t_1 + dt_1], \dots, [t_n, t_n + dt_n]$ is

$$\prod_{i=1}^n \exp[-\nu(t_i - t_{i-1})] \nu dt_i = \nu^n \exp(-\nu t) \prod_{i=1}^n dt_i$$

we get

$$P_z(t) = e^{-\nu t} [g_0(t) + \nu \int_0^t dt_1 g_1(t_1, t) + \nu^2 \int_0^t dt_2 \int_0^{t_2} dt_1 g_2(t_1, t_2, t) + \dots] \quad (15)$$

where $g_n(t_1, \dots, t_n, t)$ is the polarization function given that the muon hops at t_1, \dots, t_n . If we now assume that the fields at different time intervals are uncorrelated, and that during each time interval the polarization propagates according to the static function $g_0(t)$ we have

$$g_n(t_1, \dots, t_n, t) = \prod_{i=1}^{n+1} g_0(t_i - t_{i-1}). \quad (16)$$

Equation 15 can be further simplified. However, in most cases we end up using numerical techniques at some point in order to obtain $P_z(t)$. Therefore we will not further simplify this equation here (a simple case where Eq. 15 can be solved analytically is discussed in section 2.4). We shall present the results graphically later in chapter 2 where we will compare them with the relaxation function obtained by other methods.

We refer to the polarization function which is obtained by applying the strong collision model to the static Kubo-Toyabe as the dynamical Kubo-Toyabe (DKT). The advantage of the DKT is that it is very practical for data analysis since it is not limited to a specific range of parameters. In real systems, where the dominant source of relaxation often varies with temperature between the dynamic and the static, the ability to account for the muon spin relaxation with a theory which treats both sources on the same footing, is very useful.

2 A New Look at Muon Spin Relaxation

The first apparent weakness of the traditional muon spin relaxation formalism and the DKT described in the previous chapter is that we cannot find an analytical result from which we can easily see the interplay between the different parameters Δ , ν , and \mathbf{B}^S . In addition, in the strong collision model, the local field and the hop rate are not traced back to the magnetic system and cannot be connected easily to other types of measurements. These problems are dealt with in this chapter. We start by developing a perturbation theory with which we can treat the problem of muon spin relaxation more rigorously. Like the DKT, this theory has its advantages and weaknesses. On one hand, it leads to an analytical result (AR), but on the other hand, as usual in perturbation expansion, this result is limited to a specific range of parameters.

After developing the theoretical tools, we use them to study four different types of relaxation in antiferromagnets. In 2.1 we discuss the relaxation when the local field is random, as in an antiferromagnet (AFM) at temperatures above the Néel temperature (T_N). In 2.2 we study the relaxation at the critical region ($T \rightarrow T_N$). In this section we also use neutron scattering measurements of the dynamical fluctuation in MnF_2 (an AFM) to test our theoretical results. In 2.3 we discuss the low temperature regime $T \rightarrow 0$ and predict a possible new kind of relaxation process which is unique to muons in an AFM. In section 2.4 we describe muon diffusion in an AFM (using the strong collision model). Finally, in section 2.5 we give some concluding remarks.

We write the Hamiltonian describing a muon in a magnetic environment as

$$\mathcal{H} = \mathcal{H}_c - \boldsymbol{\mu} \cdot \mathbf{B}. \quad (17)$$

where \mathcal{H}_c represents the Hamiltonian of the crystal lattice and its electrostatic interaction with the μ^+ , \mathbf{B} is the local field at the muon site, and $\boldsymbol{\mu}$ is the muon magnetic moment. The local field \mathbf{B} is generated by both the local spins \mathbf{S}^j and the external field \mathbf{B}^{ext} . The field \mathbf{B} can be written in terms of $S_{\pm} = S_x \pm iS_y$, and S_z as

$$B_{\nu} = B_{\nu}^{\text{ext}} + \sum_{j\nu'} A_{\nu\nu'}^j \cdot S_{\nu'}^j, \quad (18)$$

where the index j of the tensor \mathbf{A}^j runs over the neighbors of the muon, and the indices ν and ν' represent $+$, $-$ and z . The muon magnetic moment in Eq. 17 is given by

$$\boldsymbol{\mu} = \frac{1}{2} \hbar \gamma_m \boldsymbol{\sigma}$$

where γ_m is the muon gyromagnetic ratio and $\boldsymbol{\sigma}$ are the three Pauli matrices. The decomposition of the Hamiltonian according to Eq. 17 assumes that the presence of

the muon does not influence the magnetic interaction between the ionic moments. This assumption rests on the agreement between measurement of magnetic properties (like order parameter) made by μ SR and other techniques.

In all the cases presented here, the field operator \mathbf{B} can be broken into two parts as

$$\mathbf{B} = \mathbf{B}^s + \mathbf{B}^d(t) \quad (19)$$

where $[\mathcal{H}_c, \mathbf{B}^s] = 0$ and the sample and time average of $\mathbf{B}^d(t)$ is zero. The two fields \mathbf{B}^s and \mathbf{B}^d have a simple interpretation: \mathbf{B}^s represents the average static part of the internal field and \mathbf{B}^d represents the dynamical part. In our discussion here, \mathbf{B}^s results from either the external field or from the frozen part of the ionic spins in the sample while \mathbf{B}^d stems from the fluctuating part of the ionic spins. We further simplify the problem by either orienting the external field or the sample in such a way that the static field direction will coincide with the beam direction $\hat{\mathbf{z}}$ which is also the direction of the initial muon polarization. This configuration is known as the longitudinal field configuration (see section 1.1.2).

In the case where $\mathbf{B}^d(t)$ changes on a time scale much longer than the muon lifetime (the static case), relaxation occurs due to dephasing since different muons experience different magnetic fields and therefore precess with different frequencies. However, in the static case not all the muons precess, since some of them reside in sites where the local field points either parallel or antiparallel to their initial spin direction. In fact, when $\mathbf{B}^s = 0$, the relative number of muons experiencing such a field is 1/3. These muons do not depolarize and $P_z(t)$ recovers to 1/3 at $t \rightarrow \infty$. This effect is easily seen from Eq. 13. With the application of an external longitudinal field (or when a spontaneous field is present) the relative number of muons experiencing a field parallel to their polarization increases and, as a result, the terminal value of the polarization increases.

In the case where $\mathbf{B}^d(t)$ changes on a time scale much shorter than the muon lifetime (the dynamic case) relaxation occurs, according to perturbation theory, due to the absorption of energy quanta by the muon spin Zeeman levels, resulting in a spin flip. In this case the relaxation depends on the system's spectral density at the muon Larmor frequency

$$\omega_s = \gamma_m B_s. \quad (20)$$

A perturbation treatment for dealing with muon relaxation was developed by McMullen and Zaremba (MZ) and is reviewed in appendix A.[11] In their notation the polarization $P_z(t)$ is written as a perturbation series

$$P_z(t) = \langle \sigma_z(t) \rangle_{(0)} + \langle \sigma_z(t) \rangle_{(1)} + \langle \sigma_z(t) \rangle_{(2)} \quad (21)$$

where

$$\langle \sigma_z(t) \rangle_{(0)} = P_z(0), \quad (22)$$

$$\langle \sigma_z(t) \rangle_{(1)} = 0, \quad (23)$$

$$\langle \sigma_z(t) \rangle_{(2)} = P_z(0) \frac{-\gamma_m^2}{4} \int_0^t d\tau (t - \tau) \times \quad (24)$$

$$(e^{i\omega_s \tau} \Phi_{+-}(\tau) + e^{-i\omega_s \tau} \Phi_{-+}(\tau))$$

and where

$$\Phi_{\nu\nu'}(t' - t'') = \langle B_\nu^d(t') B_{\nu'}^d(t'') + B_{\nu'}^d(t'') B_\nu^d(t') \rangle_0. \quad (25)$$

In these equations $B_\pm^d = B_x^d \pm iB_y^d$, and $\langle \rangle_0$ is the thermal average with respect to the states of the system in the absence of the muon. In order to complete the calculation we need to specify the time dependence of the correlation function $\Phi_{ij}(\tau)$. This dependence changes considerably between the paramagnetic state, the critical region, and low temperatures and we consider each region separately.

2.1 The Paramagnetic State ($T \gg T_N$)

At high temperatures the field-field correlation function is expected to drop to zero as time goes by. If we assume that the dynamic is governed by Markovian processes, we can write the time dependence of $\Phi(\tau)$ as

$$\Phi_{+-}(\tau) = \Phi_{-+}(\tau) = 4(\Delta^2/\gamma_m^2) \exp(-\nu\tau) \quad (26)$$

where Δ/γ_m is the RMS of the instantaneous field distribution, and ν is the inverse correlation time. Using this expression we notice that Eq. 21 is an expansion in products of the internal magnetic field, which is on the scale of Δ , and time, which is on the scale of $1/\nu$. Therefore, it is an expansion in Δ/ν and is expected to be a good approximation for $\Delta/\nu < 1$. We also expect Eq. 21 to give an accurate account of the relaxation at $\nu t < 1$ since the n th term in Eq. 21 involves n integrations in time, and its contribution is proportional to the volume of integration $(\nu t)^n$. The requirements on the parameter ν prevent us from taking the limits $\nu \rightarrow 0$ and $t \rightarrow \infty$ simultaneously. Therefore in the perturbation theory we cannot discuss the static fluctuation case at $t \rightarrow \infty$ and we do not expect to find the 1/3 recovery in this theory.

If we now write

$$P_z(t) = P_z(0) \exp(-\Gamma(t)t) \quad (27)$$

expand Eq. 27 in powers of Γ , and compare it with Eq. 21 after the integration, we find that

$$\Gamma(t)t = \frac{2\Delta^2}{(\omega_s^2 + \nu^2)^2} \{ [\omega_s^2 + \nu^2] \nu t + [\omega_s^2 - \nu^2] \times$$

$$[1 - e^{-\nu t} \cos(\omega_s t)] - 2\nu \omega_s e^{-\nu t} \sin(\omega_s t) \} \quad (28)$$

which is our desired analytic result. We can see from this formulation that in general, the polarization relaxes; however some oscillations of frequency ω_s exist near $\nu t \rightarrow 0$.

We now examine the behavior of Eq. 28 in three limits: (I) zero static field ($\omega_s \rightarrow 0$), (II) the fast fluctuation regime ($\nu t \rightarrow \infty$ and $\nu > \Delta$), and (III) early times ($\nu t \rightarrow 0$ and $\omega_s t \rightarrow 0$).

(I) In the zero static field limit we find that Eq. 28 simplifies to

$$\Gamma(t)t = \frac{2\Delta^2}{\nu^2}(e^{-\nu t} - 1 + \nu t). \quad (29)$$

This relaxation form is equivalent to the well known Abragam relaxation function for the transverse field configuration, apart from an overall factor of 2. This factor is expected since in the longitudinal configuration both \mathbf{x} and \mathbf{y} fluctuations contribute to the relaxation, whereas in the transverse configuration only fluctuations in the \mathbf{z} direction cause relaxation.

(II) In the fast fluctuation limit we find

$$\Gamma(t)t = \frac{2\Delta^2\nu}{\omega_s^2 + \nu^2}t \quad (30)$$

and the relaxation has an exponential shape. The relaxation rate Γ (also known as $1/T_1$) is simply given by the Fourier transform of Eq. 26 evaluated at ω_s . This demonstrates how the relaxation rate, in the fast fluctuation limit, depends on the spectral density at the Larmor frequency. In fact in the fast limit, and when the system is symmetric with respect to the interchange of the $\hat{\mathbf{x}}$ and $\hat{\mathbf{y}}$ axis, it is possible to show (see appendix A), using Eq. 21, that

$$\frac{1}{T_1} = \int_0^\infty d\tau \cos(\omega_s \tau) \Phi(\tau) = \tilde{\Phi}(\omega_s) \quad (31)$$

The relaxation rate given in Eq. 30 is the same as the one obtained by the DKT theory in the fast fluctuation limit.[10] Since the muon lifetime ($2.2 \mu\text{sec}$) restricts the value of t to less than $10 \mu\text{sec}$, the fast limit is valid only for fluctuations $\nu \gg 0.1 \mu\text{sec}^{-1}$.

(III) In the early time limit we find

$$\Gamma(t)t = \Delta^2 t^2 + \mathcal{O}(t^3) \quad (32)$$

producing a Gaussian relaxation. We see that the relaxation at early times is independent of both the external longitudinal field and the fluctuation rate; it depends only on the RMS of the field distribution. In this case the dynamical Kubo-Toyabe and the analytical results also agree.[10] A typical experiment limits the time range to $t > 10 \text{ nsec}$ (see 1.1.4); therefore, the early time limit materializes only if $\nu \ll 0.1 \text{ nsec}^{-1}$ and $B_s \ll 1 \text{ T}$.

As mentioned earlier, Eq. 28 is expected to give a good description of the relaxation for $\Delta/\nu < 1$; at the

most we expect Eq. 28 to work for $\nu = \Delta$. In Fig. 8a we present the relaxation obtained in this condition for several longitudinal fields [$\mathbf{B}^s = (\omega_s/\gamma_m)\hat{\mathbf{z}}$]. For comparison we also show in Fig. 8b the relaxation obtained under the same conditions with the DKT as previously described.

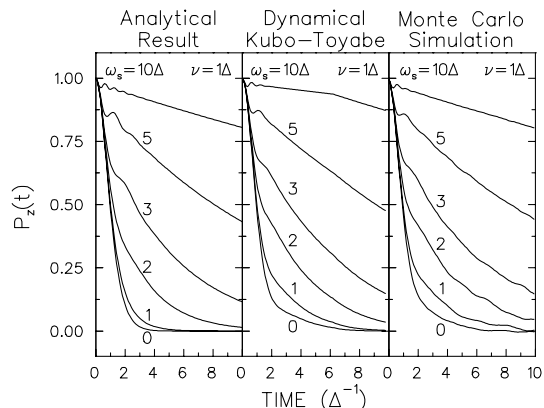


Figure 8: Muon relaxation function in the longitudinal field configuration obtained in three different models: (a) the perturbation expansion (Analytical Result), (b) the dynamical Kubo-Toyabe with a Gaussian field distribution, and (c) Monte Carlo simulations described in the text. The static longitudinal field is given by $\mathbf{B}^s = (\omega_s/\gamma_m)\hat{\mathbf{z}}$.

In Fig. 9 we present the polarization at $B^s = 0$ and several values of ν as obtained from Eq. 28. Again, for comparison we also show in this figure the result of the DKT for the zero field case.

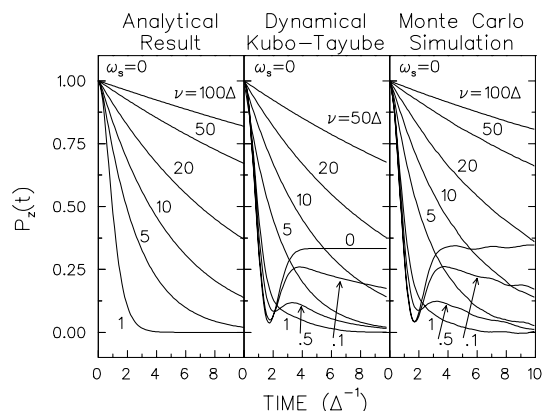


Figure 9: Muon relaxation function in zero external field obtained in three different models: (a) the perturbation expansion (Analytical Result), (b) the dynamical Kubo-Toyabe with a Gaussian field distribution, and (c) Monte Carlo simulations described in the text.

In Figs. 8c and 9c we depict the relaxation function

obtained using Monte Carlo (MC) simulations. The MC method is based on directly integrating the equation

$$\frac{d\mathbf{P}(t)}{dt} = \gamma_m [\mathbf{P}(t) \times (\mathbf{B}^d(t) + B^s \hat{\mathbf{z}})] \quad (33)$$

where

$$\mathbf{P}(0) = \hat{\mathbf{z}}.$$

The field $\mathbf{B}(t)$ is determined in a cyclic order with two steps. In the first step a field \mathbf{B}^d is selected randomly with distribution $\rho(\mathbf{B}^d)$; in the second step a time t is selected randomly with distribution $-\dot{\kappa}(t)$. The field is kept constant during the time t after which we return to the first step. The final polarization function is obtained by averaging over an ensemble of separate muons. The simulations shown in these figures were made using 10000 fictitious muons in a Gaussian field distribution for \mathbf{B}^d (as in Eq. 12) and $\kappa(t) = \exp(-\nu t)$ (as in Eq. 14).

We note that oscillations near $\nu t \rightarrow 0$ are present in all three methods, and that the early time behavior has a Gaussian shape independent of ω_s . In the DKT and MC we can obtain the relaxation for $\nu < \Delta$ as well and clearly see the recovery to 1/3. It is clear from the figure that as the fluctuations become very fast, the field experienced by the muon is very ineffective in depolarizing its spin. In Fig. 10 we compare the three methods and observe that the DKT resembles the simulation more closely in a low static field, while the analytical result better describes the simulation in a high static field. We also observe that the AR relaxes somewhat faster than the DKT function and is harder to decouple with a longitudinal magnetic field. Otherwise, the three methods yield very similar results even for values of the expansion parameter Δ/ν approaching 1; in fact, they are probably experimentally indistinguishable when we consider the typical resolution of the μ SR technique.

2.2 Critical Region ($T \rightarrow T_N$)

In this section we show that the muon $1/T_1$ in the ordered state ($T < T_N$) of the antiferromagnet MnF_2 can be accounted for by the sum of host spin fluctuations measured by neutron scattering. For this discussion we first adopt Moriya's [12] ideas originally developed for Nuclear Magnetic Resonance (NMR) and apply them to the case of a positive muon in this compound. The starting point is the breaking of the solid spins into two parts: static and dynamic, namely,

$$\mathbf{S}^j = \langle \mathbf{S}^j \rangle + \delta \mathbf{S}^j. \quad (34)$$

By substituting Eq. 34 into Eq. 18 (taking $\mathbf{B}^{\text{ext}} = 0$), we can relate the static part of the field \mathbf{B}^s to $\langle \mathbf{S}^j \rangle$ and the dynamic \mathbf{B}^d part to $\delta \mathbf{S}^j$. In MnF_2 \mathbf{B}^s coincides with the easy $\hat{\mathbf{c}}$ axis and both can be aligned with the initial polarization.[13]

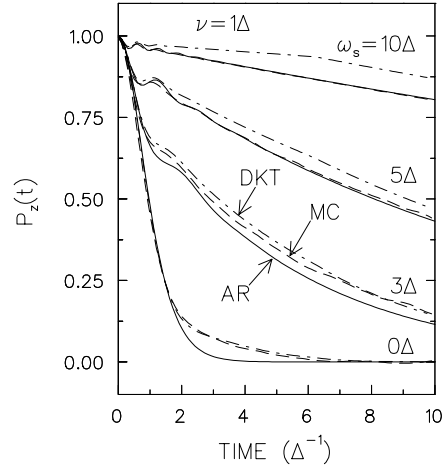


Figure 10: The analytic result (AR) obtained by the perturbation expansion compared with the dynamical Kubo-Toyabe (DKT) relaxation function with a Gaussian field distribution, and Monte Carlo (MC) simulation for several static longitudinal fields $\mathbf{B}^s = (\omega_s/\gamma_m)\hat{\mathbf{z}}$.

The time dependent correlation function defined in Eq. 25 can now be written in terms of the spin correlation according to

$$\Phi_{\nu\nu'}(\tau) = \sum_{jj'\kappa\kappa'} A_{\nu\kappa}^j A_{\nu'\kappa'}^{j'} \langle \{ \delta S_{\kappa}^j(\tau), \delta S_{\kappa'}^{j'}(0) \} \rangle. \quad (35)$$

It is customary to introduce the Fourier transform in space of the spin variable. In MnF_2 there is only one magnetic ion per unit cell, and we can define

$$\mathbf{S}^{\mathbf{k}} = N^{-1/2} \sum_j \mathbf{S}^j \exp(i\mathbf{k} \cdot \mathbf{R}^j), \quad (36)$$

where \mathbf{k} is a wavevector and N the number of magnetic ions. Using Eq. 36, the correlation between the j th and the j' th spins can be expressed as

$$\langle \{ \delta S_{\kappa}^j(\tau), \delta S_{\kappa'}^{j'}(0) \} \rangle = N^{-1} \times \sum_{\mathbf{k}} \langle \{ \delta S_{\kappa}^{\mathbf{k}}(\tau), \delta S_{\kappa'}^{-\mathbf{k}}(0) \} \rangle \exp(-i\mathbf{k} \cdot [\mathbf{R}^j - \mathbf{R}^{j'}]). \quad (37)$$

Combining equations 31, 35, and 37 we find

$$1/T_1 = (1/2N) \int_{-\infty}^{\infty} d\tau \cos(\omega_s \tau) \times \sum_{\mathbf{k}} \sum_{\kappa\kappa'} D_{\kappa\kappa'}(\mathbf{k}) \langle \{ \delta S_{\kappa}^{\mathbf{k}}(\tau), \delta S_{\kappa'}^{-\mathbf{k}}(0) \} \rangle. \quad (38)$$

where

$$D_{\kappa\kappa'}(\mathbf{k}) = \sum_{jj'\nu\nu'} A_{\nu\kappa}^j A_{\nu'\kappa'}^{j'} \exp(-i\mathbf{k} \cdot [\mathbf{R}^j - \mathbf{R}^{j'}]).$$

Most of the contribution to the sum in Eq. 38 is from \mathbf{k} near the staggered magnetization wave vector \mathbf{k}_0 of the antiferromagnetic order. We therefore shift the origin of the Brillouin zone to the point \mathbf{k}_0 , and define $\mathbf{q} = \mathbf{k} - \mathbf{k}_0$. In the most general case, both longitudinal and transverse fluctuations contribute to $1/T_1$. However, as we will show, longitudinal fluctuations do not contribute to $1/T_1$ in the case of MnF_2 . We therefore conclude that in this case $D_{33}(\mathbf{q}) = 0$. Since \mathbf{A}^j is very short range, as a function of j , and since the correlation function peaks at $q = 0$ [14], we can approximate $D_{\nu\nu'}(\mathbf{q})$ in the sum of Eq. 38 as independent of q for small q . Similar approximations were used by De Renzi *et al.* [14] in their work on μSR linewidth in MnF_2 at $T > T_N$.

Defining the scattering function

$$S_{\perp}(\mathbf{q}, \omega) = \int_{-\infty}^{\infty} dt \cos(\omega t) \langle \{ \delta S_{+}^{\mathbf{q}}(t), \delta S_{-}^{\mathbf{q}}(0) \} \rangle \quad (39)$$

and using the symmetry of MnF_2 under the interchange of x and y , we arrive at

$$1/T_1 = D \int S_{\perp}(\mathbf{q}, \omega_s) d^3q \quad (40)$$

where D is a constant independent of temperature, and the sum over \mathbf{q} is replaced by an integral.

The temperature dependence of the right hand side of Eq. 40 enters in two places: one is the temperature dependence of the scattering function $S_{\perp}(\mathbf{q}, \omega)$, and the other is the temperature dependence of the static local field ω_s .

μSR measurements in MnF_2 were performed by Uemura *et al.*, and are fully described in Ref. [13]. They used two experimental configurations in zero external field: (a) the transverse configuration (TC) in which the initial muon polarization was perpendicular to the \hat{c} axis and (b) the longitudinal configuration (LC) in which the initial polarization was parallel to \hat{c} . In TC they measured the precession frequency of the muon moment in the static local field at $T < T_N$, and thus obtained $\omega_s(T)$. Two frequencies were found in the μSR spectra and assigned to two different muon sites. In LC they measured the relaxation rate of the muon polarization in temperatures both above and below T_N . Here again two relaxation time scales were observed. The fast relaxation was attributed to muons at the high field site. We are concerned here only with the spin lattice relaxation of muons in the site with the higher field since the data is less scarce. In Fig. 11 we show the fast $1/T_1$ as a function of temperature.[13] The relaxation rate of the muon at the Néel temperature is $\sim 14 \mu\text{sec}^{-1}$; the precession frequency at $T \rightarrow 0$ in the TC is $\omega_s = 2\pi \times 1.3$ GHz. If we make the approximation $\Delta \sim \omega_s(0)$ we find (using Eq. 30) $\Delta/\nu \sim 1/\omega_s T_1 \sim 10^{-3}$, and can safely say that Eq. 31 is valid in this case. It is also obvious from the figure that at

temperatures higher than the Néel temperature $1/T_1$ is independent of T . This is clear evidence that $1/T_1$ is independent of the longitudinal spin fluctuation, since these fluctuations are known to undergo critical slowing down as discussed in.[13, 15] The same conclusion was drawn from the study of De Renzi *et al.* at $T > T_N$. [14]

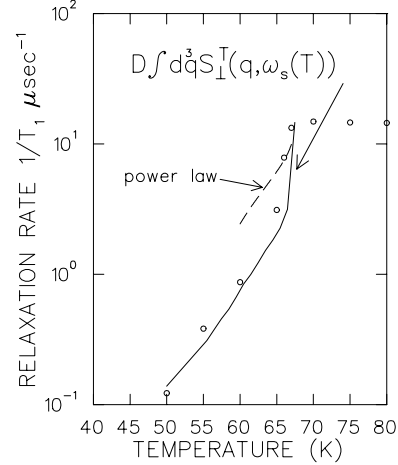


Figure 11: μSR relaxation rate measurements in MnF_2 , compared with model calculation and power law as described in the text.

Schulhof *et al.* [15] measured the scattering function $S_{\perp}(\mathbf{q}, \omega)$ in MnF_2 near T_N by neutron scattering. They showed that near T_N , $S_{\perp}(\mathbf{q}, \omega)$ could be approximated by

$$S_{\perp}(\mathbf{q}, \omega) \propto \frac{1}{\kappa_{\perp}^2 + \mathbf{q}^{*2}} \left(\frac{\Gamma_{\perp}}{\Gamma_{\perp}^2 + (\omega - \omega_0)^2} + \frac{\Gamma_{\perp}}{\Gamma_{\perp}^2 + (\omega + \omega_0)^2} \right) + O((\omega_s/T)^2) \quad (41)$$

where ω_0 and Γ_{\perp} are functions of the temperature and are given by

$$\begin{aligned} \omega_0(T, q) &= a_0(T) + b_0(T)(q^*)^2, \\ \Gamma_{\perp}(T, q) &= a_{\perp}(T) + b_{\perp}(T)(q^*)^2, \\ q^{*2} &= q_x^2 + q_y^2 + (c/a)^2 q_z^2, \end{aligned} \quad (42)$$

where a and c are the lattice parameters. From their data we derive $b_0(T)$, $a_{\perp}(T)$, and $b_{\perp}(T)$, as shown in Fig. 12. The solid lines represent fits to power laws made just for interpolating the neutron scattering data. The functions describing these lines are shown in the figures. The gap energy $a_0(T) = 1.36(1 - T/T_N)^{0.37}$ meV, and $\kappa_{\perp} = 0.054(5) \text{ \AA}^{-1}$ is explicitly given by the authors.[15] This form of $S_{\perp}(\mathbf{q}, \omega)$ and $\omega_s(T)$ is then used to numerically integrate the right hand side of Eq. 40 at various temperatures. The integral was performed in a cube, and the range of integration was limited by the available neutron data ($q < 0.3 \text{ \AA}^{-1}$).

The temperature dependence of this integral was then scaled by a factor D so that both sides of Eq. 40 agree at T_N . The result of the computed $1/T_1$ is shown in Fig. 11 by the solid line. In this figure we can see that the calculated line agrees very well with the measured data. This is the first demonstration that the muon relaxation rate results from host spin fluctuations according to Eq. 40 in the ordered state of a magnet. The broken line in this figure represents a fit to a power law. It is clear that such a power law fits the data very poorly. However, the agreement with Eq. 40 extends over a wide temperature range. Thus, Eq. 40 provides us with a powerful tool to check theories of magnetic interaction, since it contains more information than merely critical exponents.

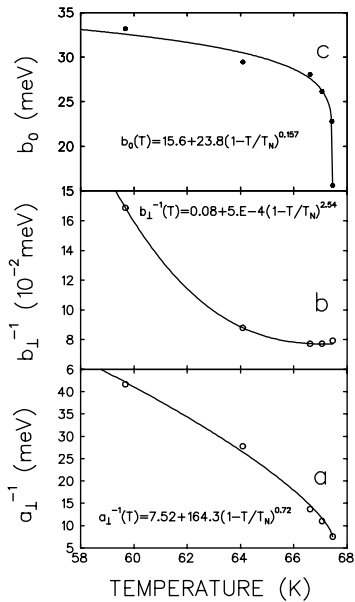


Figure 12: Fitted parameters from neutron scattering measurements.

2.3 Relaxation Mechanism ($T \rightarrow 0$)

In this section we concentrate on the low temperature region, namely $T/T_N \rightarrow 0$. In this region it is possible to describe the dynamics in terms of a quasi-particle excitation and relaxation mechanism. Here we will examine the possible existence of a unique kind of muon spin relaxation mechanism; as a result of this mechanism, the muon spin relaxation rate ($1/T_1^\mu$) is expected to exhibit a temperature dependence that is different from that of the spin of a nuclei ($1/T_1^N$) with the same type of coupling to the magnetic system. The relaxation mechanism suggested here has not yet been observed in a real system but, as we shall see, the required conditions can be met in some materials.

First let us briefly review the traditional theory of

muon (or nuclear) spin relaxation mechanisms. For simplicity we concentrate on the case of a muon which interacts with the moment of a single ion, namely, $B_\nu = A_{\nu\nu'} S_{\nu'}$. Rewriting \mathbf{S} in the spin wave theory form (see appendix C Eq. 107) breaks the field \mathbf{B} into static and dynamic parts. The static part is a consequence of the operator free term (S) in the expression for S_z . The dynamic part includes all of the linear and bilinear terms in creation and annihilation operators. For the evaluation of the relaxation rate we convert in appendix B, Eq. 31, to the thermally averaged Fermi golden rule

$$\frac{1}{T_1} = \frac{\pi \hbar \gamma_m^2}{2} \sum_{i\pm} \frac{e^{-\beta E_i}}{z} \times \sum_f |\langle f | B_-^d | i \rangle|^2 \delta(E_i - E_f \pm \hbar \omega_s) \quad (43)$$

which depends on the matrix element of B_-^d . B_-^d , in turn, depends on both S_+ and S_- , or on $S_z - S$. The matrix elements are evaluated between the initial and final magnon configuration $\{n(\mathbf{k}, p)\}$, where $n(\mathbf{k}, p)$ indicates the number of magnons in an excited state of wave vector \mathbf{k} and polarization p .

Since the S_- and S_+ operators involve single creation or annihilation operators, they lead to relaxation through the absorption or creation of a magnon with an energy $\hbar \omega_s$. The relaxation rate therefore involves the factor $n(\hbar \omega_s)$ (the number of magnons with this energy). The S_z operator, on the other hand, involves both a creation and annihilation operator and leads to relaxation through the annihilation of one magnon and the creation of another. This scattering-like contribution to the relaxation rate involves $n(E)[n(E') + 1]$, the product of the number of magnons with the incoming energy (E) and outgoing energy (E'). The energy difference between the incoming and the outgoing magnons must be $\hbar \omega_s$. This type of process is known as magnon Raman scattering (MRS).

If, for example, $\mathbf{A} = A \delta_{\nu\nu'}$, and if we consider contribution only from absorption, we get

$$\frac{1}{T_1} \propto \hbar (\gamma_m A)^2 \int u_k^2 n(k) \delta(E_p(\mathbf{k}) - \hbar \omega_s) d^d k \quad (44)$$

where $E_p(\mathbf{k})$ is the energy of a magnon with wave vector \mathbf{k} and polarization p and u_k is given in appendix C. By looking at the low temperature limit (where we let $k \rightarrow 0$ and $u_k \rightarrow 1/k^{1/2}$), and by taking the magnon dispersion relation (Eq. 114)

$$E_p(\mathbf{k}) = \theta_N b k \quad (45)$$

we find

$$\frac{1}{T_1} = D (\gamma_m A)^2 \frac{\omega_s^{d-2}}{(\Theta_N/\hbar)^{d-1}} n(\hbar \omega_s) \quad (46)$$

where D is a factor on the order of unity and d is the dimensionality. We see that the relaxation rate is finite at $\omega_s \rightarrow 0$ for $d = 2$. For $d = 3$, $1/T_1$ goes to zero at $\omega_s \rightarrow 0$. In both cases the relaxation rate decreases with decreasing temperature.

As can be seen from Eq. 46 the magnitude of the relaxation rate depends on the ratio $\hbar\gamma_m A$ to Θ_N . In a typical local field of 1 kG and ordering temperature of 10 K this ratio is 10^{-7} μsec (in 3D) which is undetectably small. Thus, in order to account for the relaxation of muon spins in AFMs we have to look for a different relaxation mechanism.

Van Kranendonk and Bloom found that the nuclear T_1^N relaxation mechanism, at temperatures much smaller than the Néel temperature T_N , is indeed dominated by magnon Raman scattering (MRS).[16] They argued that at such temperatures one may ignore not only direct absorption but also the phonon contribution, provided that T_N is smaller than the Debye temperature Θ_D . An explicit calculation carried out by Moriya supports these assumptions.[17] It was later demonstrated quantitatively by Kaplan *et al.* that the MRS model can explain very well the relaxation rate of ^{19}F spin in MnF_2 at $T \rightarrow 0$.[18]

However, the implanted muon is coupled electrostatically to its neighbors in a different manner than a nucleus, and has a much smaller mass. This can result in vibration frequencies of the μ^+ different from those of the nuclei, which in turn allows additional sources of $1/T_1$ to become important. The relaxation mechanism pursued here applies in cases where the muon vibration energy levels' spacings are of the same order of magnitude as the energy carried by a magnon. In these cases muon T_1 relaxation could proceed via the absorption of a magnon, excitation of the muon to a higher vibrational level and a spin flip. This excitation-assisted spin flip process can coexist with the previously studied MRS process.

When a narrow field distribution at the muon site (at $T \rightarrow 0$ in an AFM) is observed, one can assume that there is a muon bound state. An estimate of the energy scale of the muon vibration energy levels in a particular compound can be obtained from muon diffusion. For example, thermally activated muon diffusion, with an activation energy of $E_a = 0.39(1)$ eV, will be shown in section 2.4 to take place in the ordered state of the so-called Infinite Layer AFM $\text{Ca}_{0.86}\text{Sr}_{0.14}\text{CuO}_2$.[7] The vibrational energy spacings are only a fraction of E_a , and can be estimated by $\sqrt{2\hbar^2 E_a / mL_{\text{eff}}}$, where $m = 105.66$ MeV/ c^2 is the muon mass and L_{eff} is some effective length scale of the potential well. For $L_{\text{eff}} = 3$ Å (the lattice parameters are $a = 3.8$ and $c = 3.2$ Å) the energy spacings are on the order of 0.05 eV. It so happens that the Néel temperature of this compound is also 0.05 eV (540 K) which is the expected energy scale for magnons. Thus we believe that the conditions

for the excitation-assisted spin flip relaxation process could exist in this compound.

The model used here to account for the temperature dependence of $1/T_1^\mu$ assumes that the muon, after entering the sample, is trapped instantaneously in a crystallographically unique electrostatic potential well. Once the μ^+ is in this well, the Hamiltonian \mathcal{H}_c is given by $\mathcal{H}_c = \mathcal{H}_{ss} + V(\mathbf{r})$ where \mathcal{H}_{ss} describes the AFM spin system (here we use the Heisenberg model), and $V(\mathbf{r})$ describes the electrostatic interaction of the muon with the solid. The magnetic field can be written as in Eq. 18 but with the matrix $\mathbf{A}^j(\mathbf{r})$ depending on the displacement \mathbf{r} of the μ^+ from its equilibrium position. It is this dependence which couples the magnons to the vibrational levels of the μ^+ in its well. A schematic view of the excitation-assisted spin flip process is provided in Fig. 13.

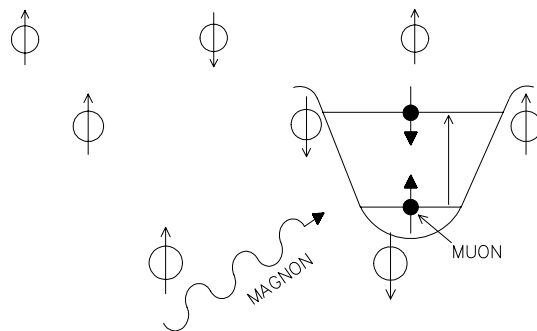


Figure 13: A schematic view of the excitation-assisted spin flip process

In order to simplify the problem, the quantization axis of the AFM electronic spins, the direction of the field at the μ^+ site, and the initial muon polarization, are taken to align with the \hat{c} axis. The relaxation processes are accounted for by two expansions: $A^j(\mathbf{r})$ is expanded in terms of \mathbf{r} around $\mathbf{r} = 0$ and \mathbf{S} is expressed in terms of creation ($M_{\mathbf{k}p}^\dagger$) and annihilation ($M_{\mathbf{k}p}$) operators of magnons, as given by spin wave theory described in appendix C; \mathbf{k} and p are the wave vector and polarization of the magnon. These expansions give rise to various terms. All terms contributing to the static local field are represented by the observed internal field \mathbf{B}^s . Other terms induce the direct absorption, the MRS, and the excitation assisted spin flip processes. Since the first two processes have been examined elsewhere, only the latter will be considered here.

The model is further simplified by the following two assumptions: I) the potential well is isotropic, II) the muon falls down to its vibrational ground state before its spin relaxes. The second assumption is a consequence of the short stopping time 10^{-10} sec and the expected population of higher vibrational energy lev-

els. Since in our model these energy levels are on the order of T_N , at $T < T_N$ the population of the higher level decreases as $\exp(-T_N/T)$ with decreasing temperature. The focus is therefore on the terms leading to transitions between an initial state of a μ^+ in the vibrational ground state, up spin, and a magnon configuration $\{n(\mathbf{k}, p)\}$, and a final state with the μ^+ in the first excited vibrational state, down spin, and one less magnon.

If ρ_m^+ is the raising operator of the vibrational levels in the m 'th spatial direction, then the important part of the dynamical field operator is given by

$$B_+^d = \sum_{p,m} \sum_{\mathbf{k}} d_{pm}(\mathbf{k}) \rho_m^+ M_{\mathbf{k}p}, \quad (47)$$

where

$$d_{1m}(\vec{k}) = \left(\frac{2s\hbar}{m\omega_v N} \right)^{1/2} \times \left(v_k \sum_i \frac{dA_{-}^i}{dr^m} e^{ikR_i} + u_k \sum_j \frac{dA_{-}^j}{dr^m} e^{-ikR_j} \right)$$

$$d_{2m}(\vec{k}) = \left(\frac{2s\hbar}{m\omega_v N} \right)^{1/2} \times \left(u_k \sum_i \frac{dA_{+}^i}{dr^m} e^{-ikR_i} + v_k \sum_j \frac{dA_{+}^j}{dr^m} e^{ikR_j} \right).$$

The functions u_k and v_k are given in appendix C, $\hbar\omega_v$ is the energy difference between the ground state and the first excited state of $V(\mathbf{r})$, and the indices i and j are taken over the different sub-lattices. In principle, the local field \mathbf{B}^s will cause an energy splitting between the up spin and down spin states, which will result in different relaxation rates on the two sub-lattices. However, the splitting (~ 0.01 K) is much smaller than the typical magnon energy and can be ignored.

The relaxation rate is evaluated by the thermally weighted Fermi golden rule. It is easy to see that the temperature dependence comes only from the average number of magnons with energy $\hbar\omega_v$. The relaxation rate is given explicitly by

$$\frac{1}{T_1} = Kn(\hbar\omega_v) \quad (48)$$

where

$$K = \frac{\hbar\gamma_m^2 V}{(2\pi)^2} \sum_{p,m} \int d^3k |d_{pm}(\mathbf{k})|^2 \delta(E_p(\mathbf{k}) - \hbar\omega_v).$$

The order of magnitude of this mechanism can be estimated at low temperatures ($T \ll T_N$) by taking $n(\hbar\omega_v) \sim \exp(-\hbar\omega_v/k_B T)$ and the long wavelength approximation. In the $k \rightarrow 0$ limit of an ideal Heisenberg antiferromagnet, the following relation is valid

[16]:

$$\sum_{p,m} |d_{pm}(\mathbf{k})|^2 = \frac{s}{2Nbk} F^2$$

The factor $F \sim (\hbar/2m\omega_v)^{1/2} (dA/dr)$ has units of magnetic field, and is of the order of the field fluctuations seen by the muon as it oscillates in the well. The relaxation rate calculated from Eq. 48 in the long wavelength limit obeys an Arrhenius law

$$\frac{1}{T_1} = \frac{Sv}{2\pi b^3} \left(\frac{\hbar\omega_d}{\theta_N} \right)^2 \omega_v \exp(-\hbar\omega_v/k_B T) \quad (49)$$

where $\omega_d = \gamma_m F$, and v is the volume of the cell. This result is in contrast to the T^3 law at low temperatures of the MRS.[16] The excitation-assisted spin flip relaxation mechanism will be important when $\hbar\omega_d/\theta_N$ is large, and the signature of this mechanism is an activation energy of the order of the Néel temperature.

As mentioned earlier, the conditions for the excitation assisted spin flip process exist in $\text{Ca}_{0.86}\text{Sr}_{0.14}\text{CuO}_2$. However we could not experimentally confirm that the muon relaxation in this compound is indeed governed by the model developed here. The main reason for this failure is that at the moment only powder samples exist and we could not separate the different relaxation sources (see 1.2). Therefore, the confirmation of the excitation assisted spin flip process will have to wait for the fabrication of a single crystal.

2.4 Hopping

Another source of dynamic relaxation which occurs in solids is muon diffusion. When diffusion takes place, the muon does not spend its entire life in a single site but actually hops between several sites. In order to include this extra dynamical effect we should replace $\mathbf{B}^d(t)$ by $\mathbf{B}^d(\mathbf{r}(t), t)$ in Eq. 25 where $\mathbf{r}(t)$ now represents the site of the muon at different times. The problem of the relaxation can be worked out with some diffusion model describing $\mathbf{r}(t)$. However, in this section we describe a situation where the muon hops between different sites in the ordered state of an AFM. This problem can be solved analytically with the use of the strong collision model (section 1.3). The relaxation function developed here is also used in chapter 4 to fit μSR data in $\text{Ca}_{0.86}\text{Sr}_{0.14}\text{CuO}_2$ (an AFM) at $T \sim 300$ K where the data clearly indicates that muon diffusion takes place.

We assume that the field changes experienced by the muon spin occur only due to physical site change of the muon itself. Moreover, we say that the muon hopped only if it jumped to a site where the field is opposite to the previous site. After each time the muon hops between such sites the spin polarization starts to rotate in the opposite sense to the rotation before the hop. The polarization resulting from two such hops is demonstrated in Fig. 14.

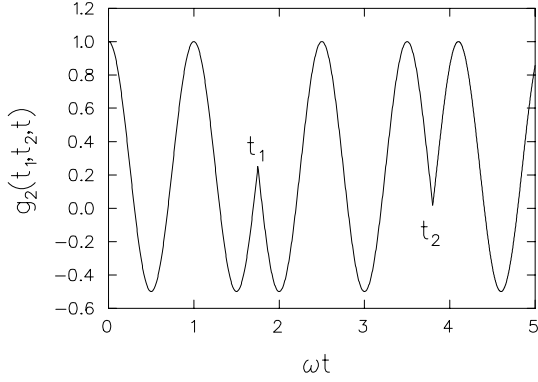


Figure 14: The polarization of a muon that hops at t_1 and t_2 in an antiferromagnet. The angle between the initial polarization and the local field is taken as 30° .

For n hops between sites of opposing field, at times $t_1 < \dots < t_n < t$, the polarization function g_n is given by

$$g_n(t_1, \dots, t_n, t) = \text{Re}\{\cos^2(\theta) + \sin^2(\theta) \exp(i \sum_{i=1}^{n+1} [-1]^{i+1} \omega [t_i - t_{i-1}])\} \quad (50)$$

where $t_{n+1} = t$. In order to evaluate this sum we take the Laplace transform of both sides of Eq. 15,

$$F(s) = \int_0^\infty e^{-st} P_z(t) dt. \quad (51)$$

In this case, the integrals on the right hand side of Eq. 15 decouple and $F(s)$ is given by

$$F(s) = \text{Re} \left(\cos^2 \theta \sum_{n=1} \nu^{n-1} f_0^n(x) + \sin^2 \theta f_\omega(x) (1 + \nu \overline{f_\omega(x)}) \sum_{n=0} \nu^n |f_\omega(x)|^n \right). \quad (52)$$

when $x = s + \nu$ and $f_\omega(x) = 1/(x - i\omega)$. After summing over the geometrical sequences we find

$$F(s) = \cos^2 \theta \frac{1}{s} + \sin^2 \theta \left(\frac{c_+}{s - z_+} + \frac{c_-}{s - z_-} \right) \quad (53)$$

where

$$z_\pm = \frac{1}{2} \pm \frac{\nu(\nu^2 - \omega^2)^{-\frac{1}{2}}}{2}$$

and

$$z_\pm = -\nu \pm (\nu^2 - \omega^2)^{\frac{1}{2}}.$$

It is easy to obtain the inverse Laplace transform of Eq. 53 from which we obtain

$$P_z(t) = \cos^2 \theta + \sin^2 \theta (c_+ e^{z_+ t} + c_- e^{z_- t}). \quad (54)$$

In a powder sample we can replace the $\cos^2 \theta$ with $\frac{1}{3}$ and the $\sin^2 \theta$ with $\frac{2}{3}$ for the powder average.

In Fig. 15 we show $P_z(t)$ in two cases: the fast hopping regime, characterized by $\nu > \omega$, and the slow hopping regime with $\nu < \omega$. For both fast and slow hopping, the relaxation of the 2/3 component at $t \ll 2\pi/\omega$ follows t as $1 - (1/2)\omega^2 t^2$. This quadratic behavior at $t \rightarrow 0$ is expected in a strong collision model and also emerges from the perturbation treatment (Eq. 32). At long times $t \gg 2\pi/\omega$, two limits are of interest: In the very fast hopping limit ($\nu \gg \omega$) the 2/3 component relaxation function is given by $\exp(-\omega^2 t/2\nu)$, similar to the fast limit of the perturbation approach (Eq. 30). In the very slow hopping limit $\nu \ll \omega$, the time dependence of the 2/3 component goes as $\exp(-\nu t) \cos(\omega t)$. In this limit, the relaxation rate can be understood by noting that only the spins of muons that haven't hopped at all will contribute to the polarization at long times; the number of such muons decreases exponentially. If we now include T_1 and T_2 relaxation from other sources, independent of the hopping, we arrive at

$$P_z(t) = \frac{1}{3} e^{-t/T_1} + \frac{2}{3} e^{-t/T_2} (c_+ e^{z_+ t} + c_- e^{z_- t}). \quad (55)$$

This model is not applicable if the sizes of the magnetic domains are smaller than the average length that the muon travels between sites. It also should be noted that hopping between sites of opposite fields ($\nu = \nu_{\uparrow\downarrow}$) is not the total hopping rate because hopping between sites of the same field ($\nu_{\uparrow\uparrow}$) also might occur; if ν_{tot} is the total hopping rate, then $\nu_{tot} = \nu_{\uparrow\downarrow} + \nu_{\uparrow\uparrow}$.

2.5 Summary

We have discussed the depolarization rate of a muon in an antiferromagnet in four different regimes: I) the random field regime which is encountered in either high temperatures ($T \gg T_N$) or in systems where the spins freeze in random orientations, II) the critical regime ($T \rightarrow T_N$) where the physics of the spin system is best described in terms of spin-spin correlation function, III) the low temperature regime ($T \rightarrow 0$) where we can actually distinguish between different relaxation mechanisms, and IV) the hopping regime which can take place at all temperatures. The emerging picture is that when the ionic spins fluctuate very fast ($\nu \gg \Delta$ at $T \gg T_N$) they are not effective in depolarizing the muon spin. Therefore, the relaxation rate in this region is small. As $T \rightarrow T_N^+$ the ionic spins slow down ($\nu \sim \Delta$), they depolarize the muons very effectively, and the relaxation increases. At $T \ll T_N$ the relaxation depends on the amount of energy quanta available to cause spin flips. Since this amount decreases as $T \rightarrow 0$, the relaxation rate is small again. Thus we expect to find a peak in the relaxation rate in systems

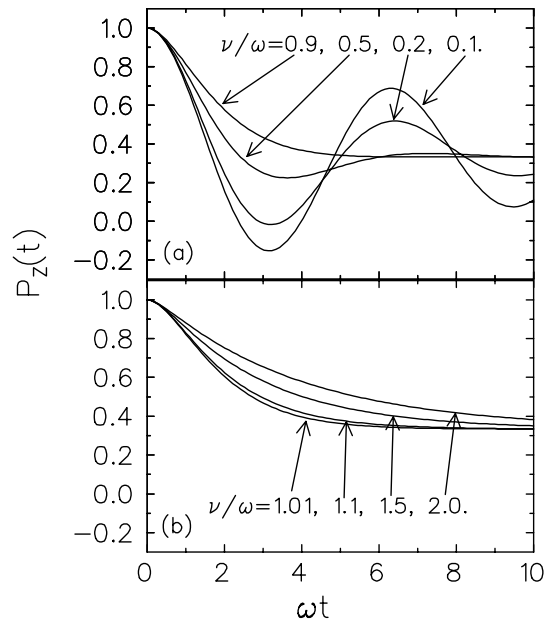


Figure 15: Muon polarization in an antiferromagnet for various ratios of hopping rate ν to rotation frequency ω calculated with the strong collision model. In (a) $\omega > \nu$ and in (b) $\omega < \nu$.

which go through phase transition. This type of behavior was observed in all magnetic systems known to us. It is the breakdown of this very fundamental behavior in systems with kagomé lattice structure which first drew our attention to them. We now turn to review our experiments on these kagomé systems.

3 The Kagomé Lattice

3.1 Introduction

The term “super-degenerate”, in the title of this thesis, refers to antiferromagnetic systems with an exceptionally large number of states in which the classical energy is minimized. These states are sometimes referred to as the degenerate classical ground states. In contrast to most magnets, where the degeneracy stems from the invariance of the energy only under a collective rotation of a macroscopic number of spins, the energy of a super-degenerate antiferromagnet is also invariant under a rotation of a very small number of spins. This extra invariance (symmetry) dramatically increases the number of classical ground states. Since the thermodynamical and dynamical properties of a magnet (at low temperature) are strongly influenced by the degeneracies of the ground state, we expect to find new physics in such systems. In this chapter we explore one such system known as the kagomé lattice and, as expected, encounter numerous unusual effects.

An example of an antiferromagnet whose ground state is invariant only under a rotation of all the spins in the system (a merely degenerate AFM) is the classical Heisenberg model with a Nearest Neighbors (NN) interaction on a cubic lattice. The Hamiltonian of this system is

$$\mathcal{H} = J \sum_{\langle i,j \rangle} \mathbf{S}_i \cdot \mathbf{S}_j \quad (56)$$

where \mathbf{S}_i is a classical unit vector associated with the i 'th site, the sum is taken only over NN, and $J > 0$. This Hamiltonian is rotationally symmetric, and for the system to order magnetically there must be a spontaneous symmetry breaking where the system selects a particular direction ($\hat{\mathbf{z}}$) with which the spins are aligned. The ground state energy (E_g) in this case is independent of the direction $\hat{\mathbf{z}}$, and any collective rotation of all the spins in the system leaves E_g intact. However, once a direction $\hat{\mathbf{z}}$ is selected, any change of spin orientation which involves a finite number of spins could only increase the system's energy. Therefore this system is not super-degenerate.

A system with a super-degenerate ground state is obtained by placing Heisenberg spins on a kagomé lattice. The name “kagomé” is constructed from two Japanese words: kago, which means basket, and mé, which means lattice. The basket (kago) made from woven bamboo strips, is used in Japan to hold goods as large as fruits or as small as candy. The kagomé lattice, shown in Fig. 16, is obtained from the triangular lattice by omitting a spin from every other site on every other line. The energy of the NN Heisenberg model on the kagomé lattice can be minimized by placing the spins on each triangle 120 degrees away from each other, so that

$$\mathbf{S}_A + \mathbf{S}_B + \mathbf{S}_C = 0,$$

where A , B , and C represent the three corners of a triangle.[19] Examples of such spin arrangements are shown in Fig. 16a and b as well as in Fig. 19. However, the spins do not have to be on the same plane as in these figures. For example, the spins to the left of spins C in Fig. 16a could be on a different plane than the spins to their right. The configurations in which the spins are on a single plane are called coplanar states. Now we can see that the interchange of a small group of spins leaves the energy invariant, for example, the spins which are labeled A and B in Fig. 16b (only six spins). It is due to this property that the kagomé system earns the title “super-degenerate” and it is in this system that experimenters and theorists alike study the influence of the high degeneracy on magnetic properties.

Long range order in the kagomé lattice is possible in two configurations known as the $q = 0$ and $\sqrt{3} \times \sqrt{3}$ states. The $q = 0$ configuration, shown in Fig. 16a, is

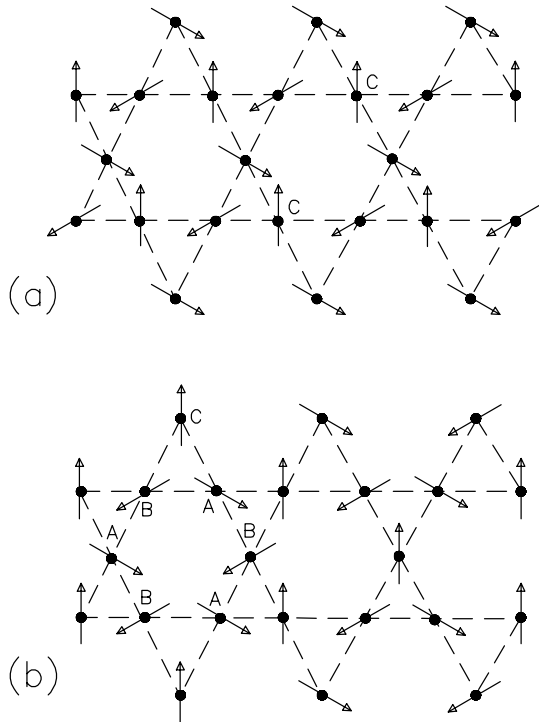


Figure 16: Classical spins on the kagomé lattice with (a) a $q=0$ ground state and (b) a $\sqrt{3} \times \sqrt{3}$ ground state.

obtained by placing the spins along any line which connects nearest neighbors in an alternating sequence (e.g. ABABAB).[20] The name $q = 0$ alludes the fact that in this configuration the periodicity of the atomic and magnetic unit cells coincide. The $\sqrt{3} \times \sqrt{3}$ state, shown in Fig. 16b, is obtained by placing the spins along each such line in a rotating sequence (e.g. ABCABCA).[21] The name $\sqrt{3} \times \sqrt{3}$ pertains to the fact that in this configuration the magnetic unit cell is $\sqrt{3}$ longer than the atomic unit cell.

In an external magnetic field \mathbf{H} , the nature of the Heisenberg kagomé lattice does not change much. In a ground state, the spins on each triangle obey the condition

$$J(\mathbf{S}_A + \mathbf{S}_B + \mathbf{S}_C) - \mathbf{H}/2 = 0.$$

[19] This condition may be satisfied for both canted states, where the three spins in a triangle no longer lie on a single plane, and for planar states where all spins are coplanar with the magnetic field. There are an infinite number of ways of distributing any of these triads over the kagomé lattice, as in the case of zero field. There are also states which contain more than three possible spin orientations. These may be obtained from the $\sqrt{3} \times \sqrt{3}$ state by rotating, for example, spin A and B about the axis defined by $\mathbf{S}_C - \mathbf{H}/2J$. [19] Thus the magnetic field does not remove the infinite ground states' degeneracy (for $H < 6J$). Furthermore, the

magnetization in all of these states is identical.

The first question to be asked about the kagomé system is whether this lattice can support a long range Néel order at $T \rightarrow 0$. This is not a trivial question, since the degeneracy of the classical ground state results in a manifold of states out of which only two are known to possess long range order. Minimizing the classical energy in itself does not necessarily cause the system to favor long range order or even a coplanar configuration. Therefore, we expect the ground state to be either a very dynamical one, or one in which a selection of specific spin configurations would take place by some other mechanism. Two such possible mechanisms are thermal fluctuations (so-called "order by disorder") and quantum fluctuations.

A simple example of the thermal fluctuations selection mechanism is given by considering a single quantum particle in a non-symmetric double potential well, such as in Fig. 17. Both sides of the well have the same minimum energy (the classical ground is doubly degenerate) but the restoring force in the left side is stronger than in the right side. In other words, the frequency of oscillations in the harmonic approximation on the left side (ω_L) is larger than that frequency on the right side (ω_R). As in the kagomé case, we find ourselves unable to decide where the particle would be at finite temperature just from minimum energy consideration. However, the number of excited states between E_g and $E_g + \Delta E$ on the left/right side is $\Delta E/\hbar\omega_{L/R}$, and therefore the density of states is higher on the right side. Since at temperature T the particle will be in states with energy $\Delta E \sim k_B T$, and since there are more such states on the right side, that is where the particle is more likely to be. The selection of the right side should be most dramatic if that side has no restoring force in the harmonic approximation (zero mode), or, better yet, no restoring force to higher orders of approximation.

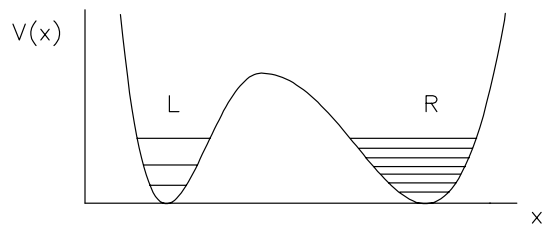


Figure 17: A non-symmetric double potential well. The minimum energy is the same on both sides, but the density of excited levels is higher on the right side.

Returning to the magnetic kagome case, it was shown by Chalker *et al.* [22] that the density of excited states in the harmonic approximation is highest near a coplanar ground state. Therefore, thermal fluctuations should select a coplanar configuration. Among all coplanar

states, both the $\sqrt{3} \times \sqrt{3}$ and the $q = 0$ states are special in that they contain spin deviations with no restoring force whatsoever. For example, in the $q = 0$ case, all the spins to the left of spins C, in Fig. 16a, can rotate around an axis defined by spins C with no restoring force. An example for the $\sqrt{3} \times \sqrt{3}$ case can be visualized again from Fig. 16b by continuously rotating the A and B spins around the C spins while keeping the angle between each pair constant at 120° throughout this rotation (see also sub-section 3.5.2). However, in the $q = 0$ state there are less such modes than in the $\sqrt{3} \times \sqrt{3}$ state, therefore making the $\sqrt{3} \times \sqrt{3}$ state the most likely to be selected at low temperatures (according to the order from disorder argument). Indeed, in the numerical simulations performed by Reimers and Berlinsky, a tendency towards coplanarity was found starting at $T/J \sim 0.01$. In addition, the order parameter corresponding to the $\sqrt{3} \times \sqrt{3}$ state ($m_{\sqrt{3}}$) increased as $T \rightarrow 0$. [23] However, the tendency toward the $\sqrt{3} \times \sqrt{3}$ state decreased with increasing lattice size. Henley demonstrated (by taking nonlinear interactions between the normal modes into account) that the $\sqrt{3} \times \sqrt{3}$ order is thermally selected in the low-temperature regime. [24]

As mentioned earlier, another mechanism which might help to select a specific configuration is that of quantum fluctuations. These types of fluctuations emerge from the inability to specify S_x , S_y , and S_z simultaneously for quantum spins. Therefore, even when two neighboring spins are fully up, there is still a residual interaction between their x and y components. This situation is demonstrated in Fig. 18 where we see that, unlike the classical spins, the quantum spins in a Néel type state spend some of their time with their x (or y) components parallel. According to Chubukov, when it comes to the kagomé lattice, this residual interaction is minimized in one of the long range coplanar configurations. [25] Another approach to account for quantum fluctuations is the so-called large N expansion, where each spin is allowed to have $N > 3$ components. Sachdev has found evidence from the large N expansion that the kagomé system prefers to be in the $\sqrt{3} \times \sqrt{3}$ state. [26]

From our discussion up to this point, it seems that the kagomé lattice favors the $\sqrt{3} \times \sqrt{3}$ ground state. However, if we momentarily assume that this is indeed the case, we immediately find some processes which act to destroy this state. Two such processes are chiral domain wall formation and quantum tunneling.

The chiral domain walls separate regions where the spins are arranged in a different sense of rotation, *i.e.* ABCABC vs. ACBACB (see the solid line in Fig. 19). The generation of chiral domain walls costs no energy but does increase the entropy. We therefore expect to find a large number of these walls. They should also be able to move easily across the lattice. This means that from an entropical point of view, long range or-

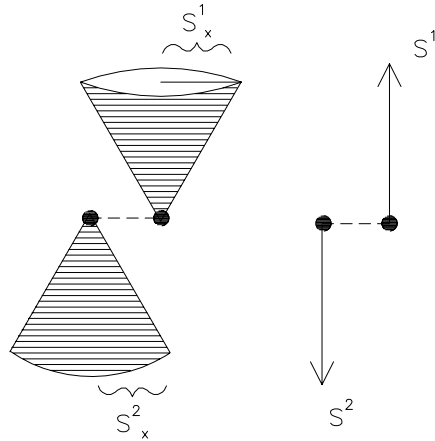


Figure 18: *Classical and quantum spins with antiferromagnetic interaction in a Néel state. In the quantum case some residual interaction exists from the x and y components.*

der is hopeless. But that is not the end of the story. In the presence of a domain wall, the restoring force reappears and the density of excited states in the presence of a wall is smaller than when the wall is absent. Thus, there must be a gentle competition between the tendency to order (from the disorder) and the tendency to increase the entropy by generating walls. [23]

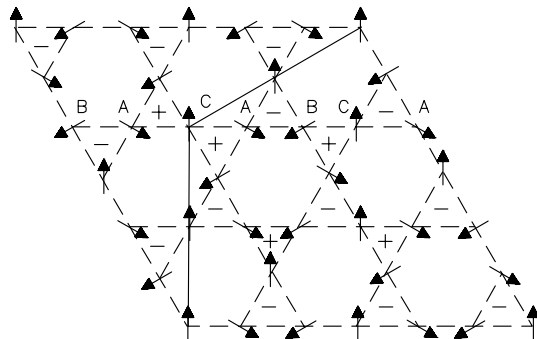


Figure 19: *Chiral domain wall in a coplanar the kagomé system*

The other force which is detrimental to the $\sqrt{3} \times \sqrt{3}$ state, and which was discussed by von Delft and Henley, is tunneling of spins from the A direction to the B direction, and vice versa, in a small region (say along the hexagon in Fig. 16b). [27] This tunneling can take two routes, from above the plane and from below it. In the case of integer spins, the two paths interfere constructively, and tunneling competes with the quantum tendency towards long range order. In the case of half integer spin the interference is destructive.

It is therefore difficult to answer our first question

and to determine whether the kagomé system orders at low temperatures or stays dynamic. The competition between mechanisms that favor the $\sqrt{3} \times \sqrt{3}$ state (or any other coplanar state) and those that drive the system towards disorder could result in a very interesting dynamical nature.

This leads us to the second question concerning the kagomé lattice, which is what type of excitation dominates the dynamics in this system. *A priori*, the dynamics could involve three different types of excitations:

(I) The usual magnon-like excitations (which are present in all ordered magnets).[20]

(II) The motion of chiral domain walls. We expect the rate at which domain walls move to be related to their length. In the kagomé lattice this length can involve as few as 6 spins with no upper limit to the number. On the other hand, walls of all lengths can move with no cost in energy, and we expect motion on all length scales to be present even at very low temperatures. Thus, the dynamical effects which result from this motion involve a wide range of time scales.

(III) The local modes. In the kagomé system, the high degeneracy leads to the motion of small groups of spins, as previously described. These excitations could affect the properties of the kagomé magnet at both the low temperature and the critical regions. In the critical region, the dynamical properties are usually determined by a frequency-wavelength relation and the rate at which the length scale diverges as $T \rightarrow T_c$. The local modes, however, are completely impartial to length scales, and should contribute to the dynamical properties even near T_c . In the low temperature region, the dynamical effects are usually determined by the fact that the amplitude of excitations decreases as the energy of the excitation decreases. This is not the case for the local modes, and their amplitudes are nearly independent of the excitation energy.

Again, it is hard to give a definite answer to the second question since it is not clear which type of excitation is the dominant one. What *is* clear is that these characteristics of the system must lead to anomalous dynamical behavior.

Experiments were done on two families of systems which have localized moments on kagomé lattice. These are the $\text{SrCr}_{8-x}\text{Ga}_{4+x}\text{O}_{19}$ (SCGO) and the Jarosites $\text{KR}_3(\text{OH})_6(\text{SO}_4)_2$ where $\text{R}=\text{Fe}$ (FeJ) or Cr (CrJ). However, instead of shedding new light on the problem, the experiments are even more confusing. Some unusual results were found in:

(I) Low temperature DC-Susceptibility measurement in SCGO which was done in two different cycles.[28, 29] The first cycle is known as the zero field cooled (ZFC), in which the sample is first cooled down to low temperature in zero external field and only then is the field applied. The susceptibility $\chi_{\text{zfc}}(T)$ is then measured by warming the sample. The second cycle is

the field cooled (FC), in which the field is first applied at high temperature (in the paramagnetic state) and then $\chi_{\text{fc}}(T)$ is measured upon cooling. It was found that SCGO behaves like a spin glass (SG) in susceptibility measurements (see appendix D). A spin glass usually shows a sharp peak in $\chi_{\text{zfc}}(T)$; the temperature at which χ_{zfc} peaks is known as the glass temperature T_g . In addition T_g is a bifurcation point in the sense that at temperatures below T_g the values of χ_{zfc} and χ_{fc} are different. This difference occurs since, upon cooling, a spin glass system is trapped in some region of phase space (the ZFC-region) separated from the rest of the phase space by an entropy wall. Therefore, the application of the field generates a response which represents only states of the system in the ZFC-region of phase space. On the other hand, cooling the system in the field leads it to a completely different region in phase space (the FC-region) resulting in a magnetic response indicative of that region. In general, systems with such confinement in phase space are known as nonergodic systems.[30] However, up to the time of these experiments, spin glass behavior has been observed only in systems in which magnetic ions randomly occupy a small fraction of sites in an otherwise non magnetic sample. This kind of geometrical randomness cannot be associated with SCGO. Moreover, even if the system is trapped in some region of phase space, the moment (according to the Heisenberg model) is expected to be the same as in any other region, as previously mentioned. Thus, the origin of the SG behavior is not understood.

(II) High temperature DC-susceptibility measurements in SCGO yielded the Curie-Weiss temperature of ~ 500 K.[31, 28, 29] This value is rather surprising since normally the Curie-Weiss temperature and the glass temperature are on the same scale, and for SCGO $T_g \sim 4$ K.[32]

(III) AC-susceptibility measurement of the non-linear part of $\chi(\omega)$, performed by Martínez *et al.* in SCGO, implied that the magnetic state below T_g does not correspond to a conventional spin glass.

(IV) Heat capacity measurement performed by Ramirez *et al.*[33] in SCGO showed that $C(T) \sim T^\alpha$ where $\alpha = 2$. In the CrJ, $C(T)$ is also consistent with the T^2 behavior at $T \rightarrow 0$. [34] This temperature dependence is in contrast to normal SG where $C(T) \sim T$, but in agreement with antiferromagnetic type excitations ($\omega \sim k$) in two dimensions. Assuming AFM type of excitation, it was concluded that the size of the area over which these excitations are well defined is $600 \times 600 \text{ \AA}^2$. Upon dilution of the magnetic Cr ions, α did not change appreciably, even when the percolation threshold for the kagomé lattice was crossed. This shows that the excitations which give rise to the T^2 behavior of the specific heat are of local nature and do not result from a collective phenomena.

(V) The neutron scattering experiment of Broholm

et al.[35] in SCGO found that at $T = 1.5$ K ($\sim 0.5T_g$), the ordered moment is only 25% of the total moment, while the rest of the moment fluctuates. A careful fit of the scattering peak to 2D and 3D models indicated that in this system the interactions are mainly of 2D nature, and that the correlation length ξ is only 7 ± 2 Å. This correlation length is in contrast to the size of the presumably AFM correlated region inferred from the heat capacity experiment, and suggests a somewhat disordered ground state. On the other hand, the response function $S(Q_0, \omega) \approx \int S(\mathbf{q}, \omega) d^3q$ showed no frequency dependence below T_g . This is the expected behavior from a 2D AFM (see section 2.3) with long range order. It should be pointed out that from this neutron scattering experiment we know only that the AFM correlations persist on a time scale of THz, and the ordered portion of the moment could, in principal, fluctuate on a longer time scale.

The picture emerging from all these experiments cannot be accommodated with traditional theories of spin glasses or antiferromagnets. The peculiarity of these systems is further emphasized in the experiments presented here. In the following sections, we will mostly study the dynamical nature of the kagomé magnet, utilizing both experimental and theoretical means. The experimental side concentrates on additional susceptibility and μ SR measurements of the two families of samples with kagomé structure. The theoretical part is devoted to dynamical numerical simulations and to the development of a dynamical model.

The structure of the chapter is as follows: In sections 3.2 and 3.3 we present the measurements on SCGO and Jarosites respectively. In section 3.4 we present a new type of numerical simulation, designed to evaluate the dynamical properties of Heisenberg spins on the kagomé lattice. Finally, in section 3.5 we draw some conclusions concerning this system. Using the insight obtained from the experiments and simulation, we suggest a model which could account for some of our observations.

3.2 $\text{SrCr}_{8-x}\text{Ga}_{4+x}\text{O}_{19}$

The physics of localized spins on kagomé lattice was considered by Japanese physicists from the early 50's. It became a popular subject in the western world only after the discovery, in 1984, by Obradors *et al.* of the compound $\text{SrCr}_{8-x}\text{Ga}_{4+x}\text{O}_{19}$ (SCGO) which has layers of Cr^{+3} ions arranged in the kagomé structure.[31] The cell of SCGO, shown in Fig. 20, is constructed of five layers, two of them (the 12KI and 12KII) are kagomé nets and the other three (the 2A, 4FI and 4FII) are layers of Cr^{+3} ions arranged in a triangular array. In the lattice these layers are arranged in the sequence 4FI-12KI-2A-12KII-4FII-4FII which isolate the two kagomé layers. The distance between the Cr ions on the triangular layers is larger than in the kagomé layers and we

believe that the magnetic behavior of this compound is determined by the physics of the kagomé lattice.

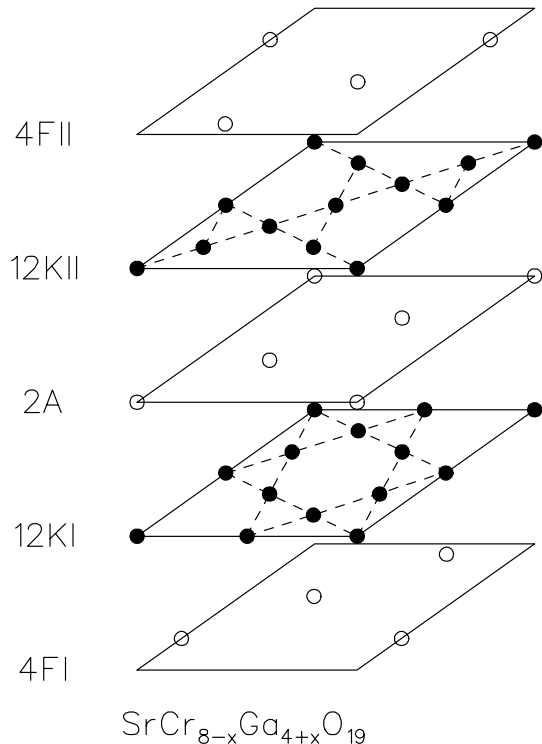


Figure 20: *The crystal structure of $\text{SrCr}_8\text{Ga}_4\text{O}_{19}$. The solid circles represent the kagomé layers (12KI and 12KII) and the empty circles represent the more dilute triangular layers (4FI, 4FII, and 2A).*

In this compound, the nonmagnetic Ga ions reside mostly on the triangular planes, but some Ga ions occupy sites on the kagomé plane. Unfortunately the SCGO is apparently not stable without the Ga and samples of pure kagomé planes ($x = -1$) have not been made. However, for $x < 2.126$, the concentration of Cr moments on the kagomé plane in SCGO is higher than the percolation threshold for that lattice ($p_c = 0.6527$), and we expect an infinitely large patch of interacting ions to exist in these samples. The superexchange interaction in SCGO is mediated via the oxygen ions.

In this section we present LF- μ SR, TF- μ SR, and susceptibility measurements of SCGO. The section is divided as follows: in sub-section 3.2.1 we present a new type of susceptibility experiment designed to study the field dependence of the bifurcation between field cooled and zero field cooled measurements. In sub-section 3.2.2 we present μ SR data on the two SCGO samples, one with $x = 0$ and the other with $x = 1.5$. The $x = 0$ and $x = 1.5$ has a site occupation $p = 0.88$ and $p = 0.72$ respectively. We find that it is difficult to reconcile our data with known relaxation theories of μ SR. This difficulty is discussed in sub-section 3.2.3.

3.2.1 Susceptibility Measurements

In our susceptibility experiment we test how the difference between the FC and the ZFC measurements depends on the applied field H . The motivation is that there should be no difference between FC and ZFC measurement in the Heisenberg model of spins on the kagomé lattice, unless there is some single ion anisotropy (a $D(S_z)^2$ term in the Hamiltonian).[19] This is because different classical minimum energy states in the Heisenberg model with external field, have the same moment; even if the system is trapped in some state in phase space, separated by an entropy wall from the rest of phase space, no effect should be observed in the susceptibility measurement. On the other hand if a single ion anisotropy does exist and the spin glass behavior is a result of this anisotropy, then the difference between the FC and ZFC experiments should disappear when $\mu_B H$ exceeds the anisotropy energy.[19]

We test this expectation by performing FC and ZFC experiments in various fields using a commercial (Quantum Design) SQUID dc-magnetometer at Columbia University. The results are presented in Fig. 21. We see that the difference at the lowest temperature (2 K) between the χ_{fc} and χ_{zfc} ($\Delta\chi$) decreases as the field increases, and disappears almost completely for $H = 2$ kG. We therefore conclude that any anisotropy energy should be on a scale of 0.1 K. In addition, we see that the bifurcation temperature T_b , where a difference between χ_{fc} and χ_{zfc} is observed, also decreases with increasing field.

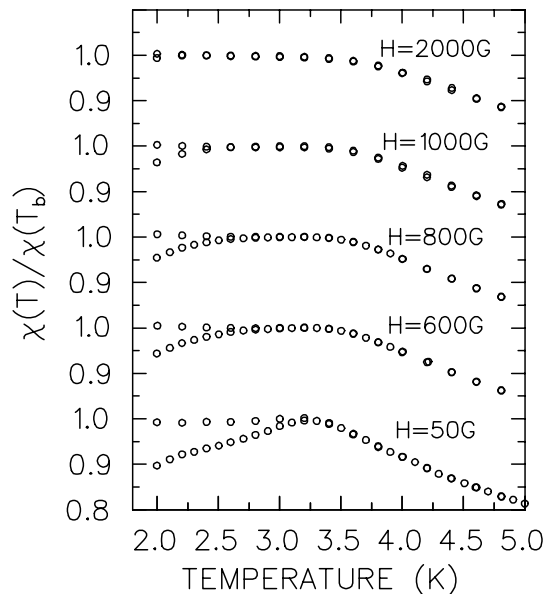


Figure 21: Field cooled and Zero field cooled susceptibility measurements in $SrCr_8Ga_4O_{19}$ at different applied magnetic fields.

We would like to present $\Delta\chi(0)/\chi(T_g)$ as a function of the field, but of course this quantity is not measurable. Instead we present

$$\Delta\chi(0)/\chi(T_g) \simeq [\Delta\chi(2) \cdot T_b]/[\chi(T_g) \cdot (T_b - 2)]$$

in Fig. 22 as a function of the applied field. Since there is no theory to guide us in presenting this measurement, we also show the same quantity but with T_b interchanged with T_g . In the inset we show the field dependence of the bifurcation temperature. At this point we don't know whether these quantities behave any differently than they would in a canonical spin glass since these kind of measurements were not performed before in SG systems. Such experiments are currently in preparation in our group.

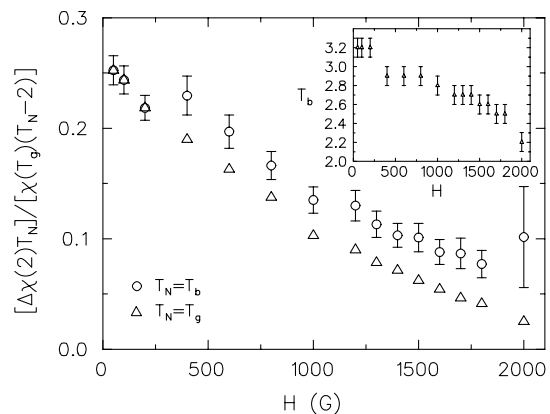


Figure 22: The difference between the susceptibility in the field and zero-field cooled measurements at 2 K ($\Delta\chi(2)$) normalized by two different normalization factors is plotted as a function of the applied magnetic field. The normalization factors are $T_N/[\chi(T_g) \cdot (T_N - 2)]$ where T_N is either T_g , the temperature of bifurcation at the lowest field (50 G), or T_b , the temperature of bifurcation at the applied field. In the inset we show the bifurcation temperature as a function of the applied field.

3.2.2 μ SR Measurements

The μ SR experiment was performed on two sintered SCGO samples, one with $x = 0$ and the other with $x = 1.5$. For this experiment we used both a dilution refrigerator and a normal cryostat.

In Fig. 23 we show the μ SR measurement in the longitudinal field configuration using a LF of 100 G. Since the relaxation rate increases by more than two orders of magnitude as the temperature is lowered, we present the data for temperatures below 5 K in Fig. 23a using a shorter timescale and for temperatures above 5 K, in Fig. 23b, using a longer timescale. The most

obvious feature of the data is that the rate at which the muon loses its polarization continuously increases as the temperature is lowered, even past T_g . This feature of the relaxation is very unusual (see 2.5), and in all other types of magnets known to us the relaxation rate increases as $T \rightarrow T_g^+$, peaks near the transition temperature, and then decreases as $T \rightarrow 0$.

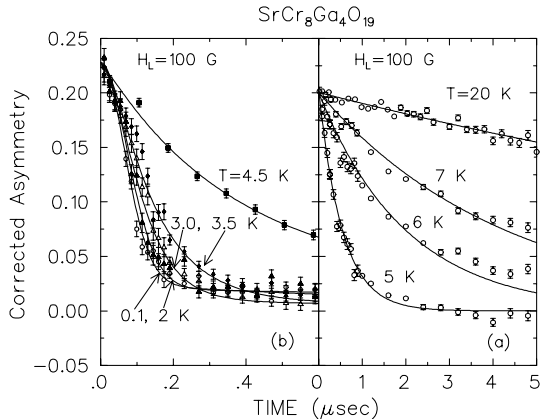


Figure 23: The corrected asymmetry in a longitudinal field of 100 G in $\text{SrCr}_8\text{Ga}_4\text{O}_{19}$ at (a) high temperatures ($T \geq 5$ K) and (b) low temperatures ($T < 5$ K). The solid lines are fits to Eq. 57 and 58 as described in the text.

When coming to fitting the muon asymmetry to a specific relaxation function we observe three elements in the data:

I) The asymmetry, at very low temperature (0.1 K), has a gaussian line shape at early times, and a slowly relaxes at long times. This is demonstrated in Fig. 24a and on a logarithmic scale in Fig 24b. The asymmetry involved in the long time relaxation rate is rather small and could, in principal, be a consequence of some unknown and complicated relaxation function. However, it could also be ascribed to background or defects in the sample. For practical reasons we assume the latter.

II) At temperatures close to T_g the asymmetry has an exponential line shape, again with two timescales involved. This is seen for $T = 4.5$ K in Figs 24c and d.

III) At high temperature ($T \geq 5.5$ K) the asymmetry is well described by an exponential line shape with a single timescale for relaxation. The asymmetry at $T = 5.5$ K is depicted in Figs. 24e and f.

We therefore fit the data at $T \leq 5$ K with

$$A(t) = A_b \exp(-\lambda t) + A_s \exp(-\Gamma(t)t) \quad (57)$$

where A_s/A_b is the asymmetry of the sample/background, λ is the background relaxation rate and $\Gamma(t)t$ is given by Eq. 28 (with $\omega_s = \omega_L = \gamma_m H_L$). This function yields all the features described above in items I and

II. It will also continuously connect to the function

$$A(t) = A_t \exp(-\Gamma t) \quad (58)$$

with $A_t \simeq A_b + A_s$, which is sufficient to describe the data at $T \geq 5$ K. We label the parameters Δ and ν obtained from fitting the data to Eqs. 57 and 58 with the index “fit” since we are planning to estimate them by other methods as well. The subscript 0 and 1.5 refers to the different samples. The connection between the two equations is made via the relation $\Gamma = 2(\Delta_0^{\text{fit}})^2/\nu^{\text{fit}}$. This parameterization of the relaxation rate Γ is valid when $\nu^{\text{fit}} \gg \omega_L$ as is the case for temperatures above 5 K. The parameter $\Delta_0^{\text{fit}} = 10 \pm 1 \mu\text{sec}^{-1}$ is global to both high and low temperatures. This value of Δ_0^{fit} corresponds to $\langle \mathbf{B}^2 \rangle^{1/2} \sim 100$ G. The fits are represented in Fig. 24 by the solid lines. Surprisingly, we find that Eq. 57 fits the data very well even for $\nu^{\text{fit}} < \Delta_0^{\text{fit}}$. We therefore take Eq. 57 as a phenomenological function which can be rigorously derived in the region $\nu^{\text{fit}} > \Delta_0^{\text{fit}}$ as shown in section 2.1.

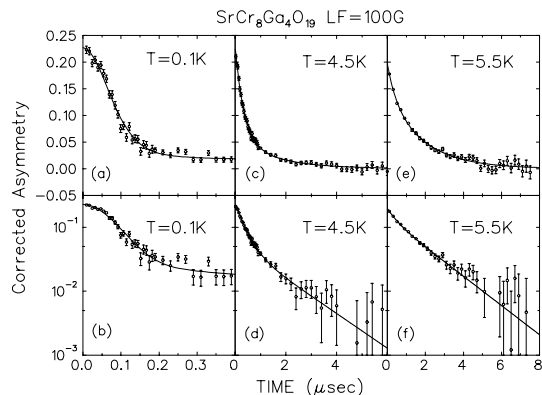


Figure 24: The line shape of the muon polarization in $\text{SrCr}_8\text{Ga}_4\text{O}_{19}$ at three different temperatures demonstrated on both linear and logarithmic scales. The solid lines are fits to Eq. 57 and 58 as described in the text.

The correlation time $\tau^{\text{fit}} = 1/\nu^{\text{fit}}$ obtained from the fits is presented in Fig. 25 as a function of temperature. The crossed and open squares represent fits to Eqs. 57 and 58 respectively. We also present a scale which is $2(\Delta_0^{\text{fit}})^2$ times the scale of τ^{fit} . We can read on this scale the spin-lattice relaxation rate $1/T_1$ which is well defined (and equals Γ) for temperatures above 5 K. In the inset we show τ^{fit} in a wider temperature range and on a logarithmic scale. We see that as we cool down τ^{fit} continuously increases over a very wide temperature range $T_g < T < 30T_g$, and at 1 K τ^{fit} saturates. These two phenomena are in contrast to usual spin glasses. For comparison, in the canonical spin glass CuMn , no relaxation is observed when $T > 3T_g$,

and the relaxation rate drops sharply below T_g . [36] In CuMn (5 at.%) the relaxation rate reaches $\sim 1\%$ of its maximum value when the temperature is decreased to $\sim 25\%$ of T_g .

Figure 25: The correlation time $\tau = 1/\nu$ as a function of temperature in both SCGO samples. The crossed/empty squares are obtained from a fit to Eq. 57/58 in the $x = 0$ sample. The same holds for the diamonds and the $x = 1.5$ samples. In the inset we show the same plot on a wider temperature range. The additional vertical axes are explained in the text.

An important test of our understanding of the relaxation mechanism is a decoupling experiment in which we measure the relaxation rates in various external longitudinal fields. Normally we would expect a polarization with a gaussian shape and $\Delta \sim 10 \mu\text{sec}^{-1}$ to decouple completely with a field of 500 G. However, again to our surprise, we find that this is not the case in SCGO. In Fig. 26a we show the raw asymmetry for various longitudinal fields at $T = 100 \text{ mK}$. It is clear that the polarization in SCGO does not decouple as expected. In fact there is hardly any change in the relaxation rate up 0.2 T. Since the application of a large field strongly influences the α parameter (see 1.1.7), as can be seen most clearly in the case of 2 T, we correct α so that the asymmetry at $t = 0$ is the same for all the spectra. The corrected asymmetry is presented in Fig. 26b. In this figure we also see the expected polarization using Eq. 57 with the parameters obtained from the 0.1 K, 100 G data and an external field of 500 G. There is an obvious discrepancy between the expected decoupling rate and the observed one. It also should be pointed out that the discrepancy between theory and experiment is independent of which theory (AR, DKT, or MC) we use (see section 2.1). Thus we conclude that Δ_0^{fit} and τ^{fit} do not represent the true RMS and correlation time of the local field and that they should be

regarded only as phenomenological fitting parameters.

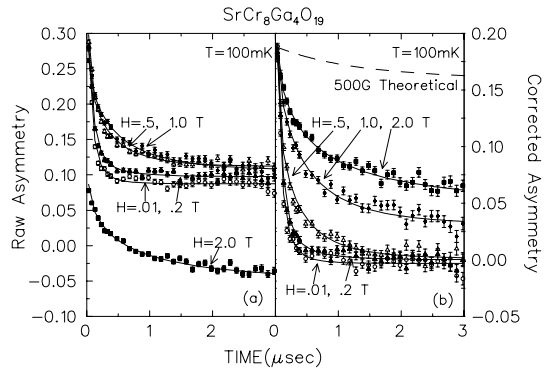


Figure 26: The (a) raw and (b) corrected asymmetry in a LF- μSR measurement in $\text{SrCr}_8\text{Ga}_4\text{O}_{19}$ at 100 mK and various longitudinal fields. The solid lines are guides to the eye. The broken line in (b) is the expected polarization in a longitudinal field of 500 G according to the parameter obtained from the 0.1 K, 100 G data as explained in the text.

Puzzled by the decoupling mystery, we attempt to test more directly the internal field at the muon site. This test is performed in two steps: (I) TF- μSR and (II) susceptibility measurements.

(I) In the TF- μSR experiment we measured the muon rotation frequency as a function of temperature $f(T)$ by applying a strong field (2 kG) perpendicular to the initial muon polarization. The oscillating asymmetry for $T = 100 \text{ K}$ and $T = 20 \text{ K}$ is shown in Figs. 27a and b in the so called rotating reference frame. In this frame we multiply the signal by $\cos(2\pi f_{\text{RRF}} t)$ and average all the events within a time period n/f_{RRF} (n is an integer). In this way we see only the beat frequency, which is the difference between the precession frequency and f_{RRF} . Looking at this figure, it is hard to see any shift in frequency between the two temperatures. We therefore conclude that the frequency shift is smaller than our resolution, namely, $f(100) - f(20) < 0.1 \mu\text{sec}^{-1}$.

(II) In the susceptibility experiment we measure the sample magnetization as a function of temperature $M(T)$ also in $H = 2 \text{ kG}$. In Fig. 27c we present the susceptibility $\chi(T) = M(T)/H$.

If we now assume that the internal field is a linear combination of the applied field and the magnetization we have

$$\Delta B(T) = (2\pi/\gamma_m)\Delta f(T) = g\Delta\mu_{eff}^z(T) \quad (59)$$

where $\mu_{eff}^z = M/N$ is the induced moment per Cr, we find that $g < 3 \text{ kG}/\mu_B$. With this upper limit on g we can estimate the upper limit on the field at the muon site by replacing $\Delta\mu_{eff}^z$ with the Cr effective moment $\mu_{eff} = 4.07 \mu_B$ in Eq. 59. [28] This method predicts

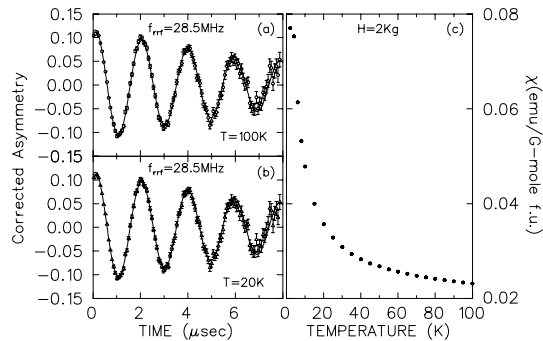


Figure 27: Muon precession in the TF- μ SR configuration at an applied field of 2 kG, presented in the rotating reference frame at (a) $T = 100$ K and (b) $T = 20$ K, for $\text{SrCr}_8\text{Ga}_4\text{O}_{19}$. The uniform susceptibility as a function of temperature is depicted in (c).

that the local field at the muon site is smaller than 12 kG.

In order to find a lower limit on the field we use numerical simulations. In these simulations, the orientation of the Cr moments was allowed to vary randomly in a finite size numerical sample. The local field at a position \mathbf{r} in this sample was calculated by summing the dipolar fields from all moments in a sphere of radius 10 Å. We found $\langle B^2 \rangle^{1/2} > 3$ kG at all sites. Using a larger sphere could only increase the minimum value of $\langle B^2 \rangle^{1/2}$.

A third method for field estimation is to use the relation $1/T_1 = 2\Delta^2\tau$ (see 2.1) which should hold at high temperatures and small LF. The correlation time τ is estimated from the energy-time version of the Heisenberg principle as $\tau \simeq \hbar/J\sqrt{Z_{\text{eff}}}$ where Z_{eff} is the average number of nearest neighbors. In order to evaluate this number we use the relation

$$Z_{\text{eff}} = \sum_{i=1}^4 iC_i^4 p^i (1-p)^{4-i}$$

where C_i^4 is the number of ways an ion can have i chromium neighbors and p is the site occupation. For the $x = 0$ sample ($p = 0.88$) $Z_{\text{eff}} = 3.38$. Taking the relaxation rate at 50 K, $1/T_1 = 0.026 \mu\text{sec}^{-1}$, and $J = 60$ K [20] we find $\Delta/\gamma_m = 6.2$ kG. This method, combined with the other two, shows that the order of magnitude of the internal field is 10 kG. The huge difference between the estimated value of the parameter Δ , ($\Delta^{\text{est}} \sim 10^3 \mu\text{sec}^{-1}$) and the value we obtain from our fits in the LF- μ SR experiment ($\Delta_0^{\text{fit}} = 10 \mu\text{sec}^{-1}$) reinforces our conclusion that Δ_0^{fit} and τ^{fit} do not truly represent the RMS and correlation time of the internal field.

We now turn to look at the $x = 1.5$ sample. Since the temperature and field dependence of the muon po-

larization in this case is very similar to the one we observed in the $x = 0$ sample we present the data somewhat briefly. In Fig. 28a we show the corrected asymmetry for several temperatures and a longitudinal field of 100 G. Here again we see that the rate at which the muon loses its polarization increases continuously down to 2 K and then saturates. In Fig. 28b we show the corrected asymmetry for several longitudinal fields. We fit the $H_L = 100$ G data in exactly the same way as in the $x = 0$ case, but this time the global parameter $\Delta_{1.5}^{\text{fit}} = 5.8 \pm 0.2 \mu\text{sec}^{-1}$. We present the correlation time and spin-lattice relaxation rate as described in the previous section in Fig. 25. The crossed and empty diamonds represent fits to Eq. 57 and Eq. 58 respectively. We also present a scale which is $2(\Delta_{1.5}^{\text{fit}})^2$ times the scale of τ^{fit} as in the $x = 1.5$ case.

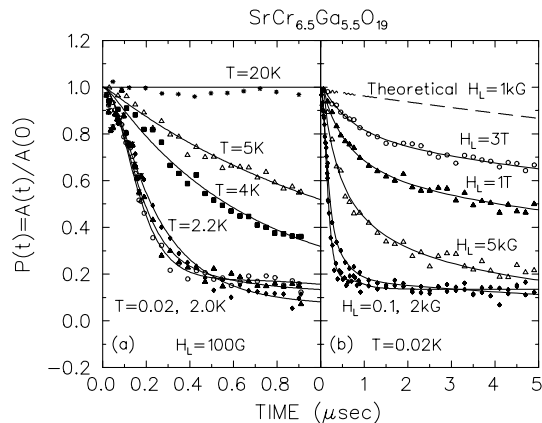


Figure 28: The muon polarization in the $x = 1.5$ sample at (a) longitudinal field of 100 G and various temperatures and (b) temperature of 0.02 K and various longitudinal fields. In (b) the solid lines are guides to the eye; the broken line is the expected polarization in a longitudinal field of 1 kG according to the parameter obtained from the 0.02 K, 100 G data as explained in the text.

The most striking feature of the comparison between the correlation time τ^{fit} in the two samples is that it is nearly the same for all temperatures below 7 K. This is surprising since the $x = 1.5$ sample is diluted; therefore, the correlation length and, thus, the correlation time, must be smaller. In other words, smaller groups of spins are locked together and the magnetic behavior of the $x = 1.5$ sample should more resemble a paramagnet.

Using the Δ^{fit} and τ^{fit} obtained from the $T = 0.02$ K, $H_L = 100$ G data, we plot the expected theoretical curve at a field of 1 kG using Eq. 57. Again, we find that the decoupling rate does not agree with our expectation. We can estimate the internal field in this sample using the 50 K value of $1/T_1 = 0.036 \mu\text{sec}^{-1}$ and

$Z_{\text{eff}} = 2.56$ ($p=0.72$) which gives $\Delta_{1.5}^{\text{est}}/\gamma_m = 6.9$ kG. Again the estimate of the local field from our dynamical theory of chapter 2 and simple energy scale considerations disagree. It also seems that $\Delta_0^{\text{est}} < \Delta_{1.5}^{\text{est}}$. This is not expected in a paramagnetic state, unless at 50 K the spins are still correlated, and for some reason dilution increases the local field.

3.2.3 Discussion

We have found several unexpected features in our μSR experiments in SCGO. These features will be reviewed in the concluding chapter (3.5). At the moment, the open question is whether these effects are indeed properties of the kagomé lattice or are a mere coincidence which occurs in the SCGO compounds. In order to test the second possibility we present in the next section a similar experiment on another group of systems, known as the jarosites, which also have a kagomé lattice structure. In section 3.4 we demonstrate, using numerical simulations, that indeed some of the unusual properties found here are inherent in the kagomé lattice.

3.3 The Jarosite Systems

Most of the experimental effort in kagomé systems to date has concentrated on SCGO.[35, 29, 33, 37, 5, 38] However, SCGO possesses magnetic impurities on the kagomé plane (for all values of x at which it is stable) and so does not serve as a perfect realization of the AFM kagomé lattice.[31] Therefore, we decided to broaden the μSR investigation to the family of compounds known as the jarosites, especially $\text{KFe}_3(\text{OH})_6(\text{SO}_4)_2$ (FeJ), and $\text{KCr}_3(\text{OH})_6(\text{SO}_4)_2$ (CrJ). The jarosites have no magnetic impurities on the kagomé plane and the ionic moments (Fe^{+3} , $S=5/2$ and Cr^{+3} , $S=3/2$) can be easily interchanged, thus making this system almost ideal for the experimental study of the kagomé lattice.[39, 40] The Jarosites may still fall short of the idealized 2D kagomé system because of the interplane interactions found in all real systems.[41, 42, 43, 35] These interactions, as small as they might be, could change the nature of the problem in question.

Some information on the dimensionality of the magnetic interaction is provided by previously performed experiments.[40, 41, 42] Susceptibility and Mössbauer measurements show that FeJ orders magnetically with $T_N > 50$ K and that the Curie-Weiss temperature (T_{CW}) is 600 K;[40, 41] therefore $T_N/T_{\text{CW}} = 0.08$. Neutron scattering in this sample found that the order extends in all 3 dimensions.[41] The CrJ, on the other hand, has a Curie-Weiss temperature of 67.5 K [41] and shows a phase transition, in neutron scattering, only at 1.9 K [43]; therefore $T_N/T_{\text{CW}} = 0.03$. The frozen portion of the moment, however, is only 4% of the total moment.[43] This fact, combined with detailed analysis of the inelastic neutron scattering peaks, sug-

gests that the interaction in the CrJ is closer to being two dimensional than the interaction in the FeJ compound. The ordering in both cases is of the $q = 0$ type.[40, 41, 43] It should also be pointed out that the neutron scattering in CrJ revealed the coexistence of a short range correlation component together with the long range order.[42, 43]

We therefore study in section 3.3.1 the FeJ as an example of an ordered kagomé system, possibly with 3D interactions, and concentrate on the magnetic properties in the ordered state. We investigate the CrJ in section 3.3.2 as an example of a quasi 2D kagomé system and concentrate on the dynamical properties. For the CrJ we present susceptibility measurements in addition to the μSR experiments.

3.3.1 $\text{KFe}_3(\text{OH})_6(\text{SO}_4)_2$

The μSR experiment in FeJ was performed in the zero field (ZF) configuration using a gas-flow cryostat. In this configuration the muon spin is influenced only by the presence of the internal magnetic field. In Fig.29 we show the time dependence of the polarization in FeJ at three different temperatures. At 100 K the electronic moments fluctuate very rapidly and are not effective in depolarizing the muon spin, but as the temperature is lowered these fluctuations slow down. At 55 K we already see a strongly damped oscillatory signal which indicates the onset of magnetic order. At a much lower temperature (6 K), the damping decreases and full spin precession is observed. It is evident from the figure that the precession is governed by more than one frequency at low temperatures. Therefore, we fit the data below 45 K with

$$P_z(t) = A_b e^{-t/T_b} + A_f e^{-t/T_f} \cos(\omega_f t) + A_s e^{-t/T_s} \cos(\omega_s t). \quad (60)$$

Above 50 K we could not resolve the two frequencies and so used only one oscillating signal. The fact that two frequencies are observed indicates that there are either two crystallographically inequivalent muon sites or a unique site which does not possess the symmetries of the magnetic system.

In a linear interaction between the muon spin and the electronic spins (e. g. dipolar interaction), the local moment is proportional to the muon precession frequency. We present the fast frequency ω_f and slow frequency ω_s normalized by their value at the lowest temperature (2.1 K) in Fig.30. For comparison we also show the mean field theory curve for spin 5/2 assuming $T_N = 60$ K. From this figure we see that the measured moment is somewhat more stable against thermal excitation than the mean field prediction. This stability supports the identification of three dimensional ordering found by neutron scattering. As a justification for the use of two oscillating signals in our fit at low temperatures, we show in the inset of Fig.30 the Fourier

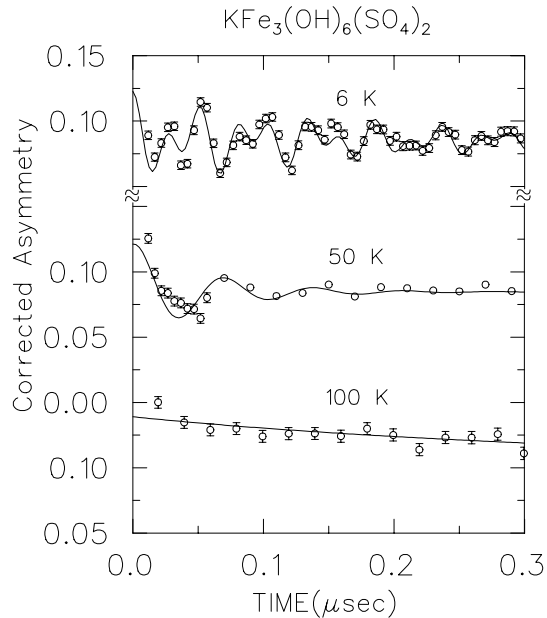


Figure 29: The corrected asymmetry in $KFe_3(OH)_6(SO_4)_2$ at three different temperatures.

transform of the data at $T = 2.1$ K. Two major frequencies are seen with a smaller contribution from a third frequency which cannot be resolved in the fits. The frequencies at $T = 2.1$ K correspond to a local field of 2.8 kG and 1.6 kG at the muon sites, respectively.

3.3.2 $KCr_3(OH)_6(SO_4)_2$

The susceptibility measurements on the CrJ were made using a Quantum Design (SQUID) magnetometer at the University of British Columbia. The results, shown in Fig.31, were obtained using a field of 100 G in the field cooling and a zero field cooling sequences. We found a clear difference between the FC and ZFC measurements below 2.5 K but no actual cusp in the susceptibility. The same difference was observed in SCGO, but there a cusp was also observed.[29] This suggests that the temperature hysteresis in susceptibility is inherent in the kagomé lattice and is not a result of magnetic impurities.

The μ SR experiment in CrJ was performed in the longitudinal field (LF) configuration using an Oxford dilution refrigerator. In order to obtain better cooling of the powder sample in the dilution refrigerator we mixed the powder with 10% apiezon grease which was diluted in Hexane and allowed to dry for a day. This procedure did not change the susceptibility (per Cr) of the sample.

The polarization function in CrJ at $H_L = 100$ G and several temperatures is shown in Fig.32. We used

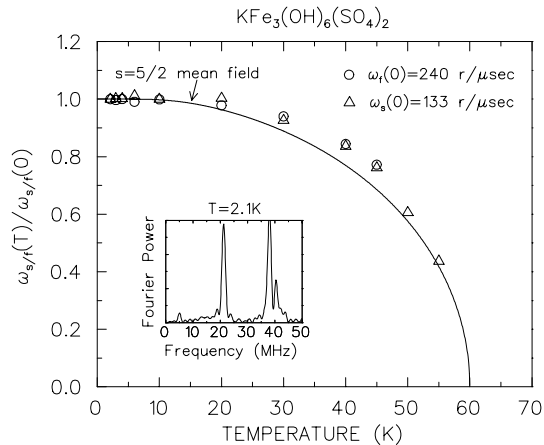


Figure 30: The temperature dependence of the slow and fast muon spin precession frequency $\omega_{s/f}(T)$, as given by Eq. 60, normalized by $\omega_{s/f}(0)$. The solid line represents the mean field prediction of spin 5/2. The inset shows the Fourier transform of the corrected asymmetry at 2.1 K.

a small longitudinal field of 100 G in order to obtain a clear baseline by decoupling the background and the field generated by nuclear dipole moments. The increase in relaxation as the system is cooled down from 10 K to 25 mK indicates the slowing down of spin fluctuations. The absence of the 1/3 recovery even at $T = 25$ mK indicates either fast or intermediate fluctuations. In order to distinguish between the two fluctuation regimes we plot the early time relaxation at $T = 25$ mK in the inset of the figure. The shape of the relaxation function suggests the existence of two sites, as in FeJ, with a gaussian shaped relaxation function at early time. In order to be impartial to the line shape we use the relaxation function

$$P_z(t) = A_f \exp[-(t/T_f)^\beta] + A_s \exp[-(t/T_s)^\beta]. \quad (61)$$

for data fitting. β is a free parameter limited to the region $0 \leq \beta \leq 2$. We allow fractional values for β in order to accommodate the possibility of dilution effects (see appendix D). We fit the data with the asymmetries of the fast relaxing signal A_f and slow relaxing signal A_s held fixed at all temperatures. At $T = 25$ mK we found $\beta_{s/f} = 2.0/1.67$; these values of β , combined with the lack of the 1/3 recovery, support the intermediate fluctuation scenario ($\nu \sim \Delta$) at this temperature (at least for the slow signal). The values of the relaxation rates at this temperature are $T_{s/f} = 1.08/0.11$ μ sec and the square root of their ratio has the same order of magnitude as the ratios of the local fields in the FeJ case. However, we cannot conclude that the muons occupy the same site in the two compounds, since the asymmetry ratio A_f/A_s in CrJ is different from this ratio in FeJ.

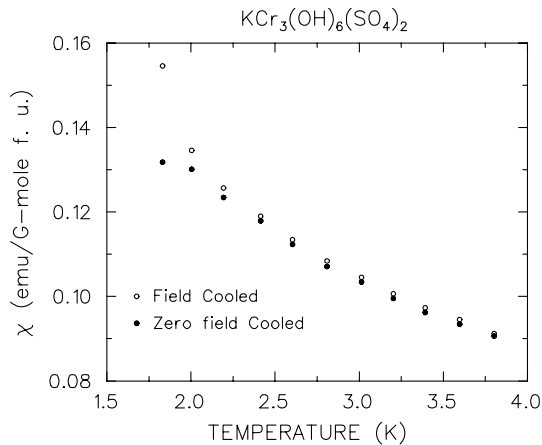


Figure 31: Field cooled and zero field cooled susceptibility measurement in $KCr_3(OH)_6(SO_4)_2$.

The amplitude of the fast relaxing signal (A_f) is small and the error bars in T_f and β_f are rather large. This is not the case for T_s or β_s . We therefore show only the parameters of the slow signal as a function of temperature in Fig.33. The change in β_s from ~ 1 at high temperatures to 2 as $T \rightarrow 0$ indicates a transition between the fast fluctuating limit to the intermediate limit. The transition takes place at $T \simeq 2$ K which corresponds to the phase transition observed in neutron scattering.[43] Below $T \sim 1$ K, the relaxation rate T_s saturates; the same saturation was observed in SCGO (see 3.2).[37, 5, 38] The saturation of T_s indicates that spin fluctuations remain with large spectral weight at low frequencies (~ 1 MHz) down to 25 mK.

In Fig.34 we show the field dependence of the polarization function at $T = 25$ mK for several longitudinal magnetic fields. The solid lines are guides for the eye. The expected increase in the terminal value of $P_z(t)$ with increasing LF is indeed observed. However, this increase occurs at a rate which is much slower than expected. For comparison, we also plot in this figure the expected theoretical curve (dashed line) for a longitudinal field of 500 G. For this curve we assume $\nu = \Delta$ and use the Kubo-Toyabe dynamical theory with these parameters evaluated from the 25 mK, 100 G data. A large disagreement is observed between the theory and experiment. A similar disagreement was observed in a LF μ SR experiment in SCGO.[38]

3.3.3 Discussion

We find that the lack of a peak in $1/T_1$, the unexpected decoupling rate, and the bifurcation in susceptibility measurement are common to both CrJ and SCGO. The FeJ behaves in a completely different manner. Whether there is indeed a stronger 3D interaction in FeJ or there is some critical spin value $3/2 < S_c \leq 5/2$ above which

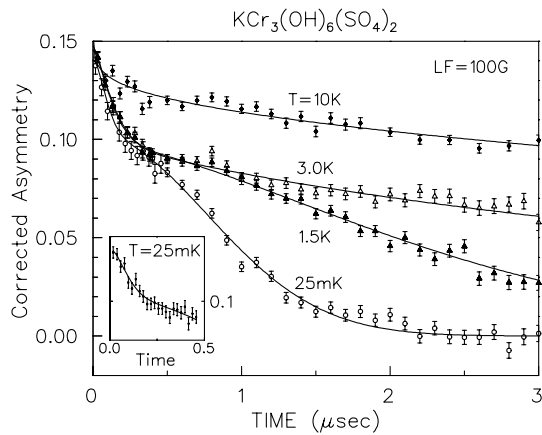


Figure 32: The corrected asymmetry in $KCr_3(OH)_6(SO_4)_2$ at a $H_L = 100$ G and several temperatures. The inset shows the early time depolarization in the $T = 25$ mK case.

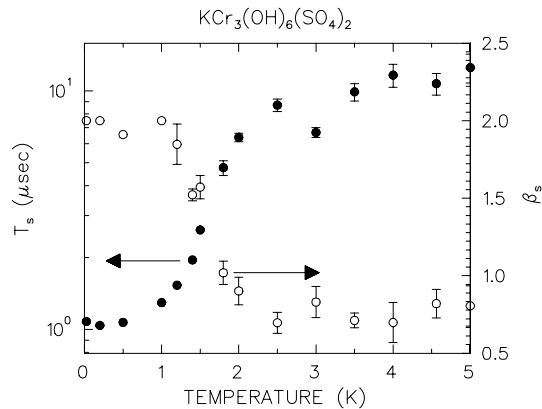


Figure 33: The temperature dependence of the parameters T_s and β_s as obtained from Eq. 61.

quantum fluctuations are suppressed and the kagomé lattice can order, is not clear to us. We now turn to the numerical simulation which will further enforce some of these conclusions.

3.4 Numerical Simulation

The dynamical properties of the kagomé system found by μ SR (see section 3.2 and 3.3), and our theoretical expectation for unusual dynamical behavior (discussed in section 3.1) motivated us to simulate the time evolution of spins on a kagomé lattice. Our aim is to check the stability of the possible long range ground state configurations against small excitations as well as to investigate the temperature dependence of the spin-lattice relaxation rate $1/T_1$. This relaxation rate is computed

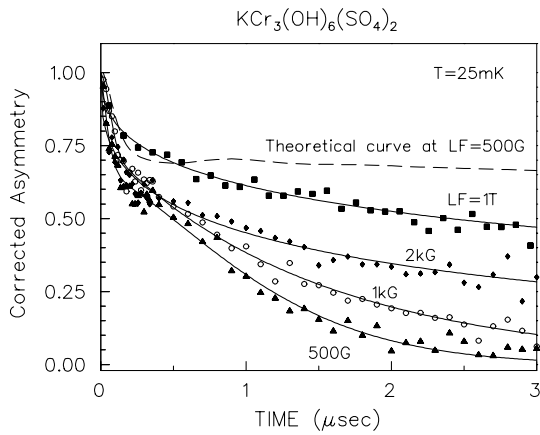


Figure 34: The corrected asymmetry in a LF- μ SR measurement on $KCr_3(OH)_6(SO_4)_2$ at 25 mK and various longitudinal fields. The solid lines are guides to the eye. The broken line is the expected polarization in a longitudinal field of 500 G according to the parameter obtained from the 25 mK, 100 G data as explained in the text.

via the spin-spin correlation function $\langle \hat{\mathbf{S}}(0) \cdot \hat{\mathbf{S}}(t) \rangle$. We also wish to examine the influence of the underlying lattice geometry on the spin evolution. This is achieved by comparing the dynamics of kagomé and square lattices (both are 4-fold coordinated). Since some of the experiments were done on diluted systems, we also test the influence of vacancies on the correlation time.

Our numerical study proceeds in three steps: (I) we examine the time evolution of an individual spin $\hat{\mathbf{S}}_i(t)$ for given initial conditions, (II) we test the stability of the system by comparing the sample averaged correlation function $[\hat{\mathbf{S}}(0) \cdot \hat{\mathbf{S}}(t)]$ (SACF) between the two lattices for a given excitation energy, and (III) we evaluate the spectral density (see Eq. 31) from the temperature averaged correlation function $\langle \hat{\mathbf{S}}(0) \cdot \hat{\mathbf{S}}(t) \rangle$ (TACF) and discuss its application to experiments.

We approximate the equation of motion for each spin with that derived from the classical Heisenberg Hamiltonian; namely,

$$\frac{d\hat{\mathbf{S}}_i}{dt} = -J\hat{\mathbf{S}}_i \times \sum_{j:i} \hat{\mathbf{S}}_j, \quad (62)$$

where $\hat{\mathbf{S}}_i$ is a three-component unit vector representing the spin direction. The sum in Eq. 62 is taken over the nearest neighbors of the i 'th spin (employing periodic boundary conditions). We numerically evaluate $\hat{\mathbf{S}}_i(t)$ using the 4'th order Runge-Kutta (RK) algorithm with a time increment (dt) of 0.02 or less.[44] In this algorithm the spin configuration at $t + dt$ is first crudely estimated from $S_i(t)$ using Eq. 62 with a finite dt . The

estimated value is then fed back into the equation of motion in order to obtain a more correct value. The term "4'th order" stands for four corrections in each time step (dt). The error thus obtained is of order $\mathcal{O}(dt)^5$. The lattice sizes in steps I and II are 972 spins ($L = 18$) for the kagomé and 900 spins ($L = 30$) for the square. In step III we present results for the kagomé lattice with smaller sizes as well.

In step (I) the simulation is performed for a particular choice of excitation in (a) the square lattice, (b) the $\sqrt{3} \times \sqrt{3}$ state on the kagomé lattice, and (c) the $q = 0$ state on the kagomé lattice. We first place the spins in a long range ordered ground state where the spins lie in the $\hat{\mathbf{x}}\hat{\mathbf{y}}$ plane. We then pivot one spin out of this plane ($S_z(0) = 1$). The excitation energy corresponding to this configuration is $4J$ on the square lattice and $2J$ on the kagomé lattice. The results are shown in Fig. 35. In each of the three cases, a, b, and c, we present the time evolution of S_z for two different spins on the lattice: $S_z(t)$ of a modified spin and $S_z(t)$ of an unmodified spin. The figures demonstrate a remarkable difference between the time evolution of the spins on the square lattice and the spins on the kagomé lattice. In the square case, the modified spin undergoes periodic motion around an average value which lies in the plane. The frequency ($8\pi J$) of this motion corresponds to the field at the site of the modified spin at $t = 0$. The motion of the modified spin is governed by a narrow distribution of frequencies and is only weakly damped within the plotted simulation time. In the kagomé case, on the other hand, none of the spins can be described as fluctuating around a finite average component at long times. There is also more than one characteristic time scale involved in the motion. Only at the beginning of the motion can a frequency ($4\pi J$) be defined for three periods. This frequency again corresponds to the local field at the site of the modified spin at $t = 0$.

In step (II) we obtain the sample-averaged correlation function (SACF) for a given excitation energy. The SACF is calculated by evaluating the scalar product of $\hat{\mathbf{S}}_i(0)$ and $\hat{\mathbf{S}}_i(t)$ for each individual spin and then averaging over the entire lattice. Here, unlike in step (I), we excite the system by slightly disorienting each spin on the lattice from its ground state direction. The new orientation is chosen randomly within a small solid angle (Ω) centered around the original spin direction. The energy of excitation (ΔE) is controlled by the choice of Ω . In Fig. 36 we show the SACF with this type of collective excitation ($\Delta E = 4J$). The difference between the square and the kagomé lattice is obvious, but there is also a substantial difference between the $\sqrt{3} \times \sqrt{3}$ and the $q = 0$. We discuss the three cases in the framework of a damped harmonic oscillator. The SACF of the square lattice, shown in Fig. 36a, exhibits a clearly defined frequency ($0.01J$) with a zero damping rate. On the other hand, the SACF in the excited

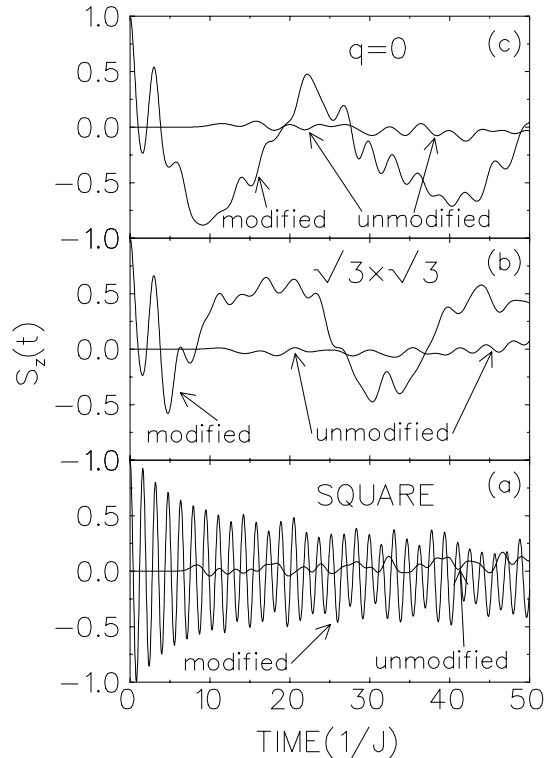


Figure 35: The time evolution of \hat{S}_z in three cases: (a) the excited square lattice; (b) the excited $\sqrt{3} \times \sqrt{3}$ state on the kagomé lattice; (c) the excited $q = 0$ state on the kagomé lattice. The excitation of the system is achieved by rotating one spin into a direction perpendicular to the plane of the ground state. In each case $\hat{S}_z(t)$ for both the modified spin and another, initially unmodified spin, is shown.

$\sqrt{3} \times \sqrt{3}$, shown in Fig. 36b, has a very large damping rate and oscillations occur on various time scales. Finally, the excited $q = 0$, shown in Fig. 36c, is an intermediate case in which the frequency, like that of the square lattice, is well defined ($0.007J$), but the damping is finite like that of the $\sqrt{3} \times \sqrt{3}$.

In step (III) we perform the temperature average following the procedure of Wysin and Bishop using a combination of Monte Carlo (MC) simulation and the RK integration.[45] The underlying equation which we evaluate is

$$\langle \hat{\mathbf{S}}(0) \cdot \hat{\mathbf{S}}(t) \rangle = \sum_{\text{IC}} \frac{e^{(-E/T)}}{Z} [\hat{\mathbf{S}}(0) \cdot \hat{\mathbf{S}}(t)]_{\text{IC}} \quad (63)$$

where IC stands for Initial Conditions, E is the total energy of the system with a given IC, T is the temperature, and Z is the partition function. The evaluation of Eq. 63 is done in a cyclic procedure: first the system is warmed from the $T = 0$ configuration by MC; next, the final configuration of the MC procedure is

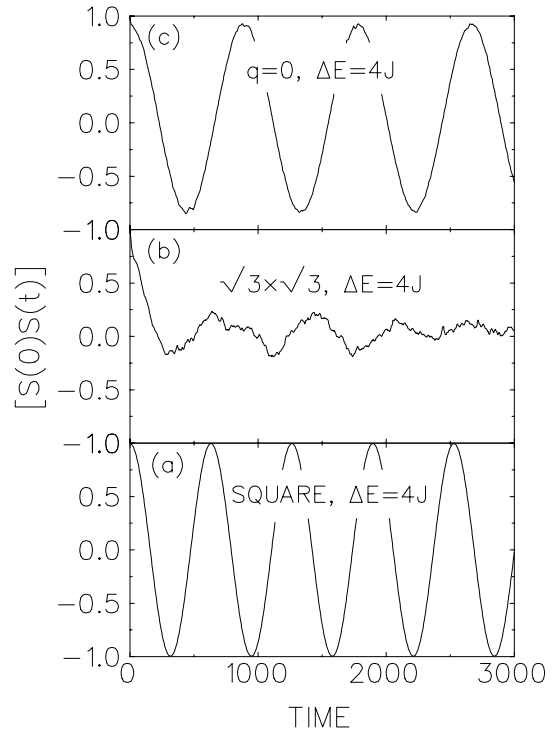


Figure 36: Sample averaged correlation functions for the collectively excited (a) square lattice, (b) $\sqrt{3} \times \sqrt{3}$ state on kagomé lattice, and (c) $q = 0$ state on kagomé lattice.

taken to be the initial configuration for the equations of motion; the RK integration is then used to obtain a correlation function, and the final configuration of the motion is fed back into the MC for a new choice of initial conditions. We average the correlation functions over 18 cycles at low temperatures and 6 cycles at high temperatures. For the Monte Carlo selection of states we use 10000 lattice sweeps in the standard Metropolis algorithm.[44] In this algorithm the present spin configuration of the system (with energy E_p) is changed to a new configuration by first randomly generating a temporary spin state (energy E_t). The temporary state is obtained by modifying only one spin in the present configuration. The temporary state is then accepted as the new system configuration with probability $\exp(-(E_t - E_p)/T)$. In the kagomé case, the $T = 0$ state is taken as the $\sqrt{3} \times \sqrt{3}$.

In Fig. 37 we show the TACF for the kagomé lattice at $T = 0.01 J$. We see that $\langle \hat{\mathbf{S}}(0) \cdot \hat{\mathbf{S}}(t) \rangle$ has a zero derivative at $t = 0$, as predicted by several authors, [46] and that it is overdamped. We also show in this figure the TACF for several values of non-magnetic impurity concentration (x). It is clear that the initial relaxation rate of the $\langle \hat{\mathbf{S}}(0) \cdot \hat{\mathbf{S}}(t) \rangle$ is nearly independent of the impurity concentration, even for values of x larger than

the percolation threshold ($1 - p_c = 0.3473$). [33] This result indicates that the dynamics of the kagomé lattice are mostly governed by local excitations and do not involve collective motion of spins on the lattice.

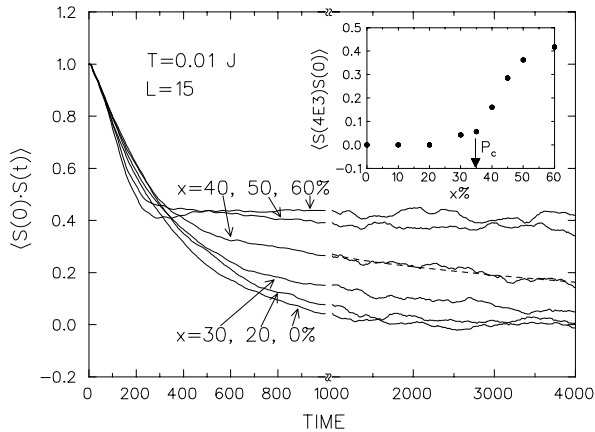


Figure 37: The spin-spin correlation function for various values of the non-magnetic impurity concentration x . The broken line demonstrates a fit to an exponential at late times with which we obtain the terminal value of this function. The inset shows the terminal value as a function of x .

We also see that the terminal value of the temperature averaged correlation function ($\langle \hat{S}(4000) \cdot \hat{S}(0) \rangle$) increases as x increases. This behavior is expected since as x increases, more and more spins become isolated and stay correlated at all times. In the inset of the figure we show the terminal value of the TACF as a function of x . This value is determined by fitting the $\langle \hat{S}(0) \cdot \hat{S}(t) \rangle$ at late time to an exponentially relaxing function, as demonstrated by the broken line for the $x = 40\%$ case. At an impurity concentration smaller than the percolation threshold, the terminal value of the TACF is consistent with zero, but as we cross the threshold this value goes up dramatically.

At the end of the temperature averaging we obtain the spectral density $\tilde{\Phi}(\omega)$. Since we don't know the muon site (or the matrix \mathbf{A} used in Eq. 35) we define

$$\tilde{\Phi}'(\omega) = 2 \int_0^{\infty} dt \cos(\omega t) \langle \hat{S}(0) \cdot \hat{S}(t) \rangle, \quad (64)$$

and evaluate this Fourier transform using a FFT algorithm. The weak damping rate in the oscillations of the square lattice case hinders the Fourier transform and we have to smooth the spectra with a gaussian. The details of the shape of $\tilde{\Phi}'(\omega)$ therefore depend on the choice of gaussian and the simulation time. However, the quantity which is of major concern to us, $\tilde{\Phi}'(0)$, only depends weakly on the transformation procedure.

In the kagomé case, there is no difficulty in obtaining the Fourier transform.

In Figs. 38a, b, and c we show $\tilde{\Phi}'(\omega)$ for the square lattice at three temperatures: 1, 0.1, and 0.02J. The reader should note the different timescales of the abscissa. As the temperature decreases from 1.0 to 0.1, the scale of the spectral density narrows and $\tilde{\Phi}'(0)$ increases. In addition, a number of spin wave-like peaks appear in the spectra. The narrowing of the spectral density with decreasing temperature is characteristic of a paramagnetic phase. Upon further cooling to 0.02J, $\tilde{\Phi}'(0)$ decreases and only one narrow peak centered at $\omega > 0$ is observed. This behavior is characteristic of an ordered phase and can be qualitatively understood from the results of step II. At low temperatures, only a narrow range of low energy excitations are accessible to the system; the correlation function is therefore combined from a number of $[\hat{S}(0) \cdot \hat{S}(t)]$ which resemble each other. The SACF shown in Fig. 36a is a typical example of one such $[\hat{S}(0) \cdot \hat{S}(t)]$. It results in a $\langle \hat{S}(0) \cdot \hat{S}(t) \rangle$ which can be described as an underdamped oscillator and a spectral density with a peak at $\omega > 0$. At high temperatures a wide range of high energy excitations are accessible to the system; the correlation function is expected to be overdamped and the maximum of $\tilde{\Phi}'(\omega)$ is expected at $\omega = 0$. In the kagomé lattice the situation is fundamentally different, as can be seen from Figs. 38d, e, and f. Although there is a narrowing of the spectral density, $\tilde{\Phi}'(0)$ continuously increases upon cooling. In other words, no phase transition is seen as $T \rightarrow 0$. This behavior can also be understood from step II; the SACF in the $\sqrt{3} \times \sqrt{3}$ shown in Fig. 36b is strongly damped even at very low excitation energies. It is therefore not surprising that $\langle \hat{S}(0) \cdot \hat{S}(t) \rangle$ is overdamped and that $\tilde{\Phi}'(\omega)$ is peaked at zero frequency for all temperatures.

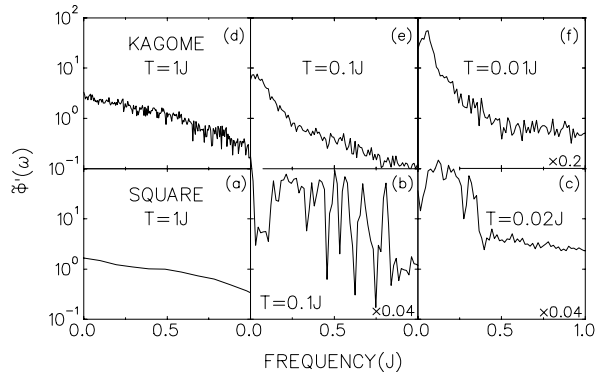


Figure 38: Spectral density $\tilde{\Phi}'(\omega)$ in the square lattice obtained at (a) $T = 1.0J$, (b) $T = 0.1J$, and (c) $T = 0.02J$, and in the kagomé lattice obtained at (d) $T = 1.0J$, (e) $T = 0.1J$, and (f) $T = 0.01J$.

We can now define the correlation time $\tau = \tilde{\Phi}'(0)$. In Fig. 39 we show τ (normalized by the value of τ at $T = 10J$) as a function of temperature for the kagomé and square lattices. The error bars are estimated from the variation of τ between different cycles. In this figure we also show simulation results for a kagomé lattice with 675 ($L = 15$) spins and 108 ($L = 6$) spins. In the square lattice we see a maximum in τ at $T = 0.1J$, while in the kagomé lattice, τ increases monotonically with decreasing temperature. In addition, we see a very weak lattice-size dependence in the kagomé case.

The peak of τ in the square case is not surprising, since at $T \sim 0.5J$ the correlation length reaches the lattice size and the system is effectively ordered.[47] However, the continuous increase of τ in the kagomé case, even for a small system, is not trivial, especially in view of the increase in the order parameter $m\sqrt{3}$ with decreasing lattice size at $T \rightarrow 0$. [23] It suggests that the difference between the square and kagomé lattices is due to the local motion of spins in the kagomé system, namely, the zero modes.

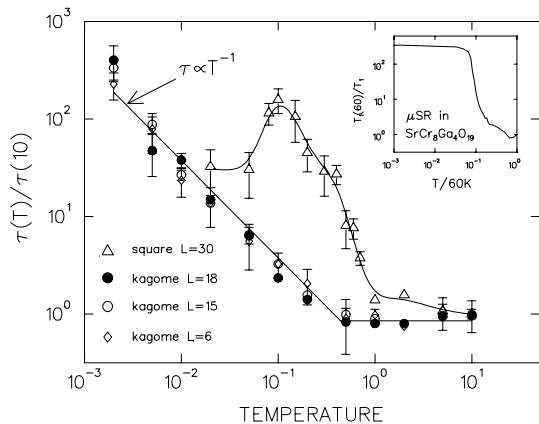


Figure 39: The correlation time τ normalized by the value of τ at $T = 10.0J$ is plotted against temperature in units of J . The normalization factors are: $1.12/J$ in the square with $L = 30$ spins, $2.40/J$ in the kagomé with $L = 18$ spins, $2.36/J$ in the kagomé with $L = 15$ spins, and $1.17/J$ in the kagomé with $L = 6$ spins. The solid lines are guides for the eye. The inset shows the experimental result for the μ^+ spin-lattice relaxation as a function of temperature in $\text{SrCr}_8\text{Ga}_4\text{O}_{19}$. [5]

The correlation time τ , is intimately related to the spin-lattice relaxation rate of the muon, as we have seen in chapter 2. The relation, when the static local field is small ($\omega_s \rightarrow 0$), is given by $1/T_1 \sim B^2\tau$ (see Eq. 31). [12] From our simulation we therefore anticipate the absence of a T_1 minimum in the kagomé lattice. Indeed, such an absence is observed in the μSR measurement of both the $\text{SrCr}_8\text{Ga}_4\text{O}_{19}$ and $\text{KCr}_3(\text{OH})_6$ (SCGO) presented in section 3.2 and 3.3. [5] The experimental

results in SCGO, normalized by $J = 60\text{ K}$, [20] are presented in the inset of Fig. 39. It should be noted that some differences between these simulations and the μSR experiment on SCGO and CrJ are anticipated: SCGO contains 14% nonmagnetic impurities on the kagomé plane, as well as magnetically active triangular planes, while CrJ could have some 3D interactions. It also should be noted that, at very low temperatures, quantum effects should also play an important role in the dynamics of these systems, although the fact that the spins are moderately large ($3/2$) favors the use of a classical model.

The data shown in Fig. 39 is too noisy to be accurately fitted to a specific model of critical dynamics. Nevertheless, the diagonal line in the kagomé case below $T = 0.5$ is plotted using $\tau \propto T^{-\nu z}$ where $\nu z = 1$. As can be seen, this line is in agreement with the simulation results and also with the critical exponents $\nu = 1/2$ and $z = 2$. These exponents arise in several models of critical dynamics where the correlation length diverges near the critical temperature. [48] However, the weak lattice size dependence of τ encourages us to believe that it is the local modes which are responsible for $\tau(T)$ in the kagomé lattice. This possibility will be explored in the next chapter.

We have found that the kagomé lattice has a very strong influence on the evolution of Heisenberg spins. Between the two kagomé ground states discussed here, the $q = 0$ is more stable against small excitations. In the $\sqrt{3} \times \sqrt{3}$ state the system forgets its initial configuration relatively quickly. Our simulations demonstrate that in the kagomé lattice the spectral density continuously narrows with no transition down to $T = 0$. This is in agreement with both experimental results and thermodynamical simulations. [22]

3.5 Conclusion and Discussion

3.5.1 Summary of Experimental results

Clearly, our experiments and simulation show fundamental differences between the kagomé lattice and other magnetic compounds. This is manifested in four effects:

(I) No peak in the muon relaxation rate. Indeed, the Cr spin slows down as the temperature is lowered, but the spectral density at low energy continuously increases down to low temperatures. In the μSR experiment, the relaxation rate saturates at low temperatures, while in the numerical simulation of classical Heisenberg spins the relaxation rate increases all the way to $T \rightarrow 0$. As was demonstrated in section 2.3 and by the simulation results in the square lattice, this behavior cannot result from collective excitations.

(II) No difference in the fitted correlation time τ^{fit} at temperatures below 7 K. Although there is a difference in the depolarization rates of the muon in the

SCGO samples with $x = 0$ and $x = 1.5$, we find that after taking into account the difference in the local field, τ^{fit} is nearly the same in both samples. The weak impurity dependence of the correlation time in the kagomé system is also supported by the numerical simulations and coincides with the weak dependence of the heat capacity in SCGO on dilution. This phenomenon is in contrast to our basic assumption of critical dynamics. Close to the critical point of a magnet we would expect the correlation length ξ and the correlation time τ to be related via $\tau \sim \xi^z$, where z is the dynamical exponent. Thus, we would expect a shorter correlation time in the diluted system than in the concentrated system since it must have a shorter correlation length, at a given temperature, by virtue of its missing ions. This basic assumption of critical dynamics doesn't seem to hold for the kagomé lattice leading us to speculate, again, that the dynamics of this lattice do not involve the long range correlations of spins.

(III) The Gaussian line shape in a LF- μ SR measurement indicates a small internal field (100 G) but does not decouple, even with a very strong external field. This effect cannot be accommodated with the relaxation theories described up to now. This line shape is observed in both the SCGO and CrJ, rendering it a seemingly intrinsic property of the dynamics in the kagomé lattice with Cr ions. When other methods are used to evaluate the order of magnitude of the internal field, a much higher value is found (10 kG). Faced with the discrepancy between our theories and experiments, we look back on our models of muon spin relaxation and realize that these models stem from the assumption of Markovian dynamical processes. Therefore, we speculate that the dynamics in SCGO and CrJ are not described by these types of processes.

(IV) The energy scale of the single ion anisotropy in SCGO (if it exists) is on the order of 0.1 K and is much smaller than T_g . Therefore this anisotropy is most likely not responsible for the observed difference between field cooled and zero field cooled measurements in this system.

These four effects are observed for the first time, as far as we know, in kagomé lattices and confirm our expectations of unique dynamical behavior in these systems. In what follows we offer some ideas as to how the observed dynamical phenomena in the kagomé lattice may come to be.

3.5.2 Speculations on Dynamics in the Kagomé lattice

In order to explain the discrepancy in the μ SR theory we came up with two possible scenarios. The first one concerns the muon as a probe. It is possible that the long range order is locally broken and the dynamic fluctuations are triggered by the presence of the muon.

The introduction of a muon breaks the time symmetry and could lead to non-Markovian processes. Although this scenario could possibly explain the line shape, it cannot explain the temperature dependence of the correlation time since the interaction of the system with the muon can be viewed as local heating which would then slightly increase the temperature locally. We would therefore still expect a $1/T_1$ maximum in this scenario.

The other model is based on the symmetry of the kagomé lattice. We have already shown that the collective modes cannot be responsible for the observed behavior in the kagomé lattice. We therefore first examine the influence of the local modes on the spectral density. Let us, for purposes of demonstration, evaluate the spectral density resulting only from initial conditions that lead to a rigid motion of the 6 spins on an hexagon in the $\sqrt{3} \times \sqrt{3}$ state. The same motion was used by von Delf and Henly to calculate tunneling probabilities in the quantum kagomé lattice.[27] The IC are obtained by keeping spins A and B (see Fig. 40) on the same plane with spin C, placing them symmetrically on both sides of it. The angle between spins A and B is taken to be 2θ . In this configuration the vector $[\hat{\mathbf{S}}_A(0) + \hat{\mathbf{S}}_B(0)]$ is parallel to $\hat{\mathbf{S}}_C(0)$, and the excitation energy is

$$E(\theta) = 3(2 \cos(\theta) - 1)^2.$$

The equations of motion are

$$\frac{d\hat{\mathbf{S}}_C}{dt} = \hat{\mathbf{S}}_C \times (\hat{\mathbf{S}}_A + \hat{\mathbf{S}}_B + \hat{\mathbf{S}}_{A'} + \hat{\mathbf{S}}_{B'}) \quad (65)$$

$$\frac{d\hat{\mathbf{S}}_{A/B}}{dt} = \hat{\mathbf{S}}_{A/B} \times (2\hat{\mathbf{S}}_C + 2\hat{\mathbf{S}}_{b/a}) \quad (66)$$

where the vectors $\hat{\mathbf{S}}_{A'}$ and $\hat{\mathbf{S}}_{B'}$ are neighbors of $\hat{\mathbf{S}}_C$ which are not shown in the figure. Their sum $(\hat{\mathbf{S}}_{A'} + \hat{\mathbf{S}}_{B'})$ is fixed in time and is also parallel to $\hat{\mathbf{S}}_C(0)$. The last equation can be rewritten as

$$\frac{d(\hat{\mathbf{S}}_A + \hat{\mathbf{S}}_B)}{dt} = 2(\hat{\mathbf{S}}_A + \hat{\mathbf{S}}_B) \times \hat{\mathbf{S}}_C \quad (67)$$

$$\frac{d(\hat{\mathbf{S}}_A - \hat{\mathbf{S}}_B)}{dt} = 2(\hat{\mathbf{S}}_A - \hat{\mathbf{S}}_B) \times (\hat{\mathbf{S}}_C + \hat{\mathbf{S}}_A + \hat{\mathbf{S}}_B) \quad (68)$$

Given our special initial conditions, we see from Eq. 65 and 67 that

$$\frac{d\hat{\mathbf{S}}_C}{dt} = 0 \quad (69)$$

$$\frac{d(\hat{\mathbf{S}}_A + \hat{\mathbf{S}}_B)}{dt} = 0. \quad (70)$$

From Eq. 68, we find that the vector $(\hat{\mathbf{S}}_A - \hat{\mathbf{S}}_B)$, and therefore $\hat{\mathbf{S}}_A$ and $\hat{\mathbf{S}}_B$, oscillate around the vector $2[\hat{\mathbf{S}}_C(0) + \hat{\mathbf{S}}_A(0) + \hat{\mathbf{S}}_B(0)]$ with a frequency

$$\omega(\theta) = 2[1 - 2 \cos(\theta)]. \quad (71)$$

This result leads to the spin-spin correlation function

$$\hat{\mathbf{S}}(t) \cdot \hat{\mathbf{S}}(0) = \cos^2(\theta) + \sin^2(\theta) \cos(\omega(\theta)t) \quad (72)$$

for spins A and B .

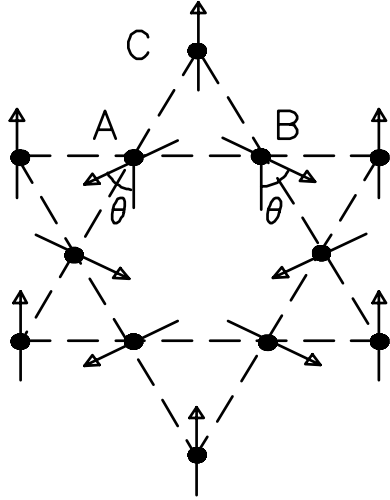


Figure 40: *The initial condition which lead to a rigid local motion of spins on the kagomé lattice*

Since $\tau = \lim_{\omega \rightarrow 0} \tilde{\Phi}'(\omega)$, we are only interested in $\tilde{\Phi}'(\omega)$ in the limit $\omega \rightarrow 0$. After eliminating the static terms we find

$$\begin{aligned} \tilde{\Phi}'(\omega) &\propto \int_0^\pi \frac{\exp(-E(\theta)/T)}{Z} \sin^2(\theta) \delta(\omega - \omega(\theta)) d\theta \\ &= \frac{(12 + 4\omega - \omega^2)^{\frac{1}{2}} \exp(-3\omega^2/4T)}{16Z}. \end{aligned} \quad (73)$$

where the partition function Z is given by

$$Z = \int d\theta \exp(-E(\theta)/T).$$

Since $E(\theta) \propto \theta^4$, to lowest order in θ , we find $Z \propto T^{1/4}$ at low temperatures.

Equation 73 has two consequences: (I) in the limit $\omega \rightarrow 0$ we find that the correlation time (or spectral density) increases as $\tau \propto T^{-1/4}$. (II) at very low frequencies we expect $\tilde{\Phi}'(\omega) = \tau(1 + \omega/6)$, and the spectral density increases with ω before it starts to decrease. Although in this model we find a mode which could result in an increasing correlation time as $T \rightarrow 0$, the critical exponent obtained here is different from the one we find in the simulation, and the initial increase of the spectral density shown in Fig. 38f is too rapid. In addition we know that the system has a tendency towards coplanarity. This tendency does not exist in our simple model. We must then conclude that this mode is oversimplified.

We therefore go one step further and suggest that there are two additional time scales involved in the problem: the first one, τ_1 , is the time scale in which the system relaxes into a $\sqrt{3} \times \sqrt{3}$ state (in the vicinity of the probe) once it has been excited out of it. The second, τ_2 , is the time scale in which it takes the system to find itself in a configuration which can lead to a local motion. Since the $\sqrt{3} \times \sqrt{3}$ state is the most favorable, these time scales are not equal, and they both depend on the size of the area which is to be moving. This type of motion is usually what we expect from non-ergodic systems. In such systems the degrees of freedom become confined to a small region of phase space and only rarely travel to other areas of phase space because of an entropy wall. However, once the system has traveled and arrived in a new area of phase space, it remains there for some time before embarking on a new journey. In our model the system is only weakly locked in a particular coplanar state and will often visit other coplanar states since the entropy wall is relatively small. Unfortunately, at this point, we can not offer a solution for the spectral density in this model. However, we can show that some of the features observed in our experiment could be understood in light of it.

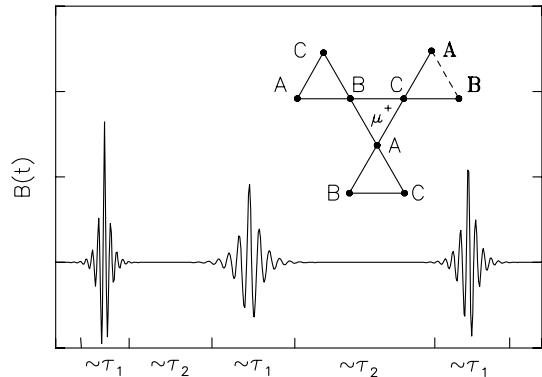


Figure 41: *The local field in the domain flip model. The inset shows a spin configuration which leads to a local field at the center of a triangle.*

Let us imagine a situation in which the field at the muon site is zero for the $\sqrt{3} \times \sqrt{3}$ state but different from zero for another coplanar state. This situation can occur if the muon resides in the center of a triangle. For example, in the inset of Fig. 41 we show a spin configuration near a muon which is obtained from the $\sqrt{3} \times \sqrt{3}$ by interchanging two spins (marked in bold). The field at the muon site in this case is not zero. An example for the time evolution of the local field at the muon site according to this model is shown in Fig. 41. In this situation the evolution of the muon polarization will be governed by a stochastic process with two different types of time segments. During the segments

of time in which the local field is zero, there will be no evolution of the polarization whatsoever, while during the time segments in which the local field is non-zero, the polarization will evolve in a manner similar to the one described in section 2. It was first noticed by Uemura *et al.*[49] that the measured muon polarization function, taking both the zero and non-zero field time segments into account ($P_z^{2S}(t)$), is the same as the polarization function obtained by cutting out the zero field segments and considering only the non-zero field segments ($P_z^{1S}(t)$). However, the time has to be re-scaled as $t \rightarrow r \cdot t$ where r is the portion of time the muon experience a finite field. In the language of the local mode excitations $r = \tau_1/(\tau_1 + \tau_2)$. This time-rescaling is a consequence of the fact that in a LF experiment the muon polarization evolves in time only where there is a local source of magnetic field. Therefore, in any interval of time dt , only during the portion $r \cdot dt$ does the polarization relax.

If we now look at our LF- μ SR experiment in SCGO or CrJ, with the minute LF of $H_L = 100$ G, we see that the root mean square of the local field Δ is mostly determined by the depolarization at early time where $P_z(t) = P_z^{2S}(t) \sim \exp(-\Delta^2 t^2)$. However, this polarization is exactly

$$P_z^{2S}(t) = P_z^{1S}(r \cdot t) = \exp(-[\Delta^{1S} \cdot r \cdot t]^2)$$

where Δ^{1S} is the RMS of the field taking only the non-zero field segment into account. Thus, according to this model $\Delta = r \cdot \Delta^{1S}$ and the local field, when it is not zero, is $1/r$ times larger than what we have concluded it to be from our measurements at low LF. We can now understand the unexpected weak decoupling. In order to make $P_z^{2S} = 1$ we must make $P_z^{1S} = 1$. Assuming that the fluctuation $1/\tau^1 \sim \Delta^{1S}$ we must have for this decoupling $H_L \simeq 5\Delta^{1S} = 5\Delta/r$. If, for example, $r = 0.05$ in the $x = 0$ SCGO sample, only a field ~ 1 T would decouple the spectra as roughly observed in the experiment.[49]

Recently, Cherepanov considered a dynamical model which is based on domain formation and regional flips. However, he only provides estimates for dynamical exponents and not for the actual time scales. Therefore, we cannot test the applicability of his model to our measurements as yet.

This model could account for the weak dependence of dynamical properties on dilution (and lattice size in the simulation), and could possibly explain the temperature dependence of the correlation time; it could also explain the decoupling problem. Its weakness is in the necessary assumption of a muon site which could not be the same for a variety of compounds. It would be interesting to see if this model could give rise to a T^2 dependence of the heat capacity and to the observed data in neutron scattering. It should also be pointed out that the question of why the correlation time sat-

urates at low temperatures remains open. This saturation could follow from some other interaction which becomes important at low temperatures, or, as Uemura *et al.* suggested, from quantum effects.[49]

4 The “Infinite Layer” Cuprate Antiferromagnets

4.1 Introduction

The discovery of high-temperature superconductivity in cuprate systems has generated considerable interest in the magnetic properties of their undoped parent compounds.[50] This is partly based on the widely accepted conjecture that the superconductivity of the high- T_c cuprates is intimately related to the magnetic interactions within the CuO_2 planes. Another source of interest comes from the fact that some of the parent antiferromagnets, such as La_2CuO_4 , represent nearly ideal 2-dimensional Heisenberg spin systems.[51] The so-called 123 compound $\text{YBa}_2\text{Cu}_3\text{O}_7$ is perhaps the most extensively studied among the various cuprates. The 123 system has a layered perovskite structure, shown in Fig. 42, with three copper-oxygen layers stacked along the tetragonal \hat{c} axis. Two of these layers have oxygen ions between the copper ions in both the \hat{a} and \hat{b} directions, and thus are called CuO_2 plane layers. The third layer, called the CuO chain layer, has oxygen ions only along the \hat{b} axis: $\text{YBa}_2\text{Cu}_3\text{O}_y$ with $y = 7.0$ has complete CuO chains, while some oxygen atoms are missing and the chains are fragmental for materials with $y < 7.0$. Since the CuO_2 plane and the CuO chain represent two important building blocks of high- T_c cuprate compounds, it is useful to study their magnetic behavior separately. In this chapter and the next one we present such a study. Here we concentrate on $\text{Ca}_{0.86}\text{Sr}_{0.14}\text{CuO}_2$ with the CuO_2 layers structure, and in chapter 5 we investigate compounds with the CuO chain structure.

The layered compound $\text{Ca}_{0.86}\text{Sr}_{0.14}\text{CuO}_2$ is characterized by the highest density of CuO_2 planes among the various cuprate systems, with no other layers sandwiched between the CuO_2 planes (see Fig. 42).[52] Systems with this structure are often called “infinite layer” (ILy) compounds. The first infinite layer material was reported by Roth.[53] At ambient pressure the structure of $\text{Sr}_{1-x}\text{Ca}_x\text{CuO}_2$ can only be stabilized with $x \sim 0.1$,[52] but compounds with x ranging up to 1 can be synthesized at high pressure and temperature.[54] The present system is also the undoped parent compound of several cuprate superconductors having the same crystal structure; recently Azuma *et al.* [55] reported the synthesis of $(\text{Sr}_{1-x}\text{Ca}_x)_{1-y}\text{CuO}_2$ with T_c up to 110 K, and Smith *et al.* [56] obtained electron-doped ILy superconductors $(\text{Sr}_{1-x}\text{Nd}_x)_{1-y}\text{CuO}_2$ and $(\text{Sr}_{1-x}\text{La}_x)_{1-y}\text{CuO}_2$ with $T_c \sim 50$ K.

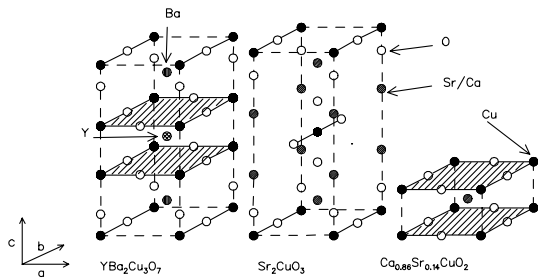


Figure 42: Crystal structures of $YBa_2Cu_3O_7$, Sr_2CuO_3 , and $Ca_{0.86}Sr_{0.14}CuO_2$. The exchange couplings along layers and chains are emphasized by the solid lines.

Our specimen of $Ca_{0.86}Sr_{0.14}CuO_2$ was prepared by calcinating stoichiometric ratios of $CaCO_3$, $SrCO_3$, and CuO for 12 hours in air. After several repetitions of calcination and regrinding, the powder was pressed into pellets which were finally sintered at $980^\circ C$ for 12 hours. The specimen was checked by X-ray diffraction; it was found that the $Ca_{0.86}Sr_{0.14}CuO_2$ has a tetragonal structure with lattice constants $a = 3.8611 \text{ \AA}$ and $c = 3.1995 \text{ \AA}$, and contains no apical oxygen atoms. We could not find any impurity peak with an intensity greater than 1% of the (011)-peak height of the ILY-structure. Simple valence counting yields a valence of +2 for the copper ions.

In our μSR experiments we find antiferromagnetic order in this system. The Néel temperature $T_N = 540 \pm 5 \text{ K}$ found by μSR is in agreement with the value $T_N = 537 \pm 5 \text{ K}$ obtained by neutron scattering measurements.[57] We also measure the order parameter as a function of temperature and compare it with the order parameters of other cuprates systems with larger layer separation. This comparison demonstrates the influence of dimensionality on the magnetic properties of the cuprates. In addition to studies of various intrinsic magnetic properties, we also present results on the muon site and diffusion in the ILY system. The simplicity of its crystal structure makes this system nearly ideal for such studies. $Ca_{0.86}Sr_{0.14}CuO_2$ orders magnetically at a temperature high enough for muons to hop between interstitial sites within the antiferromagnetically ordered state. We can study the temperature dependence of the hopping rate via the fast dephasing of the muon spin precession, using the phenomenological treatment described in section 2.4. Results on the diffusion rate may be compared with models involving the electrostatic potential at the muon site. In order to look for possible muon sites in ILY, we compare the muon spin rotation frequency observed at low temperatures with a model calculation for the local field assuming a dipolar interaction.

This chapter is organized as follows: In section 4.2,

we present μSR results on $Ca_{0.86}Sr_{0.14}CuO_2$ and compare them with neutron scattering measurements.[57] Muon diffusion in this system is discussed in section 4.3. The muon site in this system is treated in section 4.4. In section 4.5, we compare the present results in $Ca_{0.86}Sr_{0.14}CuO_2$ with previous μSR results for La_2CuO_4 ,[58] $Sr_2CuO_2Cl_2$,[51] and discuss differences in their magnetic properties within the framework of a quasi 2-dimensional Heisenberg model.

4.2 μSR Measurements

The μSR experiments were performed at the M15 surface muon channel at TRIUMF. Several pieces of sintered polycrystalline specimens, each approximately $5 \times 5 \times 0.5 \text{ mm}$, were mounted in a He gas flow cryostat which operates in a temperature region from 3.0 to 300 K. An oven was used to obtain higher temperatures. Fig. 43 shows typical time spectra of the muon polarization observed in $Ca_{0.86}Sr_{0.14}CuO_2$ between 400 K and 545 K. A large increase in the muon spin depolarization rate is seen between 545 K and 535 K. The relaxation at 545 K is characteristic of nuclear magnetic moments, whereas the relaxation at 535 K is due to the freezing of electronic moments. The Néel temperature $T_N = 540 \pm 5 \text{ K}$, estimated from Fig. 43, is in very good agreement with $T_N = 537 \pm 5 \text{ K}$ found in neutron scattering measurements.[57] Another indication of magnetic order comes from magnon Raman scattering at room temperature in which a fairly strong but broad Raman band around 3000 cm^{-1} has been attributed to spin-pair (two-magnon) excitations.[59]

Fig. 44 shows time spectra at 102, 245 and 360 K. At 102 K and 245 K spin precession is evident and the signal has a characteristic exponential decay. This indicates the existence of static magnetic order at those temperatures. Fourier transforms of the spectra at two temperatures are shown in the insert of Fig. 45. At 102 K, two frequencies are present, but only one frequency exists at 245 K. Such a splitting of the precession frequency was also seen in $Sr_2CuO_2Cl_2$ and can be the result of either a unique muon site that lacks the symmetry of the magnetic system, or two different muon sites both having the symmetry of the magnetic system. Muon hopping, with a rate increasing with increasing temperature, may then be responsible for the merging of the two frequencies into one. In that case some intermediate frequency will be measured when the hopping rate is much larger than the frequency at each site. [60, 61] For further discussion of the two frequencies, see section 4.3.

The μSR data below 300 K is analyzed with Eq. 10: we use two finite frequencies below 225 K and only one above 225 K. The high precession frequency indicates a strong local field due to the electronic moments, and the effect of nuclear moments becomes insignificant, as long as the determination of precession frequency is

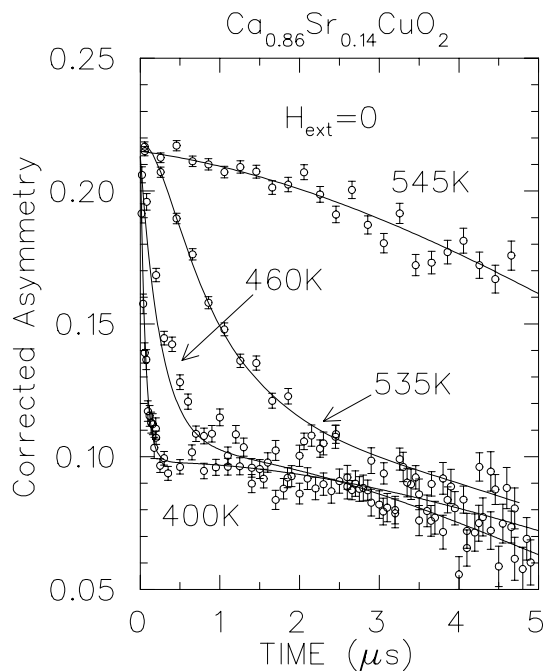


Figure 43: Corrected asymmetry above and below the Néel temperature in $\text{Ca}_{0.86}\text{Sr}_{0.14}\text{CuO}_2$.

concerned. We therefore assume $1/T_G = 0$ in the analysis at low temperatures. Since our data cannot resolve different spin-lattice relaxation times, we assume a single T_1 for the non-precessing signal in our analysis. Unlike the frequency, the values obtained for T_1 were not well determined and depended on the details of the fitting scheme; therefore we do not present them here. The fitted asymmetry of the precessing component is approximately 44% of the total asymmetry; the difference from the ideal case of $2/3$ may be ascribed to some non-precessing background component and/or a possible missing precessing component having a very high frequency or relaxation rate. Fig. 45 (solid circles) illustrates the temperature dependence of the muon precession frequency in $\text{Ca}_{0.86}\text{Sr}_{0.14}\text{CuO}_2$ normalized by 17.93 MHz. Below 225 K the curve splits into two lines centered around 16 MHz ($H_{loc} = 1.2$ kG) with the higher frequency approaching 17.9(1) MHz (1.32(1) kG) and the lower frequency approaching 14.3 MHz (1.06(1) kG). The precession frequencies depend only very weakly on the temperature below $0.5T_N$.

In most non-metallic magnetic systems, the perturbation caused by the μ^+ to the magnetism of the host material is known to be minimal. We can expect the muon spin precession frequency $f(T)$ to be proportional to the sublattice magnetization $M_s(T)$, as long as the muon site in the crystal is not altered. In neutron diffraction experiments, one measures the intensity of an antiferromagnetic Bragg peak, which is usually proportional to M_s^2 ($I_B \propto M_s^2$). In Fig. 45 we

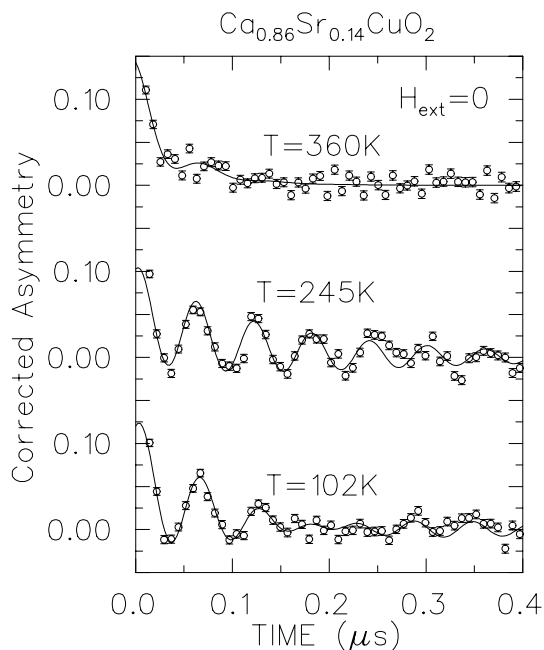


Figure 44: Corrected asymmetry deep in the magnetically ordered state. The solid curves are fits to Equations 10 and 55 as described in the text.

also included the normalized $\sqrt{I_B}$ obtained by Vaknin *et al.* [62] The two magnetization curves match reasonably well in the intermediate temperature range. A power law ($M(T) \propto (1 - T/T_N)^{0.26}$) and molecular field magnetization curves are also displayed: the former fits the results well only near T_N while the latter fits only at low temperatures.

4.3 Muon Diffusion

As shown in Fig. 44, the oscillations in the time spectra from $\text{Ca}_{0.86}\text{Sr}_{0.14}\text{CuO}_2$ start to disappear above 300 K, and are not observed at all at 400 K, even though a large static field ($B \sim 1$ kG) should exist at this temperature at the muon site. We attribute this strong dephasing of the muon spin precession to muon hopping between sites of opposite magnetic field directions (due to the two sublattices in the ordered state of an antiferromagnet). In fact, such μ^+ hopping has been observed in the 123 system.[63] Equation 55 is used to fit the μSR time spectra between 306 K and 460 K assuming that the transverse relaxation caused by the hopping is much larger than any other sources of T_2 . At 500 K and above, the relaxation is caused by the combination of hopping and the slowing down of the Cu spins in the critical regime. The relaxation behavior in this temperature range is beyond the scope of our model and is not discussed here.

The temperature dependence of the deduced hopping rate is shown in Fig. 46, where the results are com-

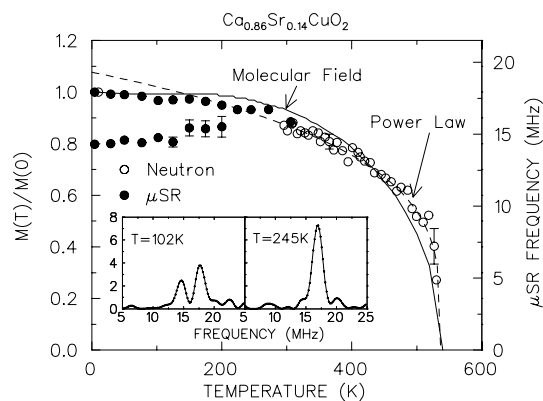


Figure 45: The temperature dependence of the muon spin precision frequency in zero-field along with neutron scattering data[57] observed in $\text{Ca}_{0.86}\text{Sr}_{0.14}\text{CuO}_2$. Below 225 K two frequencies are seen. The solid lines are a power law $M(T) \propto (1 - T/T_N)^{0.26}$ and a molecular field curve. Fourier power spectra are shown in the insert.

pared with an Arrhenius law $\nu = \nu_0 \exp(-E_a/k_B T)$. The results agree reasonably with a straight line characterized by an activation energy $E_a = 0.39(1)$ eV and an asymptotic hopping rate $\nu_0 = 1.8(8) \times 10^{13} \text{ sec}^{-1}$. These are the first quantitative results for muon diffusion and the associated energy barrier in cuprates. The measured activation energy can be compared with the numerical calculations performed by Li *et al.* of the electrostatic potential in 123.[64] According to their calculation, a muon trapped in a site between the two CuO_2 layers needs roughly 0.5 eV to escape from its site.

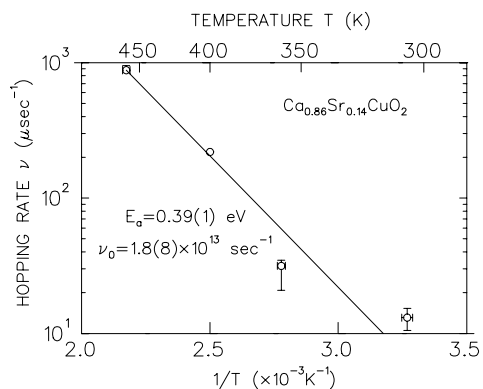


Figure 46: Hopping rate as a function of temperature in $\text{Ca}_{0.86}\text{Sr}_{0.14}\text{CuO}_2$.

4.4 Muon Sites

In the antiferromagnetic state of an insulator, we assume that the magnetic field seen by the muon is given by the dipolar field

$$H(\mathbf{R}_\mu) = \sum_i \frac{-\boldsymbol{\mu}_{\text{Cu}}(\mathbf{r}_i - \mathbf{R}_\mu)^2 + 3[\boldsymbol{\mu}_{\text{Cu}} \cdot (\mathbf{r}_i - \mathbf{R}_\mu)](\mathbf{r}_i - \mathbf{R}_\mu)}{|\mathbf{r}_i - \mathbf{R}_\mu|^5} \quad (74)$$

where \mathbf{r}_i and \mathbf{R}_μ are the position of the i th Cu^{+2} ion and muon respectively, and $\boldsymbol{\mu}_{\text{Cu}}$ is the effective magnetic moment of the Cu^{+2} ion. Neutron scattering and susceptibility measurements[57] indicate that an effective moment of $0.51 \mu_B/\text{Cu}$ lies in the $\hat{\mathbf{a}}\hat{\mathbf{b}}$ plane (in the ordered state of the ILy). Here we assume that the moments make an angle of 45° with the $\hat{\mathbf{a}}$ axis in the $\hat{\mathbf{a}}\hat{\mathbf{b}}$ plane, as was found in LaCuO_4 and $\text{Sr}_2\text{CuO}_2\text{Cl}_2$. [62] Since this moment does not involve any orbital component, the electrostatic interactions determining the muon site should not be different between the paramagnetic and ordered states. It is then reasonable to assume that the muon site preserves the tetragonal symmetry of the crystal lattice. In contrast, the magnetic field in the cell at the ordered state has lower symmetry; *i.e.*, the fields in two crystallographically equivalent sites are not necessarily equal.

To account for possible muon sites which could correspond to the two observed frequencies, we search for sites, according to the restriction $H = 1.32(1)$ or $H = 1.06(1)$ kG, and obtain their coordinates (x, y, z) in the unit cell. Then the field for the crystallographically symmetric site $(x, b-y, z)$ is calculated. If the resulting field is either 1.32(1) or 1.06(1) kG, such a site is a candidate. Otherwise, we should have seen a different frequency than the observed ones. There are two different types of sites: we refer to all sites where $H(x, y, z) = H(x, b-y, z)$ as type-A sites. There are two kinds of type-A site; A_{high} where $H = 1.32(1)$ and A_{low} where $H = 1.06(1)$ kG. If the muon occupies a type-A site we need to assume the existence of two crystallographically non-equivalent muon sites to obtain two frequencies. The other type is when $H(x, y, z)$ and $H(x, b-y, z)$ are not equal to each other, but one is 1.32(1) and the other is 1.06(1) kG. We call such a site type B. Only one crystallographic site of type-B is needed in order to account for the two frequencies.

We performed a calculation of the local field in a lattice consisting of 8^3 unit cells, which gives an error in the calculated field comparable to the measured ones. A grid of 500^3 points is used to scan within the unit cell. Type A sites are found only in the sides of the tetragon and in a plane passing through the Sr ion and midway between two adjacent Cu ions. Half of the $\hat{\mathbf{c}}\hat{\mathbf{b}}$ plane and a plane passing through the Sr ion are plotted in Fig. 47. Since electrostatic arguments suggest that muon sites are roughly 1 Å away from an oxygen ion,[65] we highlighted this sphere by a solid line, in the

figure. We found A_{high} (solid circle) and A_{low} (empty circle) sites roughly 1 Å away from the oxygen ion and very close to each other: the closest distance between A_{high} and A_{low} is 0.25 Å. If a muon stops randomly at either of these two type-A sites at low temperatures, two frequencies will be observed. One can then explain the merging of the two frequencies at elevated temperatures by assuming that the muon starts to hop from one site to the other. [60, 61] In that case, the increase of the low frequency and the increase of the error bars of that frequency as seen in Fig. 45, suggest that the site with low frequency is metastable.

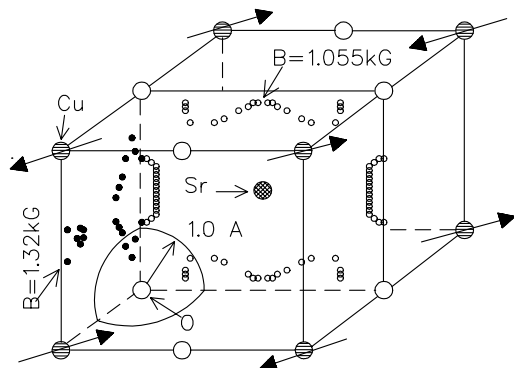


Figure 47: Possible muon sites; only half of the $\hat{c}\hat{b}$ plane and a plane passing through the Sr ion and between two Cu ions are plotted. On these planes, only type-A sites were found.

We also found several type-B sites, which exist at a reasonable distance from an oxygen ion: the closest distance to oxygen is 1.25 Å. If the muon resides in any of these type-B sites at low temperatures a splitting of the frequency will be seen due to the lower symmetry of the magnetic lattice. However, the measured ratio between the muon precession asymmetry of the high frequency signal to the low frequency signal is roughly 6 at low temperatures. If the muon stops in a type-B site, this ratio is expected to be 1. In addition, without rapid hopping between adjacent type-B sites, two frequencies are expected at any temperature. Hopping between two type-B sites is less likely because we would then expect a symmetric change in the frequency as the temperature increases, in contrast to the observed change. We therefore consider that the muon sites in $\text{Ca}_{0.86}\text{Sr}_{0.14}\text{CuO}_2$ are probably type-A sites.

4.5 Discussion

Figure 48 shows the sub-lattice magnetization curves of three compounds, all containing CuO_2 plane layers,

with different inter-layer distances d_{CuO} : $\text{Ca}_{0.86}\text{Sr}_{0.14}\text{CuO}_2$ ($d_{\text{CuO}} = 3.1995$ Å), $\text{La}_2\text{CuO}_{4-0.015}$ ($d_{\text{CuO}} = 6.595$ Å) [66] and $\text{Sr}_2\text{CuO}_2\text{Cl}_2$ ($d_{\text{CuO}} = 7.765$ Å) [67]. We see that the sub-lattice magnetization decreases most quickly with temperature when the interlayer separation is greatest. This can be attributed to a decrease in the effective dimensionality for systems with larger d_{CuO} . For antiferromagnetic spin waves with linear dispersion, the density of states is given as $n(\omega) \propto \omega^2$ in 3D systems, while $n(\omega) \propto \omega$ in 2D systems. Consequently, systems with lower dimensionality have a larger spectral weight of low energy thermal magnon excitations. The sublattice magnetization is more easily destroyed by thermal excitations in 2D systems than in 3D systems. We see in Figure 48 that increasing the inter-layer distance d_{CuO} takes the cuprate antiferromagnets closer to an ideal 2-dimensional magnetic system (as one would expect).

To consider this behavior more quantitatively, we compare the experimental results with calculations for a simplified quasi two-dimensional Heisenberg model previously studied by Lines.[68] It is known that ideal two-dimensional Heisenberg systems do not undergo magnetic order at finite temperatures. To account for the deviation from the 2D Heisenberg situation, this model introduces a uniaxial anisotropy field H_A which stabilizes the magnetic order. The Hamiltonian is then given by

$$\mathcal{H} = \sum_{NN} JS_u \cdot S_d - \sum_u g\mu_B H_A S_u^z + \sum_d g\mu_B H_A S_d^z \quad (75)$$

where the subscript u(d) labels spins on “up” (“down”) sites in the ordered phase, and the first summation runs over all nearest-neighbor spin pairs. The solution for $M(T)/M(0)$ was given by Lines[68], using a random-phase Green’s function approximation. This solution depends on the parameter $D = g\mu_B H_A / 4J$ which is proportional to the ratio of the anisotropy energy to the exchange energy. We calculated $M(T)/M(0)$ for various values of D , as described in Ref. [51], and show the results with the solid lines in Fig. 48. The temperature dependence of the sub-lattice magnetization is very sensitive to the inclusion of a small anisotropy term: M decays very quickly with increasing T for small D values. We should note that, in the three cuprate systems mentioned above, the real mechanism for deviation from the ideal 2D Heisenberg interaction may be different from the uni-axial anisotropy assumed in the model Hamiltonian. In fact, an inter-layer magnetic coupling, i.e., a small three dimensional interaction, is more likely in our systems. Comparison of the model calculation and the observed results, however, allows us to roughly estimate the effective energy scale of the additional term to the ideal 2D Heisenberg interaction. Figure 48 demonstrates that an increasing inter-layer distance d_{CuO} results in a very rapid reduction of such an additional anisotropy and/or a 3D term. This is

quite reasonable if the 3D inter-layer magnetic coupling plays a predominant role in the cross-over from 3D to 2D behavior. Thus, $\text{Ca}_{0.86}\text{Sr}_{0.14}\text{CuO}_2$ is more appropriately described by a 3D model whereas $\text{Sr}_2\text{CuO}_2\text{Cl}_2$ is a very good example of a quasi 2D Heisenberg system.

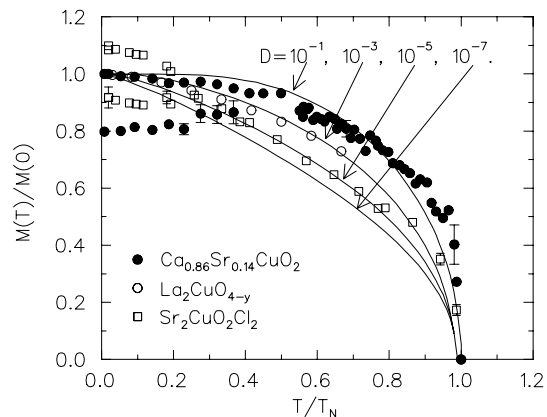


Figure 48: Comparison of $M(T)$ determined by μSR for compounds with three different layer separations. The solid lines represent a quasi two-dimensional Heisenberg model. The parameter D is given by $D = g\mu_B H_A / 45J$ where H_A is the anisotropy field.

The exchange interaction within the CuO_2 planes in $\text{Ca}_{0.86}\text{Sr}_{0.14}\text{CuO}_2$ system was estimated to be $J \sim 1000$ K from susceptibility measurements, [57] and two magnon Raman scattering.[59] This value is in agreement with the J_{2d} of $\text{La}_{2-x}\text{CuO}_{4-y}$ determined from neutron scattering.[69] The expected Néel temperature from mean field theory is ZJ , where Z is the nearest neighbor coordination. Thus the suppression factor of the ordering temperature $S = T_N/ZJ > 0.1$. As we shall see in the next chapter, systems with lower dimensionality, i.e. spin chains, have a much smaller suppression factor.

5 The “Infinite-Chain” Cuprate Antiferromagnets

5.1 Introduction

The subject of one-dimensional (1D) spin 1/2 chains has drawn considerable theoretical and experimental attention in the past few years.[70, 71] However, this research is restricted by the difficulty of finding systems in which the magnetic interaction is approximately 1D. Consequently, there is considerable interest in new materials which could better serve this study. Because of their crystal structure the “Infinite Chain” (Ich) compounds R_2CuO_3 (R is Sr or Ca) are possibly such

materials. In the orthorhombic lattice of the Ich compounds, shown in Fig. 42, the CuO chains lie along the $\hat{\mathbf{b}}$ axis ($b = 3.49$ Å), while along the $\hat{\mathbf{a}}$ axis ($a = 3.91$ Å) there are no oxygen atoms to carry the superexchange interaction. The distance between the Cu atoms along the $\hat{\mathbf{c}}$ axis ($c = 12.70$ Å) is roughly three times as large as this distance along the $\hat{\mathbf{a}}$ or $\hat{\mathbf{b}}$ axis.[72, 7] This structure leads us to anticipate 1D behavior in the Ich systems.

In addition, R_2CuO_3 , has a structure resembling the chain layer of the 123 system, as shown in Fig. 42. Comparison of these two systems could help us understand the role of dimensionality in the magnetic properties of cuprates. To date, no information has been available on the magnetic properties of R_2CuO_3 , except for the fact that two-magnon Raman scattering was not seen in this system at room temperature.[72] Chemical charge counting arguments suggest that R_2CuO_3 has CuO chains without free charge carriers.

Our μSR measurements in R_2CuO_3 find antiferromagnetic long range order. We also confirm the low dimensionality of the Ich by comparing the Néel temperature obtained by the μSR technique with the exchange interaction deduced from two magnon Raman scattering and susceptibility experiments. We find in this system that $T_N/ZJ_{1d} < 0.01$. This ratio is smaller than any other prototypical 2D [73] or 1D [74] spin system known to us. The μSR experiment is also used to determine the magnetic properties of the R_2CuO_3 in the ordered state. What follows is a detailed presentation of our data, divided into two separate subsections concerning the Ca_2CuO_3 and the Sr_2CuO_3 , followed by a discussion.

5.2 The Ca_2CuO_3 system

The Ca_2CuO_3 sample is prepared by a sintering process similar to that used for the $\text{Ca}_{0.86}\text{Sr}_{0.14}\text{CuO}_2$ sample. Powders of CaCO_3 and CuO are mixed with the ratio of 2:1 and are calcined at 960-970 °C for 12 hours in air. The powder is then pressed into pellets and sintered at 1000°C for 12 hours. The X-ray diffraction pattern is characterized by the peaks of the Ich structure, except for several small peaks of unknown origin with intensities less than 2.5% of the (011)-peak intensity.

5.2.1 μSR measurements

Fig. 49 shows Zero Field (ZF) μSR time spectra measured in Ca_2CuO_3 . At 13 K we find only muon spin relaxation, while at 11 K we find muon spin oscillations, which indicate a static local field. Therefore, the Néel temperature lies in the range $11 < T_N < 13$ K. The critical region of less than 2 K is rather small and is consistent with a first order phase transition. The

increase of oscillation amplitude at low temperatures indicates the onset of long range magnetic order.

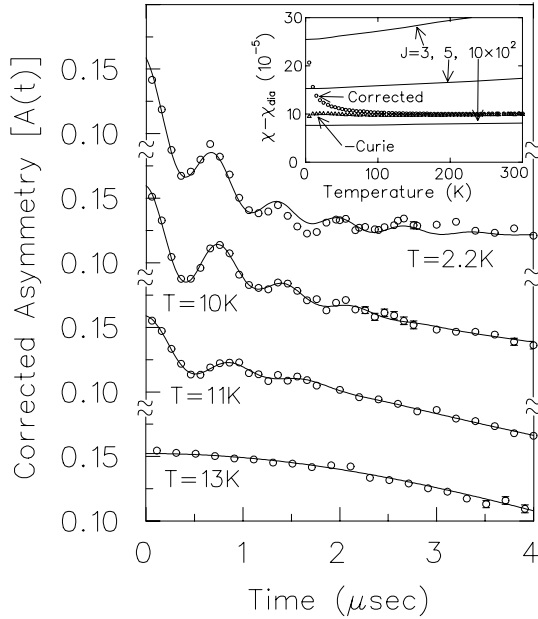


Figure 49: Zero field μ SR data in Ca_2CuO_3 . The inset shows both the corrected susceptibility $\chi - \chi_{\text{dia}}$ (in units of emu/G-mole), and the corrected susceptibility with a Curie term subtracted as described in the text. The inset also shows the expected susceptibility in a one-dimensional model.[75]

In longitudinal field μ SR measurements shown in Fig. 50, no dynamical fluctuations are found around T_N or at low temperatures. An external LF of the same strength as the internal field easily decouples the spectrum. This indicates that the main source of muon spin relaxation is static field modulations.

After several attempts we find that the best fit to the μ SR data is achieved with the form

$$A(t) = A_d e^{-t/T_L} + e^{-(t/T_G)^2} [A_1 \cos(2\pi f_1 t) + A_2 \cos(2\pi f_2 t)]. \quad (76)$$

The three amplitudes are fixed, and the contribution to the relaxation from nuclear moments and background is deduced from the high temperature data. It should be noted that the values we obtain for the frequencies depend very weakly on the fitting scheme. The presence of two frequencies could be a result of two muon sites, or a unique crystallographic site, which is not symmetric with respect to the magnetic lattice. That the observed asymmetries are different - $A_1 = 0.008$ and $A_2 = 0.0175$ (with $A_d = 0.11$) - supports the first possibility. Interestingly, the muon relaxation function in Ca_2CuO_3 is very similar to the one observed in the metallic spin density wave system $(\text{TMTSF})_2\text{-X}$, even though the ICh is insulating.[76]

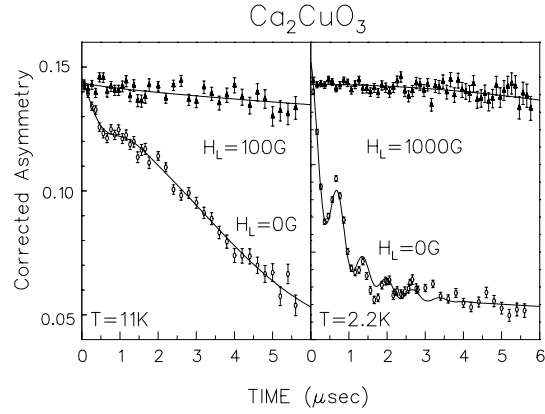


Figure 50: LF- μ SR data in Ca_2CuO_3 (a) near the critical region and (b) at low temperature.

The temperature dependence of the two fitted frequencies is shown in Fig. 51. We see a fast reduction in the frequencies with increasing temperature, expected for the sub-lattice magnetization of a low dimensional spin system. The same behavior is observed in the sister compound Sr_2CuO_3 . [7] The similar temperature dependence of the two frequencies supports the assumption that they result from two different muon sites. In the inset of this figure we show the parameters $1/T_L$ and $1/T_G$ as a function of temperature. The absence of rapid dynamical fluctuations at low temperatures in a LF- μ SR measurement suggests that the T_L relaxation originates from a random component of the local field which is static or at most slowly fluctuating (on a time scale of 1 MHz). The increase in $1/T_L$ as $T \rightarrow 0$ is ascribed to an increase in the RMS of this random field. The relaxation of the oscillating part, $1/T_G$, could also result from static field inhomogeneity.

5.2.2 Susceptibility Measurements

The dc-susceptibility measurements were made using a commercial SQUID magnetometer between 5 K and 300 K. The susceptibility data appearing in the inset of Fig. 49 are obtained after subtracting core diamagnetism ($\chi_{\text{dia}} = -78 \times 10^{-6}$ emu/G-mole) from the measured values.[77] In this figure we also plot the susceptibility after subtracting a magnetic impurity contribution, which was assumed to follow a Curie law. The estimated magnetic impurity density, assuming Cu^{+2} impurities, is 0.13%. In addition, in the inset of Fig. 49, we compare the susceptibility measurement with a model calculation for the 1D Heisenberg spin chain, consisting of $S = 1/2$ moments coupled antiferromagnetically, as given by Bonner and Fisher. [75] The model was solved numerically for the nearest neighbor exchange interaction between N moments on

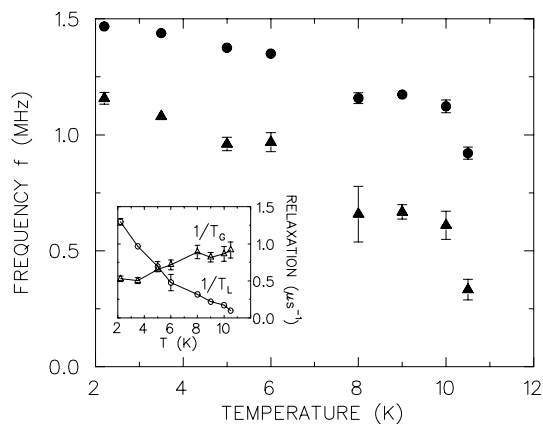


Figure 51: *The temperature dependence of the two frequencies in Ca_2CuO_3 . The inset is the relaxation rates given by Eq. 76.*

a ring; the exact solutions for N ranging between 3 and 11 were extrapolated to $N \rightarrow \infty$. The temperature dependence of the theoretical dc-susceptibility is shown for several values of the exchange interaction J_{1d} . According to this theory, J_{1d} in Ca_2CuO_3 is of the order 10^3 K.

5.2.3 Magnon Raman Scattering

The μSR determination of T_N is completely unambiguous. On the other hand, there is a certain systematic ambiguity in the estimate of J from uniform susceptibility, due to the subtraction of an impurity Curie and diamagnetic terms. Therefore, it is important to estimate J from more direct measurements. For that purpose, Tajima and collaborators performed a two magnon Raman Scattering experiment at SRL Tokyo.[78] In this experiment a laser light of a given frequency impinges on the sample and the number of photons emitted in nearby (shifted) frequencies is counted. They found a very broad peak in the frequency shift at $T = 7$ K centered at $\Delta E = 2200 \text{ cm}^{-1}$ (see Fig. 52) and spreading over $\sim 2000 \text{ cm}^{-1}$. For comparison a phonon peak would be only 100 cm^{-1} wide.

Since no frequency shift is seen at room temperature, it is attributed to scattering of light from the magnetic system in the ordered state. The interaction of the photon magnetic field with the ionic moment is too weak to produce such scattering and this effect is usually understood within the realm of the two magnon Raman scattering theory. In this theory the light is coupled electrically to the electrons of the oxygen. The scattering process begins with the absorption of an incoming photon by one of the oxygen electrons, exciting it to a higher level. Next, the excited oxygen, which now has a magnetic moment, interacts with the neighboring Cu moments producing two symmetric magnons

traveling left and right. Finally, the electron of the oxygen decays while emitting an outgoing photon of energy lower than that of the incoming photon. Since the magnons are symmetric, their momentum disappears from the kinematic equation and scattering is allowed for a large range of photon frequency shifts, giving rise to the wide peak. This theory predicts that the peak is centered at $E \sim 3J$, indicating an exchange constant J in the order of 10^3 K in Ca_2CuO_3 . [79]

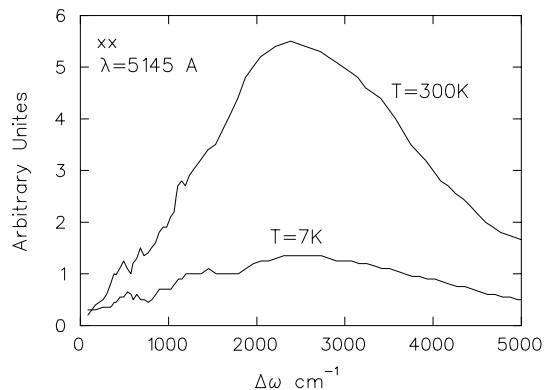


Figure 52: *Frequency shift in Raman scattering on Ca_2CuO_3 .*

The combination of the μSR results with the susceptibility and two magnon Raman scattering measurements demonstrates that Ca_2CuO_3 is a very good quasi one-dimensional compound with a suppression ratio $S = T_N/ZJ_{1d} \leq 0.01$. This ratio indicates that the exchange interaction between the CuO chains is extremely small, though finite. For comparison, in the “Infinite-Layer” system CaCuO_2 , in which oxygen atoms are placed along both the \hat{a} and \hat{b} axis (CuO_2 planes) and the interaction is roughly $3D$ $S \geq 0.1$ (see chapter 4).[7]

5.3 The Sr_2CuO_3 system

The data in Sr_2CuO_3 is very similar to the data in Ca_2CuO_3 and is therefore presented somewhat briefly. The preparation of the sample is done in a way similar to the preparation of Ca_2CuO_3 .

5.3.1 μSR Measurements

Fig. 53 shows μSR time spectra measured in Sr_2CuO_3 . A large increase in the muon spin depolarization occurs between $T = 6.0$ K and 5.5 K, which can be attributed to the slowing down of spin fluctuations, or to the appearance of a random static field. Muon spin oscillations, indicating a static local field, appear only at 4.15 K and therefore the Néel temperature can be determined as $4.15 < T_N < 6$ K. This is consistent

with the absence of magnon Raman scattering peaks in Sr_2CuO_3 at room temperature.[72]

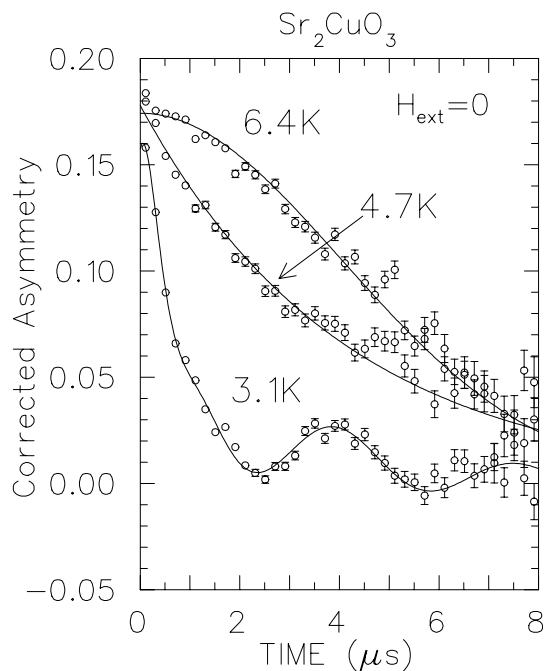


Figure 53: Corrected asymmetry above and below the Néel temperature in Sr_2CuO_3 .

Our measurement at low temperature indicates that the magnetic order in Sr_2CuO_3 involves the majority of the sample volume. The observed oscillation signal is characteristic of uniform magnetic ordering. Therefore, we conclude that the observed transition is due to the onset of magnetic long range order in the CuO chain. The μSR data is analyzed with Eq. 10, using two finite frequencies. The contribution to the relaxation from nuclear moments is deduced from the high temperature data and we assume a single spin-lattice relaxation time. Here again we present only the frequencies, since they are independent of the fitting procedure. The temperature dependence of the two observed frequencies is shown in Fig. 54. We see a fast reduction in the frequencies with increasing temperature, expected for the sub-lattice magnetization of a low dimensional spin system.

5.3.2 Susceptibility Measurements

The susceptibility measurements are made using a Quantum Design SQUID dc-magnetometer with $H = 10$ kOe between 5 K and 400 K. The susceptibility data appearing in Fig. 55 is obtained after subtracting core diamagnetism and magnetic impurity contributions from the measured values; the magnetic impurity susceptibility is assumed to follow a Curie law. The impurity Curie term in Sr_2CuO_3 is sensitive to the annealing condi-

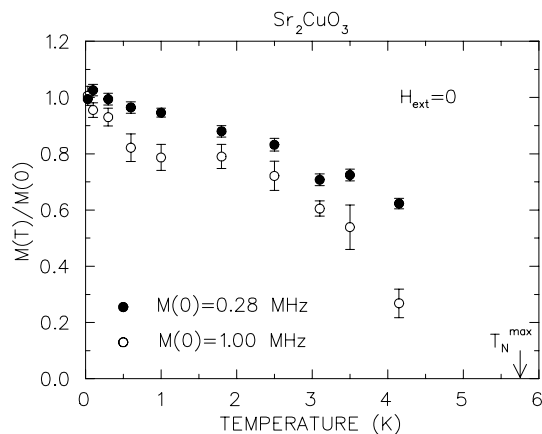


Figure 54: The temperature dependence of the muon-spin precision frequency in zero-field, observed in Sr_2CuO_3 .

tions – time, temperature, and atmosphere – as well as to sample age.[80] Some samples of Sr_2CuO_3 showed a Curie term corresponding to up to a 3% impurity density.

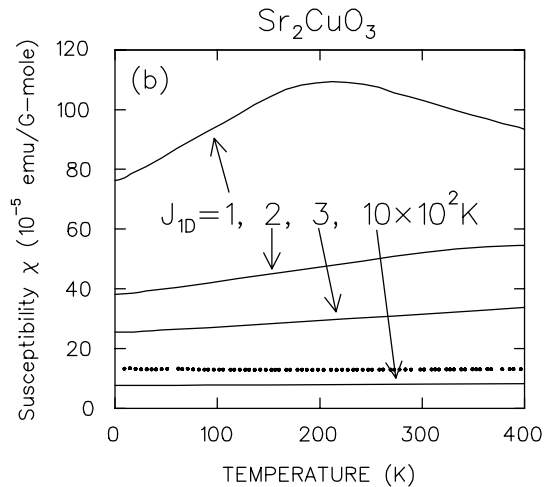


Figure 55: Susceptibility measurements after the Curie and diamagnetic terms have been subtracted compared with 1D model as described in the text.

In Fig. 55 we also compare the susceptibility measurement in Sr_2CuO_3 with the Bonner and Fisher model for 1D antiferromagnetic Heisenberg spin 1/2 chain.[75] The temperature dependence of the dc-susceptibility, for several values of the exchange interaction J_{1d} , is shown in the figure. It is clear that J_{1d} in Sr_2CuO_3 is on the order of 10^3 K, two orders of magnitude higher than the Néel temperature.

5.4 Discussion

In the infinite chain system R_2CuO_3 , the magnetic exchange interaction $J_{1d} \sim 1000$ K, inferred from uniform susceptibility measurements and Raman scattering, is very high, while the present μ SR study revealed that magnetic order occurs only below $T \sim 10$ K. The large ratio of $kT_N/J_{1d} \leq 0.01$ is quite remarkable, it is smaller than those ratios in most of known prototypical 2D [73] and 1D [74] spin systems. This ratio indicates that the exchange interaction between the CuO chains is extremely small but finite. Detailed study of such systems could provide interesting results in testing theories for highly correlated 1D charge/spin chains, such as the 1D Hubbard model. In view of this, there is an ongoing effort to dope charge carriers in R_2CuO_3 . [80]

As for the 123 superconductor, the CuO chains in the 123 system $YBa_2Cu_3O_y$ have oxygen atoms missing for $y < 7.0$; complete chains exist only for $y = 7.0$. Furthermore, the CuO chain in the 123 system serves as a charge reservoir, and the average charge per Cu is often different from that of the Cu^{2+} ions in the insulating chains in R_2CuO_3 . In $PrBa_2Cu_3O_7$, for example, Takenaka *et al.* [81] performed an optical study and found that there are 0.5 holes per Cu in the CuO chain. The same number is expected in the CuO chain of $YBa_2Cu_3O_7$. Therefore, it is not appropriate to make a direct comparison between R_2CuO_3 and the CuO chains in the superconducting 123 systems.

On the other hand, there exist experimental results indicating that the chains in the 123 systems exhibit a quasi one-dimensional nature. Two examples are: a) the low ordering temperature of the chain Cu moments; Li *et al.* [82] performed neutron scattering measurements in $NdBa_2Cu_3O_{6.35}$ and showed that the Cu moments in the CuO_2 planes order at $T_{N1} = 230$ K, while those in the CuO chain order at the lower temperature $T_{N2} = 10$ K. b) the tendency of holes, doped into the 123 chains, to be localized at low energy and low temperatures, as demonstrated [81] in $PrBa_2Cu_3O_7$. These features are most likely due to the geometrical structure of the CuO chains in these 123 compounds, characterized by the absence of an oxygen atom between adjacent Cu atoms in the \hat{a} -direction. In this sense these 123 systems and Sr_2CuO_3 share a common origin for their quasi 1D behavior.

Acknowledgments

When I applied to graduate schools in the U. S. A. I was looking for scientific excitement and personal adventure. What I have found at Columbia University was far beyond my wildest dreams and exceeded all my expectations. For these wonderful years I want to thank the American people for their hospitality and all the teachers and staff members of Columbia, especially my two advisers Tomo Uemura and Graeme Luke. Their

love of physics and drive for indisputable data is contagious, and their scientific integrity is admirable. I could not imagine a more pleasant and creative working atmosphere than that which exists in our group, side by side with a sense of urgency and exciting scientific discoveries. I would also like to thank the older students in the group: Ben Sternlieb, Lian Ping Le, and Weidong Wu, for their patience and their willingness to teach me the details of our trade, and to the younger students, Kenji Kojima, Oleg Tchernyshyov, and Ben Nachumi, for their scientific curiosity and constant debate on physics problems.

I owe a very special thanks to my wife, Michal Cooper-Keren, for her love, support, and encouragement, and for more practical reasons as well. Michal, as a writer, is able to structure any sentence, paragraph, or full paper in a way that makes it crystal clear even when she is unfamiliar with the material. The work I published during my Ph.D. as a single author could not have been possible without her help.

For some of the work presented in this thesis, I sought advice from scientists who are not part of our group. I would like to acknowledge the help of Prof. Jess Brewer (section 2.1), Syd Kritzman (sections 2.3 and 2.4), Prof. Jacob Shaham (section 2.3), Prof. Allan Blaer (section 3.4), and Prof. Viet Elser (section 3.4).

Experiments at an accelerator (μ SR) necessarily involve the efforts of a relatively large group of people. It has been my great good fortune to experience working with the μ SR group at TRIUMF including Rob Kiefl, Keith Hoyle, and Curtis Ballard. I would also like to take this opportunity to thank Prof. Setsuko Tajima for allowing me to participate in the magnon Raman scattering experiment (52) and Prof. Masashi Takigawa for the NMR experiment in the chain systems (in progress).

Finally, none of this work would have been possible without the help of our collaborators Prof. Shinichi Uchida, Prof. Mamoru Mekata and Prof. Mikio Takano, who contributed the samples and many of the insights that lead to our conclusions.

A The McMullen and Zaremba Formula

Our aim in this appendix is to derive Eq. 21 using perturbation theory. In order to do so we break the Hamiltonian

$$\mathcal{H} = \mathcal{H}_c - \boldsymbol{\mu} \cdot \mathbf{B}. \quad (77)$$

into two terms

$$\mathcal{H} = \mathcal{H}_0 + \mathcal{H}' \quad (78)$$

where

$$\mathcal{H}_0 = \mathcal{H}_c - \boldsymbol{\mu} \cdot \mathbf{B}^s \quad (79)$$

and

$$\mathcal{H}' = -\boldsymbol{\mu} \cdot \mathbf{B}^d \quad (80)$$

as in chapter 2. The fields \mathbf{B}^s and \mathbf{B}^d represent the static and dynamic components of the field at the muon site respectively. The $\hat{\mathbf{z}}$ direction is chosen as the direction of \mathbf{B}^s . We further define any operator (O) with explicit time dependence as

$$O(t) = \exp(i\mathcal{H}_0 t/\hbar) O \exp(-i\mathcal{H}_0 t/\hbar) \quad (81)$$

and thus

$$\sigma_{\pm}(t) = \sigma_{\pm} e^{\mp i\omega_s t}, \quad (82)$$

$$\sigma_z(t) = \sigma_z. \quad (83)$$

The time propagation operator for the states of the combined system (muon and crystal) is given by

$$U(t) = \exp\left(-\frac{i}{\hbar}\mathcal{H}_0 t\right) \left[1 - \frac{i}{\hbar} \int_0^t dt' \mathcal{H}'(t') \right. \\ \left. - \frac{1}{\hbar^2} \int_0^t dt' \int_0^{t'} dt'' \mathcal{H}'(t') \mathcal{H}(t'') + \dots \right] \quad (84)$$

We also define the density matrix for the combined system as

$$\rho = \rho_0 \rho_{\mu} \quad (85)$$

where

$$\rho_0 = \frac{e^{-\beta\mathcal{H}_c}}{\text{Tr} e^{-\beta\mathcal{H}_c}}, \quad (86)$$

$$\rho_{\mu} = \frac{1 + \mathbf{P} \cdot \boldsymbol{\sigma}}{2}, \quad (87)$$

$$(88)$$

and \mathbf{P} is the initial muon polarization. The temperature-averaged polarization as a function of time is given by

$$\mathbf{P}(t) = \langle \boldsymbol{\sigma} \rangle = \text{Tr} \rho U^{\dagger}(t) \boldsymbol{\sigma} U(t). \quad (89)$$

This leads to the perturbation series

$$\mathbf{P}(t) = \langle \boldsymbol{\sigma}(t) \rangle_{(0)} + \langle \boldsymbol{\sigma}(t) \rangle_{(1)} + \langle \boldsymbol{\sigma}(t) \rangle_{(2)} + \dots \quad (90)$$

where

$$\langle \sigma_+(t) \rangle_{(0)} = P_+ e^{-i\omega_s t} \quad (91)$$

$$\langle \sigma_z(t) \rangle_{(0)} = P_z. \quad (92)$$

and

$$\langle \boldsymbol{\sigma}(t) \rangle_{(1)} = \frac{i}{\hbar} \int_0^t dt' \langle [\mathcal{H}'(t'), \boldsymbol{\sigma}(t)] \rangle \quad (93)$$

$$\langle \boldsymbol{\sigma}(t) \rangle_{(2)} = -\frac{1}{\hbar^2} \int_0^t dt' \int_0^{t'} dt'' \\ \times \langle [[\mathcal{H}'(t''), [\mathcal{H}'(t'), \boldsymbol{\sigma}(t)]]] \rangle. \quad (94)$$

In these equations $\omega_s = \gamma_m |\mathbf{B}^s|$, $\langle \rangle$ indicates a trace with respect to the initial density matrix ρ , and $[,]$ is the commutator.

The lowest order terms represent the μ^+ spin precession in the static field \mathbf{B}^s ; the linear term in H' contains the expectation value $\langle \mathbf{B}^d \rangle$ which by definition is zero at all times; the third term $\langle \sigma_+(t) \rangle_{(2)}$ is given by

$$\langle \sigma_+(t) \rangle_{(2)} = -\frac{\gamma_m^2}{2} e^{-i\omega t} \int_0^t dt' \int_0^{t'} dt'' \quad (95)$$

$$\left(P_+ \langle \{ B_z^d(t'), B_z^d(t'') \} \rangle_0 + \frac{1}{2} P_+ \langle \{ \tilde{B}_+^d(t'), \tilde{B}_-^d(t'') \} \rangle_0 \right. \\ \left. - \frac{1}{2} P_- \langle \{ \tilde{B}_+^d(t'), \tilde{B}_+^d(t'') \} \rangle_0 - P_z \langle \{ B_z^d(t'), \tilde{B}_+^d(t'') \} \rangle_0 \right. \\ \left. + \langle [\tilde{B}_+^d(t'), B_z^d(t'')] \rangle_0 - \langle [\tilde{B}_z^d(t'), B_+^d(t'')] \rangle_0 \right)$$

and

$$\langle \sigma_z(t) \rangle_{(2)} = -\frac{\gamma_m^2}{4} \int_0^t dt' \int_0^{t'} dt'' \quad (96)$$

$$\left(P_z \langle \{ \tilde{B}_+^d(t'), \tilde{B}_-^d(t'') \} \rangle_0 + P_z \langle \{ \tilde{B}_-^d(t'), \tilde{B}_+^d(t'') \} \rangle_0 \right. \\ \left. - P_- \langle \{ \tilde{B}_+^d(t'), B_z^d(t'') \} \rangle_0 - P_+ \langle \{ \tilde{B}_-^d(t'), B_z^d(t'') \} \rangle_0 \right. \\ \left. + \langle [\tilde{B}_-^d(t'), \tilde{B}_+^d(t'')] \rangle_0 - \langle [\tilde{B}_+^d(t'), \tilde{B}_-^d(t'')] \rangle_0 \right)$$

where

$$\tilde{B}_{\pm}^d(t) = e^{\pm i\omega t} B_{\pm}^d(t) \\ B_{\pm}^d(t) = B_x^d(t) \pm iB_y^d(t) \quad (97) \\ \mathbf{B}^d(t) = e^{i\mathcal{H}_0 t/\hbar} \mathbf{B}^d e^{-i\mathcal{H}_0 t/\hbar}$$

and where \langle , \rangle_0 indicates a trace with respect to ρ_0 .

Here we are only interested in the longitudinal configuration; therefore, we take $P_+ = P_- = 0$ and evaluate $\langle \sigma_z(t) \rangle_{(2)}$. We can see from Eq. 96 that the last two terms will contribute to $\langle \sigma_z(t) \rangle_{(2)}$ even if $\mathbf{P} = 0$ and these terms can generate polarization out of a non-polarized ensemble. Since the equilibrium polarization at 10 mK and a typical internal field of 1 kG is only 0.03 these terms must cancel or be very small; therefore, we ignore them. Now, with the help of Eq. 97 we obtain Eq. 21

$$\langle \sigma_z(t) \rangle_{(2)} = -\frac{\gamma_m^2}{4} P_z \int_0^t dt' \int_0^{t'} dt'' \times \quad (98) \\ e^{i\omega_s(\tau)} \Phi_{+-}(\tau) + e^{-i\omega_s(\tau)} \Phi_{-+}(\tau)$$

where $\tau = t' - t''$ and

$$\Phi_{\nu\nu'}(t' - t'') = \langle B_{\nu}^d(t') B_{\nu'}^d(t'') + B_{\nu'}^d(t'') B_{\nu}^d(t') \rangle_0. \quad (99)$$

In the last equation we made the assumption that the correlation function depends only on the time difference. This assumption stems from time translation symmetry. We can now eliminate one of the integrals and arrive at Eq. 24

Next we wish to demonstrate that the relaxation rate in the fast limit is given by the spectral density at

the Larmor frequency ($\tilde{\Phi}_{\nu\nu'}(\omega_s)$) as in Eq. 31. To do so we first define the spectral density using the Fourier transform

$$\tilde{\Phi}_{\nu\nu'}(\omega) = \int_{-\infty}^{\infty} \Phi_{\nu\nu'}(\tau) e^{i\omega\tau} d\tau \quad (100)$$

which leads to

$$\langle \sigma_z(t) \rangle_{(2)} = t \int \frac{d\omega}{2\pi} f_t(\omega - \omega_s) \Phi_{+-}(\omega) \quad (101)$$

where

$$f_t(\omega) = \frac{\sin^2(\omega t)}{\omega^2 t} \quad (102)$$

and

$$\lim_{t \rightarrow \infty} f_t(\omega) = \pi \delta(\omega). \quad (103)$$

If we now write $P(t) = P(0) \exp(-t/T_1)$, expand in powers of t/T_1 , and compare with Eqs. 21 and 101, after the integration with the delta function we arrive at Eq. 31.

B The Fermi Golden Rule

The method developed in appendix A is very general and applicable in a variety of limits. In the fast limit ($t \rightarrow \infty$) it can be directly connected to the well-known Fermi Golden Rule. In order to understand this connection, we denote: the eigenstates of the system by $|i\rangle$, the eigenvalues by E_i , and the matrix element $\mathbf{B}_{fi}^d = \langle f | \mathbf{B}^d | i \rangle$. Inserting the closure relation

$$1 = \sum |i\rangle \langle i|$$

between any two operators in Eq. 98, keeping in mind that

$$\exp^{i\mathcal{H}_0 t/\hbar} |i\rangle = e^{iE_i t/\hbar} |i\rangle,$$

and performing the time integrals we obtain:

$$\begin{aligned} \langle \sigma_z(t) \rangle_{(2)} &= -(\hbar\gamma_m)^2 P_z \sum_{if} \frac{e^{-\beta E_i}}{z} \\ &\times \left(B_{+if}^d B_{-fi}^d \frac{\sin^2[(E_i - E_f + \hbar\omega_s)t/2\hbar]}{(E_i - E_f + \hbar\omega_s)^2} \right. \\ &+ \left. B_{-if}^d B_{+fi}^d \frac{\sin^2[(E_i - E_f - \hbar\omega_s)t/2\hbar]}{(E_i - E_f - \hbar\omega_s)^2} \right). \end{aligned} \quad (104)$$

At times longer than the Larmor period $2\pi/\omega_s$ we can make the replacement

$$\frac{\sin^2[(E_i - E_f + \hbar\omega)t/2\hbar]}{(E_i - E_f + \hbar\omega)^2} = \frac{\pi t}{2\hbar} \delta(E_i - E_f + \hbar\omega) \quad (105)$$

arriving ultimately at the temperature-averaged Fermi golden rule

$$\frac{1}{T_1} = \frac{\pi\hbar}{2} \gamma_m^2 \sum_{if\pm} \frac{e^{-\beta E_i}}{z} \times |B_{-if}^d|^2 \delta(E_i - E_f \pm \hbar\omega). \quad (106)$$

C Spin-Wave Theory

The starting point is the Hamiltonian

$$\mathcal{H} = -J \sum_{i>j} \mathbf{s}^i \cdot \mathbf{s}^j$$

and the spin commutation relation

$$[S_\alpha^j, S_\beta^j] = i\epsilon_{\alpha\beta\gamma} S_\gamma^j.$$

For the antiferromagnetic case where two sublattices exist, an exact representation of the spin operators in terms of Bose creation and destruction operators may be given by:

$$\begin{aligned} S_+^i &= (2S - a_i^\dagger a_i)^{1/2} a_i & S_+^j &= b_j^\dagger (2S - b_j^\dagger b_j)^{1/2} \\ S_-^i &= a_i^\dagger (2S - a_i^\dagger a_i)^{1/2} & S_-^j &= (2S - b_j^\dagger b_j)^{1/2} b_j \\ S_z^i &= S - a_i^\dagger a_i & S_z^j &= S - b_j^\dagger b_j \end{aligned}$$

where the operator a creates spin deviation on the first sublattice, namely, $a_i |n\rangle = \sqrt{n} |n-1\rangle$, n runs from S to $-S$ and $n = S$ means spin fully up. The operator b creates spin deviation on the other sublattice but this time $n = S$ means spin fully down. The operators also obey:

$$\begin{aligned} a_i a_{i'}^\dagger - a_{i'}^\dagger a_i &= \delta_{ii'} \\ a_i^\dagger a_{i'}^\dagger - a_{i'}^\dagger a_i^\dagger &= 0 \\ a_i a_{i'} - a_{i'} a_i &= 0 \end{aligned}$$

and the same for the b operators. The a and b operators commute. In the harmonic oscillator approximation we keep only first terms in $1/S$ expansion. We therefore have

$$\begin{aligned} S_+^i &= (2S)^{1/2} a_i & S_+^j &= (2S)^{1/2} b_j^\dagger \\ S_-^i &= (2S)^{1/2} a_i^\dagger & S_-^j &= (2S)^{1/2} b_j \\ S_z^i &= S - a_i^\dagger a_i & S_z^j &= S - b_j^\dagger b_j. \end{aligned} \quad (107)$$

Next, we introduce the Fourier transforms of the creation and destruction operators of spin deviations

$$\begin{aligned} a_{\mathbf{k}} &= (2/N)^{1/2} \sum_i a_i \exp(-i\mathbf{k} \cdot \mathbf{r}_i) \\ b_{\mathbf{k}} &= (2/N)^{1/2} \sum_j b_j \exp(-i\mathbf{k} \cdot \mathbf{r}_j) \end{aligned}$$

where \mathbf{r}_i and \mathbf{r}_j are lattice vectors of the i th and j th site on the appropriate sublattices and \mathbf{k} belongs to the first Brillouin zone (with two magnetic ions in the primitive cell). Now we can write the Hamiltonian in terms of spin waves

$$\mathcal{H}_0 = E_0 - 2JZS \sum_{\mathbf{k}} (a_{\mathbf{k}}^\dagger a_{\mathbf{k}} + b_{\mathbf{k}}^\dagger b_{\mathbf{k}}) + \gamma_{\mathbf{k}} (a_{\mathbf{k}}^\dagger b_{\mathbf{k}}^\dagger + b_{\mathbf{k}} a_{\mathbf{k}}) \quad (108)$$

where E_0 is a constant, Z is the number of near neighbors, and

$$\gamma_{\mathbf{k}} = \frac{1}{Z} \sum_{nn} \exp(i\mathbf{k} \cdot \mathbf{r}_{nn})$$

where \mathbf{r}_{nn} is the vector connecting a given spin with its nearest neighbor. The harmonic Hamiltonian is not

yet diagonal. It can be diagonalized, however, by the canonical transformation

$$\begin{aligned} a_k &= u_k M_{1k} + v_k M_{2k}^\dagger & b_k &= v_k M_{1k}^\dagger + u_k M_{2k} \\ a_k^\dagger &= u_k M_{1k}^\dagger + v_k M_{2k} & b_k &= v_k M_{1k} + u_k M_{2k}^\dagger, \end{aligned} \quad (109)$$

where M_{pk} and M_{pk}^\dagger are Bose creation and destruction operators of a magnon with polarization p and wavevector \mathbf{k} , and u_k and v_k are functions of \mathbf{k} . In order to maintain the commutation relation

$$M_{ik} M_{ik}^\dagger - M_{ik}^\dagger M_{ik} = 1,$$

we must have

$$u_k^2 - v_k^2 = 1. \quad (110)$$

By substituting 109 in 108 we get

$$\begin{aligned} \mathcal{H}_0 &= E'_0 + \sum_k \{ [M_{1k}^\dagger M_{1k} + M_{2k}^\dagger M_{2k}] \\ &\times [(u_k^2 + v_k^2)(-2JSZ - 4u_k v_k JSZ \gamma_k)] \\ &+ [M_{1k}^\dagger M_{2k}^\dagger + M_{1k} M_{2k}] [-4u_k v_k JSZ \\ &- 2(u_k^2 + v_k^2) JSZ \gamma_k] \} \end{aligned} \quad (111)$$

which can now be simplified by taking

$$-4u_k v_k JSZ - 2(u_k^2 + v_k^2) JSZ \gamma_k = 0. \quad (112)$$

We thus arrive at two equations for u_k and v_k which give

$$\begin{aligned} u_k &= \rho_k [\rho_k^2 - 4(JSZ \gamma_k)^2]^{-1/2} \\ v_k &= 2JSZ \gamma_k [\rho_k^2 - 4(JSZ \gamma_k)^2]^{-1/2} \\ \rho_k &= 2JSZ \{ [1 - \gamma_k^2]^{1/2} - 1 \}. \end{aligned} \quad (113)$$

The diagonalized Hamiltonian is given by

$$\mathcal{H}_0 = \sum_{p,k} \hbar \omega_k (n_{pk} + 1/2)$$

where $n_{pk} = M_{pk}^\dagger M_{pk}$ and

$$E(\mathbf{k}) = \hbar \omega_k = 2JZS(1 - \gamma_k^2)^{1/2}.$$

In the long wavelength limit we have

$$E(\mathbf{k}) = \theta_N b k \quad (114)$$

where θ_N is of the order of $k_B T_N$, b depends only on the geometry of the lattice and is equal to $\sqrt{1/3}c$ for the three cubic structures, and c is the nearest neighbor separation. The eigenstates of H_0 are denoted by $|\{n_{kp}\}\rangle$ where n_{kp} is the number of excitation or spin waves in the mode $p\mathbf{k}$.

For practical purposes it is convenient to express the spin operators \mathbf{S} in terms of the creation and annihilation operators M_{pk}^\dagger and M_{pk} of spin waves

$$\begin{aligned} S_+^i &= 2(S/N)^{1/2} \sum_k \exp(-\mathbf{k} \cdot \mathbf{r}_i) (u_k M_{1k} + v_k M_{2k}^\dagger) \\ S_+^j &= 2(S/N)^{1/2} \sum_k \exp(-\mathbf{k} \cdot \mathbf{r}_j) (v_k M_{1k} + u_k M_{2k}^\dagger) \end{aligned}$$

and to note that in the long wavelength limit we have

$$\begin{aligned} \lim_{k \rightarrow 0} u_k &\sim \frac{1}{k^{1/2}} \\ \lim_{k \rightarrow 0} v_k &\sim \frac{1}{k^{1/2}}. \end{aligned}$$

these equations are used in sections 2.3. For a more detailed review see Ref. [83]

D Spin Glass

In a spin-glass such as CuMn or AuFe, the magnetic impurities are located randomly in the sample.[36] The random distance between the muon and the impurities result in a distribution of second moments. Therefore, we treat the parameter Δ as a statistical variable. As an example, let us consider the case of a dilute spin-glass at temperatures above the freezing temperature T_g . In this case, Uemura *et al.*[36] demonstrated that the distribution of Δ can be approximated by

$$\rho(\Delta) = \sqrt{2/\pi} \frac{a}{\Delta^2} \exp\left(-\frac{a^2}{2\Delta^2}\right). \quad (116)$$

The spin-glass relaxation function is obtained by averaging Eq. 27 with respect to Δ . In order to maintain the condition $\Delta < \nu$, the parameter a must satisfy $a < \nu$. The resulting Uemura function is

$$\begin{aligned} P_z^{SG}(t) &= \int_0^\infty \exp(-\Gamma(t)t) \rho(\Delta) d\Delta \\ &= \exp\left(-\sqrt{2a^2 \gamma(t)t}\right) \end{aligned} \quad (117)$$

where

$$\gamma(t) \equiv \Gamma(t)/\Delta^2.$$

Using $\Gamma(t)$ from Eq. 30 we see that in the fast limit the relaxation has a root-exponential shape. $\Gamma(t)$ given by Eq. 32 leads to an exponential relaxation in the early time limit. In Fig. 56 we show the polarization function obtained with Eq. 117 for $\nu = a$. From the figure we observe that, in the spin glass case, the LF is less effective in recovering the polarization than in the case of a field distribution with a unique width. This slow recovery is a consequence of the high field tail resulting from the convolution of the field distribution and Eq. 116. We also note, in Fig. 56, the exponential relaxation at the early times and the presence of oscillations with frequency ω_L near $\nu t \rightarrow 0$.

References

- [1] A. Keren. *Hyp. Int.*, **85**, 281, 1994.
- [2] A. Keren, L. P. Le, G. M. Luke, W. D. Wu, and Y. J. Uemura. *Hyp. Int.*, **85**, 363, 1994.
- [3] A. Keren. *Phys. Rev. B*, **50**, 10039, 1994.

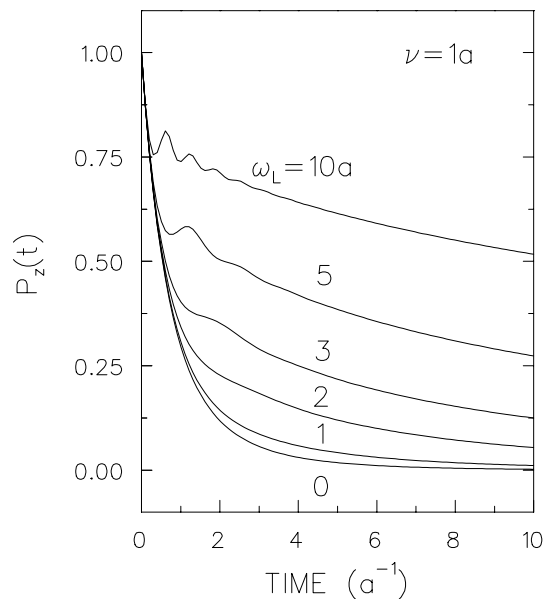


Figure 56: Muon relaxation function in a spin glass in the longitudinal field configuration. The longitudinal field is given by $H_L = \omega_L / \gamma_m$.

- [4] A. Keren. preprint, 1994. To be published in J. M. M. M.
- [5] A. Keren, L. P. Le, G. M. Luke, W. D. Wu, Y. J. Uemura, A. Ajiro, T. Asano, H. Kuriyama, M. Mekata, and H. Kikuchi. *Hyp. Int.*, **85**, 181, 1994.
- [6] A. Keren. *Phys. Rev. Lett.*, **72**, 3254, 1994.
- [7] A. Keren, L. P. Le, G. M. Luke, B. J. Sternlieb, W. D. Wu, Y. J. Uemura, S. Tajima, and S. Uchida. *Phys. Rev. B*, **48**, 12926, 1993.
- [8] A. Keren, K. Kojima, L. P. Le, G. M. Luke, W. D. Wu, Y. J. Uemura, S. Tajima, and S. Uchida. preprint, 1994. To be published in J. M. M. M.
- [9] A. Schenck. *Muon Spin Rotation Spectroscopy: Principles and Application in Solid State Physics*. Hilger, Bristol, 1986.
- [10] R. S. Hayano, Y. J. Uemura, J. Imazato, N. Nishida, T. Yamazaki, and R. Kubo. *Phys. Rev. B*, **20**, 850, 1979.
- [11] T. McMullen and E. Zaremba. *Phys. Rev. B*, **18**, 3026, 1978.
- [12] T. Moriya. *Progr. Theoret. Phys.*, **28**, 371, 1962.
- [13] Y. J. Uemura *et al.* *Hyp. Int.*, **31**, 313, 1986.
- [14] R. De. Renzi, G. Guidi, P. Podini, R. Tedeschi, C. Bucci, and S. F. J. Cox. *Phys. Rev. B*, **30**, 197, 1984.
- [15] M. P. Schulhof, R. Nathans, P. Heller, and A. Linz. *Phys. Rev. B*, **4**, 2254, 1971.
- [16] J. Van Kranendonk and M. Bloom. *Physica*, **XXII**, 545, 1956.
- [17] T. Moriya. *Progr. Theoret. Phys. (Kyoto)*, **16**, 23, 1956.
- [18] N. Kaplan, R. Loudon, V. Jaccarino, and H. J. Guggenheim. *Phys. Rev. Lett.*, **17**, 357, 1966.
- [19] E. F. Shender and P. C. W. Holdsworth. In *Fluctuations and Order: The new Synthesis*. Springer-Verlag, 1994.
- [20] A. B. Harris, C. Kallin, and A. J. Berlinsky. *Phys. Rev. B*, **45**, 2899, 1992.
- [21] C. Zeng and V. Elser. *Phys. Rev. B*, **42**, 8436, 1990.
- [22] J. T. Chalker, P. C. W. Holdsworth, and E. F. Shender. *Phys. Rev. Lett.*, **68**, 855, 1992.
- [23] Jan N. Reimers and A. J. Berlinsky. *Phys. Rev. B*, **48**, 9539, 1993.
- [24] C. L. Henley. preprint, 1994. presented at the ICM'94 meeting.
- [25] A. Chubukov. *Phys. Rev. Lett.*, **69**, 832, 1992.
- [26] S. Sachdev. *Phys. Rev. B*, **45**, 12377, 1992.
- [27] J. von Delft and C. L. Henley. *Phys. Rev. B*, **48**, 965, 1993.
- [28] A. P. Ramirez, G. P. Espinosa, and A. S. Cooper. *Phys. Rev. Lett.*, **64**, 2070, 1990.
- [29] B. Martínez, F. Sandiumenge, A. Rouco, A. Labarta, J. Rodríguez Carvajal, M. Tovar, M. T. Causa, S. Galí, and X. Obradors. *Phys. Rev. B*, **46**, 10786, 1992.
- [30] R. G. Palmer. *Adv. Mod. Phys.*, **31**, 669-735, 1982.
- [31] X. Obradors, A. Labarta, A. Isalgué, J. Tejada, and J. Rodríguez M. Pernet. *Solid State Commun.*, **5**, 189, 1988.
- [32] B. Martínez, A. Labarta, J. Rodríguez Solá, and X. Obradors. *Phys. Rev. B*, 1992. in press.
- [33] A. P. Ramirez, G. P. Espinosa, and A. S. Cooper. *Phys. Rev. B*, **45**, 2505, 1992.

- [34] A. P. Ramirez. *Annu. Rev. Mater. Sci.*, **23**, 453, 1994.
- [35] C. Broholm, G. Aeppli, G. P. Espinosa, and A. S. Cooper. *Phys. Rev. Lett.*, **65**, 3173, 1990.
- [36] Y. J. Uemura *et. al.* *Phys. Rev. B*, **31**, 546, 1985.
- [37] Y. J. Uemura, A. Keren, L. P. Le, G. M. Luke, B. J. Sternlieb, and W. D. Wu. *Hyp. Int.*, **85**, 133, 1994.
- [38] Y. J. Uemura, A. Keren, K. J. Kojima, L. P. Le, G. M. Luke, W. D. Wu, Y. Ajiro, T. Asano, Y. Kuriyama, M. Mekata, H. Kikuchi, and K. Kakurai. preprint, 1994. Submitted to J. M. M. M.
- [39] R. Wang, W. F. Bradley, and H. Steinfink. *Acta Cryst.*, **18**, 249, 65.
- [40] M. Takano, T. Shinjo, and T. Takada. *J. Phys. Soc. Japan*, **30**, 1049, 1971.
- [41] M. G. Townsend, G. Longworth, and E. Roudaut. *Phys. Rev. B*, **33**, 4919, 1986.
- [42] A. P. Ramirez, C. Broholm, S. H. Lee, M. F. Collins, L. Heller, C. Kloc, and E. Bucher. *J. Appl. Phys.*, **73**, 5658, 1993.
- [43] C. Broholm, S. H. Lee, M. F. Collings, L. Heller, A. P. Ramirez, C. Kloc, and E. Bucher. preprint, 1993.
- [44] W. H. Press, B. P. Flannery, A. A. Teukolsky, and W. T. Vetterling. *Numerical Recipes*. Cambridge University Press, Cambridge, 1989.
- [45] G. M. Wysin and A. R. Bishop. *Phys. Rev. B*, **42**, 810, 1990.
- [46] E. B. Brown. *Phys. Rev. B*, **45**, 10809, 1992.
- [47] H. Shenker and J. Tobochnik. *Phys. Rev. B*, **22**, 4462, 1980.
- [48] S. Ma. *Modern Theory of Critical Phenomena*. Addison-Wesley Publishing Company, 1976.
- [49] Y. J. Uemura, A. Keren, K. J. Kojima, L. P. Le, G. M. Luke, W. D. Wu, Y. Ajiro, T. Asano, Y. Kuriyama, M. Mekata, H. Kikuchi, and K. Kakurai. *Phys. Rev. Lett.*, 1994. To be published in *Phys. Rec. Lett.*
- [50] See, for example, papers published in Proceedings of the International Conference on Materials and Mechanisms of Superconductivity High Temperature Superconductors II, Stanford University, California, USA, 1989; *Physica C* 162-164; Proceedings of the International Conference on Materials and Mechanisms of Superconductivity High Temperature Superconductors III, Kanazawa, Japan, 1991; *Physica C* 185-189.
- [51] L. P. Le., G. M. Luke, B. J. Sternlieb, J. H. Brewer Y. J. Uemura, T. M. Riseman, D. C. Johnston, and L. L. Miller. *Phys. Rev. B*, **42**, 2182, 1990.
- [52] T. Siegrist, S. M. Zahurak, D. W. Murphy, and R. S. Roth. *Nature*, **334**, 231-232, 1988.
- [53] R. S. Roth. In *Am. Phys. Soc. Meeting*, New Orleans, 1988.
- [54] M. Takano, Y. Takeda, H. Okada, M. Miyamoto, and T. Kusaka. *Physica C*, **159**, 375-378, 1989.
- [55] M. Azuma, Z. Hiroi, M. Takano, Y. Bando, and Y. Takeda. *Nature*, **356**, 775-775, 1992.
- [56] M. G. Smith, A. Manthiram, J. Shou, J. B. Goodenough, and J. T. Markert. *Nature*, **351**, 549-551, 1991.
- [57] D. Vaknin E. Caignol P. K. Davies J. E. Fischer D. C. Johnston and D. P. Goshorn. *Phys. Rev. B*, **39**, 9122, 1989.
- [58] Y. J. Uemura., W. J. Kossler, J. R. Kempton, X. H. Yu, H. E. Schone, D. Opie, C. E. Stronach, J. H. Brewer, R. F. Kiefl, S. R. Kreitsman, G. M. Luke, T. Riseman, K. Ll. Williams, E. J. Ansaldo, Y. Endoh, K. Kudo, K. Yamada, D. C. Johnston, M. Alvarez, D. P. Goshorn, Y. Hidaka and M. Oda, Y. Enomoto, M. Suzuki, and T. Murakame. *Physica C*, **153-155**, 769-770, 1988.
- [59] Y. Tokura, S. Koshihara, T. Arima, H. Takagi, S. Ishibashi, T. Ido, and S. Uchida. *Phys. Rev. B*, **41**, 11657, 1990.
- [60] A. Abragam. *Principles of Nuclear Magnetism*. Oxford University Press, 1961.
- [61] C. P. Slichter. *Principles of Magnetic Resonance*. Springer-Verlag, Berlin Heidelberg, 1978.
- [62] D. Vaknin, S. K. Sinha, C. Stassis, L. L. Miller, and D. C. Johnston. *Phys. Rev. B*, **41**, 1926, 1990.
- [63] R. F. Kiefl, J. H. Brewer, I. Affleck, J. F. Carolan, P. Dosanjh, W. N. Hardy, T. Hsu, P. Kadone, J. R. Kempton, S. R. Kreitzman, Q. Li, A. H. O'Reilly, T. M. Riseman, P. Schleger, P. C. E. Stamp, L. P. Le, G. M. Luke, B. Sternlieb, Y. J. Uemura, H. R. Hart, and K. W. Lay. *Phys. Rev. Lett.*, **64**, 2082, 1990.
- [64] Q. Li and J. H. Brewer. *Hyp. Int.*, **63**, 169-176, 1991.

- [65] W. K. Dawson, K. Tibbs, S. P. Weathersby, C. Boekema, and K. C. B. Chan. *J. Appl. Phys.*, **64**, 5890, 1988.
- [66] B. Y. Yand, S. Mitsuda, G. Shirane, Y. Yamaguchi, H. Yamauchi, and Y. Syono. *J. Phys. Soc. Jpn.*, **56**, 2283, 1987.
- [67] L. L. Miller, X. L. Wand, S. X. wand, C. Stassis, D. C. Johnston, J. Faber, and Jr. and C.-K. Loong. *Phys. Rev. B*, **41**, 1921, 1990.
- [68] M. E. Lines. *J. Phys. Chem. Solid*, **31**, 101, 1970.
- [69] G. Shirane, Y. Endoh, R. J. Birgeneau, M. A. Kastner, Y. Hidaka, M. Oda, M. Suzuki, and T. Murakami. *Phys. Rev. Lett.*, **59**, 1613, 1987.
- [70] D. A. Tennant, T. G. Perring, and R. A. Cowley. *Phys. Rev. Lett.*, **70**, 4003, 1993.
- [71] G. Müller, H. Thomas, H. Beck, and J. Bonner. *Phys. Rev. B*, **24**, 1429, 1981.
- [72] M. Yoshida, S. Tajima, N. Koshizuka, and S. Tanaka. *Phys. Rev. B*, **44**, 11997, 1991.
- [73] L. J. de Jonge and A. R. Miedama. *Adv. Mod. Phys.*, **23**, 1, 1974.
- [74] M. Steiner, J. Villain, and C. G. Windsor. *Adv. Phys.*, **25**, 87, 1976.
- [75] J. C. Bonner and M. E. Fisher. *Phys. Rev.*, **135**, A640, 1964.
- [76] L. P. Le, A. Keren, G. M. Luke, B. J. Sternlieb, W. D. Wu, Y. J. Uemura, J. H. Brewer, T. M. Riseman, R. V. Upasani, L. Y. Chiang, W. Kang, and P. M. Chaikin. *Phys. Rev. B*, **48**, 1993, 7284.
- [77] S. Fraga, K. M. S. Saxena, and J. Karwowski. *Handbook of Atomic Data*. Elsevier, Amsterdam, 1976.
- [78] S. Tajima. preprint, 1994. in preparation.
- [79] P. A. Fleury and R. Loudon. *Phys. Rev.*, **166**, 514, 1967.
- [80] T. Ami, M. K. Crawford, R. L. Harlow, Z. R. Wand, D. C. Johnston, Q. Huang, and R. W. Erwin. preprint, 1994.
- [81] K. Takenaka, Y. Imanaka, K. Tamasaku, T. Ito, and S. Uchida. *Phys. Rev. B*, **46**, 5833, 1992.
- [82] W-H. Li, J. W. Lynn, and Z. Fisk. *Phys. Rev. B*, **41**, 4098, 1990.
- [83] V. Jaccarino. In *Magnetism*, page 307. Academic Press Inc., New York, 1963.